TECHNISCHE UNIVERSITÄT MÜNCHEN

Lehrstuhl für Aerodynamik und Strömungsmechanik

Numerical Simulation of Cavitating Flows in Diesel Injection Systems

Felix Martin Örley

Vollständiger Abdruck der von der Fakultät für Maschinenwesen der Technischen Universität München zur Erlangung des akademischen Grades eines

Doktor-Ingenieurs

genehmigten Dissertation.

Vorsitzender:		Univ.-Prof. Wolfgang Polifke, Ph.D.
Prüfer der Dissertation:	1.	Univ.-Prof. Dr.-Ing. Nikolaus A. Adams
	2.	Prof. Dr.-Ing. Stefan Hickel Delft University of Technology, The Netherlands

Die Dissertation wurde am 17.12.2015 bei der Technischen Universität München eingereicht und durch die Fakultät für Maschinenwesen am 05.10.2016 angenommen.

Felix Örley
Heßstraße 19
80798 München
Germany

felix.oerley@tum.de

Released December 31, 2015
Typesetting LaTeX

Abstract

Numerical simulations offer great potential to gain insight into the flow dynamics of high pressure Common Rail Diesel injection systems. In this work, we develop the necessary building blocks to perform Large-Eddy Simulation (LES) of turbulent, cavitating flows in Diesel injection systems including needle movement. All tools are implemented into the block-structured in-house code *INCA* of the Institute of Aerodynamics and Fluid Mechanics of the Technische Universität München.

For representing complex, moving immersed solid boundaries on Cartesian grids, the conservative immersed interface method is improved and extended to allow for the simulation of weakly compressible fluid flows. By introducing an exact reconstruction of the cut-cell properties directly based on a surface triangulation of the immersed boundary, we are able to recover a flow evolution free of numerical artefacts. We validate our method with canonical flows and demonstrate that the method allows for an accurate prediction of flow problems around moving obstacles also in liquid flows with cavitation.

The cavitation model is based on a thermodynamic equilibrium assumption. We present an extension of the single-fluid cavitation model to a monolithic, Eulerian two-fluid two-phase model, which enables the LES of nozzle and jet flows without domain-coupling. The model easily integrates different fluid descriptions, such as cavitating water and cavitating ISO4113 Diesel fuel with a non-condensable gas component. We study the collapse of isolated single bubbles, as well as the primary break-up of cavitating liquid jets. The investigation reveals that three main mechanisms promote primary jet break-up: collapse-induced turbulent fluctuations near the outlet, entrainment of free gas into the nozzle, and collapse events inside the jet near the liquid-gas interface.

The analysis of the flow field inside a 9-hole common rail Diesel injector during a full injection cycle of ISO 4113 Diesel fuel into air reveals that the opening and closing phase are dominated by small-scale turbulence. During the main injection phase, large vortical structures are formed in the needle volume and reach into the nozzle holes. Violent collapse events of cavitation structures are detected during the closing phase in the nozzle holes, and after closing in the sac hole region. A comparison with LES results with a fixed injector needle at different lift positions shows a good agreement for large needle lifts, while the needle movement has significant effects on of important flow features at low needle lifts.

Acknowledgements

The following work has been created during my time as a research assistant at the Institute of Aerodynamics and Fluid Mechanics at the Technische Universität München. At this point, I would like to thank a number of people without who contributed to the success of this work.

First, I would like to thank my supervisor, Prof. Dr. Nikolaus Adams, for his guidance and support during the last four years. By promoting creative and open minded scientific thinking at the institute, I was encouraged to approach different topics related to the field of numerical simulation and modeling over the years, and knew that he would always have my back any time, if necessary.

I would like to especially thank Stefan and Steffen for teaching me in the fields of fluid dynamics, cavitation, numerics, and many more. Thanks for ironing out those little coding flaws from time to time ;-) The same goes for the whole cavitation group: thanks for all the discussions and fun we had. It was a great time working and travelling with you! Special thanks to Bernd and Steffen for proofreading this thesis and giving constructive suggestions.

Many thanks also go to one of the most important persons at the institute, Angela. Thank you for your patience and for managing all the little things that really help us and make our life so much easier!

Without my office mates, more than four years would have probably seemed like a very long time. Thank you so much, Angelina, Christoph, Vito, and Jan, that the spirit in MW1677 and outside work was always so positive and fun, and that mutual chocolate and cappuccino support was never short.

What really will remain in my memory is the good times I had with all colleagues at the institute. Over the years, extraordinary friendships developed on the foundation working, suffering, and partying together. Thank you all so much for making this time so exciting and fun!

Most of all, I would like to thank my parents and my family. Without your support, neither my studies, the semesters abroad, nor my doctorate studies would have been possible.

Very special thanks go to Birgit. Thank you for all your strong support in all aspects of life and your patience during the past years!

List of Publications

During this PhD project, several journal publications and conference contributions have been published. This work is partly based on these contributions to the scientific community and text sections have been reproduced in this thesis under the permission of the corresponding publisher.

Peer–Reviewed Journal Papers

[132] Örley, F., Pasquariello, V., Hickel, S., and Adams, N. A. (2015).
Cut-element based immersed boundary method for moving geometries in compressible liquid flows with cavitation.
Journal of Computational Physics, 283(C), 1-22. doi:10.1016/j.jcp.2014.11.028

My contribution to this work was the development of the extension of the method and the implementation in the in-house code INCA. I tested and validated the algorithms, performed the numerical simulations including grid generation and postprocessing, and wrote the manuscript for the publication.

[134] Örley, F., Trummler, T., Hickel, S., Mihatsch, M., Schmidt, S. J., and Adams, N. A. (2015).
Large-eddy simulation of cavitating nozzle flow and primary jet break-up.
Physics of Fluids, 27(8), 086101, doi:10.1063/1.4928701

My contribution to this work was the preliminary development of the method and implementation in the in-house code INCA. I supervised the student who generated the grid and performed initial simulations and test cases. I conducted the final numerical simulations and postprocessing, and wrote the manuscript for the publication.

[131] Örley, F., Hickel, S., Schmidt, S. J., and Adams, N. A. (2015).
Large-Eddy Simulation of turbulent, cavitating fuel flow inside a 9-hole Diesel injector including needle movement.
International Journal of Engine Research, doi:10.1177/1468087416643901

My contribution to this work was the development of the simulation setup and the implementation in the in-house code INCA. I tested and validated the algorithms, performed the numerical simulations including grid generation and postprocessing, and wrote the manuscript for the publication.

Conference Proceedings

[129] Örley, F., Grilli, M., Hickel, S., Schmidt, S., and Adams, N. A. (2013).
Application of Immersed Boundary Methods for the Investigation of Cavitating Liquid Flows Interacting with Moving Geometries.
Presented at the Joint EUROMECH / ERCOFTAC Colloquium 549 'Immersed Boundary Methods: Current Status and Future Research Directions', June 17-19 2013, Leiden, The Netherlands.

[135] Örley, F., Trummler, T., Hickel, S., Mihatsch, M.S., Schmidt, S.J. and Adams, N.A. (2015).
LES of Cavitating Nozzle and Jet Flows.
Direct and Large-Eddy Simulation X, Springer (in press)
presented at: ERCOFTAC Workshop DLES 10, May 27-29, 2015, Limassol, Cyprus.

[133] Örley, F., Trummler, T., Hickel, S., Mihatsch, M.S., Schmidt, S.J. and Adams, N.A. (2015).
Large-eddy simulation of cavitating nozzle and jet flows.
Journal of Physics: Conference Series, 656(1), 012096.
presented at: 9th International Symposium on Cavitation (CAV2015), Dec. 6-10, 2015, EPFL, Lausanne, Switzerland

[130] Örley, F., Hickel, S., Schmidt, S.J. and Adams, N.A. (2015).
LES of cavitating flow inside a Diesel injector including dynamic needle movement.
Journal of Physics: Conference Series, 656(1), 012097.
presented at: 9th International Symposium on Cavitation (CAV2015), Dec. 6-10, 2015, EPFL, Lausanne, Switzerland

Peer–Reviewed Journal Papers as Co–Author

[137] Pasquariello, V., Hammerl, G., Örley, F., Hickel, S., Danowski, C., Popp, A., Wall, W. A., and Adams, N. A. (2016).
A cut-cell Finite Volume-Finite Element coupling approach for fluid-structure interaction in compressible flow.
Journal of Computational Physics, 307(C), 670-695. doi:10.1016/j.jcp.2015.12.013

Table of Contents

List of Figures

List of Tables

1 Introduction

1.1 Motivation

Technical progress in the automotive industry is strongly driven by the desire to enhance sustainability. This goal is directly linked to the reduction of emissions of greenhouse gases, which is a key factor to fight global warming. Transport accounts for approximately 25% of the global CO_2 emissions [6, 20]. A major part hereby is caused by passenger cars [112].

Consequently, legislative rules of the European Union demand a reduction in CO_2 emissions [50] and limit particulate matter mass for Diesel engines since 2015 to not exceed a value of 0.005 g/km (EU6) [51]. To meet future emission standards, automotive manufacturers and suppliers focus, for example, on the optimization of combustion engines. Modern fuel injection systems play a key role by offering a more efficient mixing and combustion process, which thus have a direct impact on fuel economy and emissions ratings [21, 140]. With the possibility of using direct injection in gasoline and Diesel engines, intense research focuses on the development of direct injection fuel injectors.

Direct injection is an established method to create an inflammable fuel-air-mixture in the engine's combustion chamber. Traditional spark ignited engines use a premixed fuel-air mixture, which limits the compression ratio because of the possibility of knock. Spark ignited engines are usually designed to deliver compression ratios of 7:1...13:1 [150]. The

injection of fuel only after the compression stroke, in contrast, allows for higher compression ratios of the unburnt fuel-air-mixture ranging from 16:1...24:1, thus generating a higher output of work during one cycle [77]. Since the combustion process is triggered by auto-ignition, direct injection becomes especially important in Diesel engines. The fresh air in the combustion chamber undergoes substantial compression, which is increasing the gas temperature, and finally causes the fuel to ignite. With the current push for regulation of fuel usage efforts are also taken for spark-ignited engines to use direct injection, since direct injection here also offers great potential [166, 189].

Recent developments in direct Diesel injection systems, but also in gasoline injection systems, have increased the rail pressures to more than 2500 bar for Diesel injectors [66] and 1000 bar for gasoline injectors [166]. This trend aims at enhancing jet break-up and mixing to improve combustion and reduce emissions. Higher flow acceleration, however, implies thermo-hydrodynamic effects, such as cavitation, which occurs when the liquid evaporates locally [16]. The subsequent collapse of such vapor structures, when convected into regions of higher pressure, causes strong shock waves in the surrounding fluid. When vapor bubbles collapse near a solid wall, intense shock waves and high-velocity liquid jets directed towards the wall surface are created [56, 144, 179]. Structure loads in this case can lead to material erosion, which may be so strong that injection performance degrades severely or devices may fail [5, 42]. On the other hand, these loads are also employed to clean injection nozzle holes and thottles from surface deposits [18, 128], and they can promote primary jet break-up [108, 134, 151, 178]. Furthermore, two-phase flows can be used to maintain choked nozzle conditions, that is, a pressure-drop independent mass flow rate [139].

1.2 Introduction to Direct Injection Systems

A simplified schematic of a common rail (CR) Diesel injection system is shown in Fig. 1.1. A large variety of designs for injection systems has been developed, which have been tailored for their specific field of operation. In the following, we briefly discuss the operation of a sac-hole solenoid CR injector. For a detailed discussion see, e.g., Reif [150].

The functional components of the injector are summarized in Tab. 1.1. The device is connected to the high pressure reservoir system via the feed line, A. The feed line on the upper side links the control chamber B with the connection volume C via the Z-orifice, D. The Z-orifice hydraulically decouples the control chamber from the rail. On the lower side, the feed line directly connects to the ring chamber, E. When the injector is in the closed state, Fig. 1.1(a), the control and ring chamber are under equal pressure and, together with the needle spring, F, maintain a net downward force acting onto the injector needle, G. The needle is thus pressed into the needle seat, H, and seals the injector.

When the control valve, I, opens, mass leaks from the control chamber via the A-orifice, J, and the pressure in the plenum drops, Fig. 1.1(b). The control valve is connected to a solenoid or piezo control unit (not shown here), which allows for small, but fast displacements of the valve piston. The force imbalance on the injector needle due to the high rail pressure lifts the needle and fuel injection is initiated. Fuel passes the nozzle

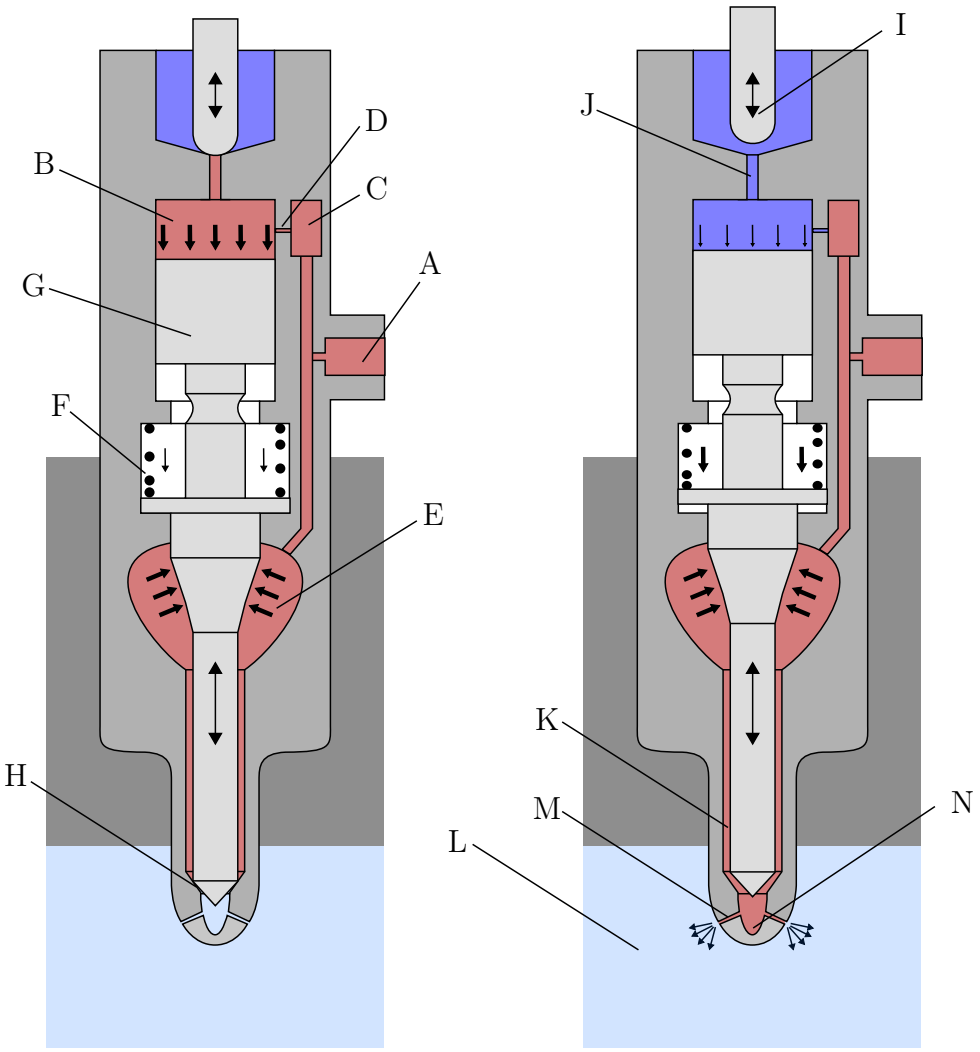

(a) closed state (b) open state

Figure 1.1: Simplified schematic of a common rail injection system. Red and blue colors mark regions of high and low pressure, respectively.

line, K, and is injected into the combustion chamber, L, via the nozzle holes, M, which connect to the sac volume, N. At the end of the injection cycle, the control valve is closed and the force balance is recovered, which closes the injector.

Cavitation is employed to control a desired mass flux passing the Z- and A-orifice under choked conditions. In the needle seat, as well as on the needle tip and inside the nozzle holes often undesired cavitation erosion is found, which stems from strong collapse events of vapor clouds in these regions.

Table 1.1: Nomenclature for simplified common rail Diesel injector

Symbol	Name
A	Feed line
B	Control chamber
C	Connection volume
D	Z-orifice
E	Ring chamber
F	Needle spring
G	Injector needle
H	Needle seat
I	Control valve
J	A-orifice
K	Nozzle line
L	Combustion chamber
M	Nozzle holes
N	Sac volume

1.3 Numerical Simulation of Injection Systems

Understanding the flow phenomena inside an injection system is necessary to quantify the effects of turbulence and cavitation, and their influence on jet and spray characteristics. Characteristic fuel nozzle dimensions inside Diesel injectors usually are in the range of tens to several hundred micrometers, which makes the instrumentation with diagnostic equipment for an experimental flow characterization challenging [14, 126]. Other limiting factors are high operating pressures and short intrinsic timescales imposed by inherent flow dynamics, by functional components such as opening or closing of control valves or the injector needle, or by multiple injections per engine cycle. Experimental assessment of erosion damage can supply information about regions of high structural stresses, which may be linked to the occurrence of cavitation [55], but still does not provide access to all aspects of the underlying flow dynamics needed for optimization. Computational Fluid Dynamics (CFD) can provide time-resolved information on flow structures in arbitrary small geometries. Detailed numerical simulations of cavitating flows thus have become an increasingly important tool in the design process of injection systems.

The computational approach involves a number of fundamental modelling assumptions.

1. Realistic industrial applications usually involve complex geometries. In addition to the modelling of stationary components, the simulation of moving bodies may become especially challenging and costly.

2. Flows of technical relevance are often dominated by turbulence. In these kinds of flows, the smallest scales account for a large part of the energy dissipation and therefore play a key role in the macroscopic flow behaviour.

3. The accurate prediction of cavitation is crucial for assessing the overall flow dynamics. Multiple cavitation models have been developed over the last years, which feature different complexity and thus applicability to industrial problems.
4. Since the realistic injection of fuel usually involves gas in the combustion chamber, the interaction of (cavitating) liquid jets with a gaseous phase becomes important.

In the following, each of these aspects is briefly discussed in the context of numerical simulations of injection systems.

1.3.1 Grid Generation and Moving Geometries

In an industrial context, the numerical method should provide a simple and easy grid generation, while technical components of complex shape should be represented with high accuracy. The most common approaches for grid generation can be summarized as *body-conforming grids* and Cartesian grids using *immersed boundary methods*.

A widely used method for geometry representation is to apply *body-conforming grids*. Mesh generation for structured grids in the pre-processing can be very time consuming. As an alternative, unstructured grids may result in a higher number of mesh cells, larger numerical errors, and a deterioration of computational efficiency.

The representation of moving obstacles in body-conforming grids by a *remeshing strategy* is computationally very costly and can result in a severe degradation of the quality of the results. Moreover, in the context of numerical simulation of realistic injection cycles, the representation of closing and opening narrow gaps is difficult or even impossible, since the timestep based on the CFL criterion becomes arbitrarily small for cells in the gap region. *Chimera techniques* partition the computational domain into a system of geometrically simple, body fitted overlapping grids [87], and are therefore better suited for simulations of gap regions. Boundary information is exchanged between the underlying grids by interpolation of the flow variables. The chimera technique often suffers from strong pressure oscillations due to large non-conservative interpolation errors in practical, three-dimensional cases [94], and is thus of very limited applicability to cavitating flows.

A highly performant alternative is to compute the flow field on simple Cartesian grids, which facilitate the implementation of high order numerical schemes, and to use an *immersed boundary approach* introduced by Peskin [142] to represent arbitrarily complex geometries. Due to the relatively simple grid, the mesh generation is greatly simplified and the treatment of moving geometries is facilitated. In their review of immersed boundary methods, Mittal and Iaccarino [124] distinguish two fundamental approaches, namely the *continuous* and *discrete forcing* technique.

The *continuous forcing technique* introduces a source term into the governing equations, which is smeared over multiple cells across the fluid-solid interface to fulfil the boundary condition in an approximate manner [52, 68, 143, 153]. A coupling of fluid-field and rigid-structure motion has been successfully investigated, e.g., by De Tullio *et al.* [29, 30]. Although implementation of the model is straightforward and such techniques are able to handle geometries of large complexity including moving obstacles [25, 191], a drawback

of these methods is the spurious loss or production of mass, momentum and energy at the interface [93, 96]. Such non-conservativity poses a particular issue for Large-Eddy Simulations (LES), which employ coarse grids and rely on an accurate prediction of physical flow behavior in near-wall regions over large time scales.

The *discrete forcing approach*, developed by Verzicco et *al.* [191] and Mohd-Yusof [125], introduces a predictor-corrector formulation using a discrete forcing function in the momentum equations for enforcing a wall boundary condition. This approach allows for an accurate representation of the boundary interface, but still lacks discrete conservativity.

The conservativity issue is met with *Cartesian cut-cell methods*, which were first introduced by Clarke *et al.* [23] and Gaffney *et al.* [57] for inviscid flows and later extended to viscous flows by Udaykumar *et al.* [186, 187, 188] and Ye *et al.* [196]. In this method the control volumes at the boundaries are reshaped to fit locally the boundary surface with a sharp interface. Representing a consistent extension of the finite volume method, the conservation laws are strictly fulfilled both locally and globally [53]. A drawback of cut-cell methods is that the fluid volume fraction of cut-cells may become very small and therefore can lead to numerical instability with explicit time integration schemes, or poor convergence with implicit methods. A stabilization of the underlying scheme is therefore required. One way to achieve stable time integration is to employ the cell-merging technique introduced by Ye *et al.* [196] and Bayyuk *et al.* [10], where the fluid part of cut-cells, whose center is located within the solid, is merged with adjacent fluid cells. The cell merging process introduces additional complexity into the numerical framework, since the computational stencil for all cells adjacent to the merged cell and for the merged cell itself becomes different from that of regular internal cells. Therefore, Kirkpatrick *et al.* [97] propose cell-linking rather than merging. A second approach, which is usually referred to as flux redistribution, was introduced by [24, 141]. The authors apply a redistribution of the difference in mass and momentum flux to neighboring cells in a way that preserves stability and local conservation. Joining the two methods, the so-called mixing procedure, in which a cut-cell is mixed with one (cell linking) or multiple (flux redistribution) surrounding cells in a conservative way, was proposed by Hu *et al.* [86] for two dimensions and a compressible flow description. The method was revised and extended to multi-dimensional problems by Lauer *et al.* [104]. Meyer *et al.* [114, 115, 116] have developed a second-order accurate conservative immersed interface method based on a cut-cell method with conservative mixing procedure for incompressible flows. Meyer *et al.* [114, 115, 116, 117] demonstrate good performance and accuracy for laminar and turbulent flows. Applications to rigid moving-boundary problems in a compressible multi-dimensional framework were reported by Grilli *et al.* [70] for laminar flows at a wide range of Mach numbers, by Günther *et al.* [73, 74] for the simulation of opening and closing of gaps in internal flows of combustion engines, and by Schneiders *et al.* [164] for the interaction of multiple elastically mounted cylinders and pitching airfoils.

1.3.2 Turbulence Modeling

Until now, the accurate modelling of turbulence is one of the larges fields of ongoing research in CFD. Over the years, three approaches, which differ in their level of compu-

tational complexity and accuracy, have been established and are used today in academia and industry.

Some authors suggest that turbulence does not play a major role in cavitating nozzle flows, see, e.g., Macian *et al.* [109] and Salvador *et al.* [155]. Many numerical and experimental studies, on the other hand, have shown that the interaction of turbulence and cavitation is of high importance to capture dominant flow features.

In *Direct Numerical Simulations* (DNS), all temporal and spatial scales, which range from the smallest scales (Kolmogorov microscales), up to the integral length scales, are fully resolved. The computational requirements in terms of grid points scale with $N \sim Re_L^{9/4}$ [19], where $Re_L = UL/\nu$ is the Reynolds number, which is proportional to the characteristic velocity U, the characteristic length scale L, and the inverse of the kinematic viscosity ν. For the applications in Diesel injection systems, which involve large Reynolds numbers inside the nozzle holes, this approach is not feasible and is only applied to study isolated sub-systems, see, e.g., Duret *et al.* [43].

Early studies of cavitating nozzle and injector flows were performed by solving the incompressible (unsteady) *Reynolds-Averaged Navier-Stokes equations* (RANS). This modelling approach has low computational cost, but may be prone to strong modelling errors. In an industrial environment, this method is state of the art for application in the development process. This includes simulations of submerged injection nozzles by Andriotis *et al.* [3], Giannadakis *et al.* [62] and, more recently, Reid *et al.* [149]. Further examples discuss cavitating duct flows and single hole injectors [59, 92, 147, 167, 198], five-hole injectors [122], and six-hole injectors [173, 176].

Befrui *et al.* [12] and Duke *et al.* [40], on the other hand, expect that large vortical structures within the nozzle flows strongly interact with cavitation structures in multiphase flows and therefore suggest performing *Large-Eddy Simulations* (LES). At a higher cost than RANS, but significantly lower cost than DNS, this method offers high accuracy and is especially suited for unsteady processes. Recent studies by Desantes *et al.* [32] for six-hole injectors present results for various, but steady, needle lifts with incompressible LES.

1.3.3 Cavitation Modeling and Fluid Compressibility

Based on the pioneering work of Plesset *et al.* [145, 146] on the growth and collapse of isolated bubbles for different boundary conditions, d'Agostino and Brennen [27] and Delale *et al.* [31] developed one-dimensional models of bubbly liquids. Since then, various cavitation models have been proposed, which can be categorized into two main groups: *two-fluid models* and *single-fluid models*. A comprehensive overview is given in Giannadakis *et al.* [64] and Battistoni *et al.* [8].

With *two-fluid cavitation models*, an individual set of conservation equations is solved for each species. Eulerian-Eulerian two-fluid models incorporate a mass transfer due to phase transition between liquid and vapor phases at the phase boundary, which can be

tracked by a sharp-interface method as proposed by, e.g., Lauer *et al.* [103, 104]. Eulerian-Lagrangian two-fluid cavitation models, as investigated by Giannadakis *et al.* [63, 64], consider the liquid as a continuous carrier phase in a Eulerian frame of reference, whereas single vapor bubbles or parcels of bubbles are tracked as Lagrangian elements using the Rayleigh-Plesset equation for growth and collapse.

Single-fluid cavitation models, which are sometimes referred to as homogenous Eulerian models, on the other hand treat the fluid as a continuous mixture of liquid and vapor and solve a single set of conservation equations characterized by average mixture properties, such as mixture density and mixture viscosity. The void fraction can additionally be transported separately as with Volume-of-Fluid (VOF) methods [85], allowing for inclusion of non-equilibrium phase transition as proposed by Kunz *et al.* [100] or Yuan *et al.* [198]. Assuming the liquid and gaseous phase to be in thermal and mechanical equilibrium, Schmidt *et al.* [159, 160] and Schnerr *et al.* [165] developed a model in which the two phases are uniformly distributed within each cell without slip between the liquid and vapor phases, neglecting surface tension and buoyancy effects. Thermodynamic equilibrium models exhibit an intrinsic length-scaling capability, see Schmidt *et al.* [162], and thus are especially suited for the application in complex flow environments, which include the interaction with subgrid-scale models for non-resolved flow scales [48].

Some approaches discussed above are based on an *incompressible* description of the governing equations. Schnerr *et al.* [165], on the other hand, argue that considering *compressible* effects for the simulation of cavitating flows to resolve wave dynamics is necessary. This approach allows for the prediction of acoustic cavitation, and for the assessment instantaneous pressure fields for predicting surface loads. A compressible LES method in the context of nozzle cavitation in a gasoline injector is, e.g., presented by Ishimoto *et al.* [90].

1.3.4 Multi-Fluid Modeling

A particular challenge in the context of fuel injection into a combustion chamber is the interaction of cavitating liquids with a non-condensable gas phase. Sou *et al.* [174, 175] and Som and Aggarwal [172] find that collapse events of cavitation structures near the nozzle outlet may enhance turbulent fluctuations, which in turn promote primary break-up of the liquid jet. This effect is observed at a supercavitating state of the nozzle, i.e., when stable cavitation sheets reach from the inlet edge of the nozzle to the outlet region, see also Shibata *et al.* [170]. A simultaneous simulation of the cavitating nozzle flow and the liquid jet is necessary to capture the effect of cavitation structures on jet break-up. Models in the literature can be classified into *Lagrangian* and *Eulerian* multi-fluid models. Additionally, hybrid approaches, so-called *Eulerian-Lagrangian*, are distinguished.

Lagrangian particle methods introduced by Dukowicz [41] significantly reduce the required mesh resolution and are adopted by Som *et al.* [173], who consequently consider the effects from nozzle flows when coupling with a subsequent spray simulation.

To correct for potential inconsistencies of the two-phase models in the two separate simulations, a combination of the models denoted as *Eulerian-Lagrangian*-Spray and Atomization (ELSA) model by Blokkeel *et al.* [15] switches from a Eulerian description of the nozzle flow to a Lagrangian particle simulation of liquid droplets in the break-up region. This approach, however, does not incorporate compressibility effects inside the liquid. Wang *et al.* [193] propose an eight-equation model based on the work of Saurel *et al.* [157, 158], to assess both internal and external 2-D nozzle flows simultaneously including cavitation effects by a stiffened gas equation of state, whereas gas and vapor are represented as one single miscible phase.

Simulations of breaking liquid jets were recently presented by Menard *et al.* [113] and Desjardins and Pitsch [33] in an *Eulerian* framework with a VOF method. The authors apply the method only to external flows. To assess the impact of two-phase nozzle flow additional simulations of nozzle flows are required. Battistoni *et al.* [8] compare a non-equilibrium thermal mixture model with an *Eulerian multi-fluid* description with Rayleigh bubble dynamics for phase change. In their simulations of cavitating nozzle flows a free gas content was considered, but effects on the primary jet break-up were not assessed. Ishimoto *et al.* [90] performed the first fully coupled simulation of cavitating nozzle flow and jet break-up with a fully compressible, barotropic LES model based on a VOF method.

1.4 State of the Art: Diesel Injector Simulations

Recently, several attempts to include the full, realistic geometry of the Diesel injection system in numerical simulations to assess the interaction of needle movement onto the liquid jet during the injection process were presented.

Margot *et al.* [110] studied a sac-type single-hole injector using an incompressible RANS approach with a moving mesh strategy. The authors found that the flow inside the nozzle and near the exit is strongly affected by the needle position. Greif *et al.* [67] presented numerical RANS results with an Eulerian multi-fluid model for an eight-hole injector. In their work, also the effect of off-axis needle displacement in multi-hole injectors was studied. Unsteady needle lift was based on re-meshing the fluid domain. RANS studies of a six-hole including a unsteady needle lift were conducted by He *et al.* [76] and Brusiani *et al.* [17] using a moving mesh strategy. The studies again confirmed that the needle motion is an important parameter to be considered in realistic simulations. Arienti and Sussmann [4] presented incompressible simulations of one- and six-hole injectors including unsteady needle lift by a levelset-based Cartesian cut-cell immersed boundary method. The authors studied the effect of needle motion onto jet break-up, but did not include a cavitation model. To the authors' knowledge, Battistoni *et al.* [9] were the first to apply a Cartesian cut-cell method to simulate five-hole Diesel injector nozzle and jet flow characteristics. The authors applied the method to study the effect of off-axis movement onto the flow field, but no particular focus was put on assessment of cavitation erosion prediction. The same holds for the studies of Zhao *et al.* [199]. Koukouvinis *et al.* [98] recently for the first time correlated pressure peaks caused by vapour pocket collapse

events with surface erosion in industrial injectors using a fully compressible LES model including a moving needle.

In the literature presented above, all authors concluded that needle movement is important in the investigation of injection processes. Cavitation has been studied by most of the authors, but has not been discussed in detail. An evaluation in terms of structural erosion risk during the injection remains an open question. Many studies furthermore only consider submerged nozzles, and neglect the effect of non-condensable gas. In this thesis, we aim at addressing these challenges.

1.5 Contribution and Accomplishments

In this work, we follow an immersed boundary approach for representing the fluid-solid-interface. We apply a compressible implicit LES model, which is paired with a homogenous mixture cavitation model to study the dynamics of turbulence and cavitation inside injection systems. An Eulerian two-fluid two-phase mixture model for the liquid-gas interface is chosen.

The main technical achievements for the numerical simulation of complex flows and the physical insights into fluid dynamics related to Diesel injection systems gained during the course of this work are:

1. Development and validation of an extension to the existing Conservative Immersed Interface Method (CIIM) of Meyer *et al.* [114, 115, 116] and Grilli *et al.* [70] for the simulation of cavitating liquids interacting with moving boundaries.
2. Development of a generalized thermodynamic description for cavitating liquids with different equations of state to compute fuel flows inside injection systems.
3. Extension and validation of existing cavitation models to a two-fluid formulation to study the effect of non-condensible gas onto jet break-up.
4. Numerical simulation of the flow inside a nine-hole solenoid common rail (CR) Diesel injector including the unsteady needle movement during a full injection cycle.

1.6 Outline

This thesis is divided into seven chapters. All chapters are summarized at the end of the corresponding section. After the introduction, the physical model and governing equations are presented in Chapter 2. The focus here is put on the thermodynamic models and solution strategies utilized in this work. In Chapter 3, the numerical method is described, which includes a brief introduction to Implicit Large-Eddy Simulation and the modifications of the ALDM scheme applied for cavitating flows. Furthermore, details on the cut-element based conservative immersed boundary method are presented. In Chapter 4, the novel immersed boundary method is validated against well-established

test-cases, such as the flow around an oscillating cylinder in a fluid at rest, an in-line oscillating cylinder in a free stream, and two moving cylinders interacting with each other. We moreover show results for a cavitating 2-D mixer and for a closing 3-D high-pressure single-fluid liquid fuel injector control valve with inertia-induced and turbulence-induced cavitation. A validation for the thermodynamic single-fluid two-phase and two-fluid two-phase model is provided in Chapter 5. In this section, we simulate single bubble collapse events, and an experimental reference configuration of a cavitating water jet injected into air. We reveal the main mechanisms for the early stages of primary break-up of cavitating liquid jets. Finally, numerical simulation results for the flow field inside a nine-hole solenoid injector during an instationary injection process is presented in Chapter 6. The work is concluded in Chapter 7, where the main findings are summarized and an outlook for future work is given.

2 Physical Model

In the following chapter the governing physical equations for the description of a fluid and the thermodynamic closure models applied in this work are introduced.

This section has partially been published in Örley et al. [131, 132, 134].

2.1 Governing Equations

We consider the three-dimensional, fully compressible Navier-Stokes equations in conservative form

$$\frac{\partial \mathbf{U}}{\partial t} + \nabla \cdot \mathbf{F}(\mathbf{U}) = 0. \tag{2.1}$$

The state vector $\mathbf{U} = [\rho, \rho u_1, \rho u_2, \rho u_3, \rho E, \rho \xi]$ contains the conserved variables density ρ, momentum $\rho \mathbf{u}$, internal energy $\rho E = \rho e + \frac{1}{2}\rho u_k u_k$, and fluid mass fraction $\rho \xi$, if required by the thermodynamical model. The numerical flux vector $\mathbf{F}(\mathbf{U})$ is divided into advection

$\mathbf{C}_i(\mathbf{U})$, and surface stresses due to pressure $\mathbf{P}_i(\mathbf{U})$ and shear $\mathbf{S}_i(\mathbf{U})$ as

$$\mathbf{F}_i(\mathbf{U}) = \mathbf{C}_i(\mathbf{U}) + \mathbf{P}_i(\mathbf{U}) + \mathbf{S}_i(\mathbf{U}) = \begin{bmatrix} u_i\rho \\ u_i\rho u_1 \\ u_i\rho u_2 \\ u_i\rho u_3 \\ u_i E \\ u_i\rho\xi \end{bmatrix} + \begin{bmatrix} 0 \\ \delta_{i1}p \\ \delta_{i2}p \\ \delta_{i3}p \\ u_k\delta_{ik}p \\ 0 \end{bmatrix} - \begin{bmatrix} 0 \\ \tau_{i1} \\ \tau_{i2} \\ \tau_{i3} \\ q_i \\ 0 \end{bmatrix}, \tag{2.2}$$

where p is the static pressure and τ_{ij} denotes the viscous stress tensor

$$\tau_{ij} = \mu\left(\partial_j u_i + \partial_i u_j - \frac{2}{3}\delta_{ij}\partial_k u_k\right), \tag{2.3}$$

with μ being the dynamic viscosity. The heat flux, where applicable, is computed from Fourier's law

$$q_i = k\partial_i T, \tag{2.4}$$

with k being the heat conductivity of the fluid and T the static temperature.

2.2 Thermodynamic Models

For closing the Navier-Stokes equations introduced in Eq. 2.1, a suitable equation of state is necessary. In this work, we either use ideal gas, or liquid fluid flows including phase change and an optional non-condensable gas component. The pure liquid, liquid-vapor-mixture, and non-condensable gas components are denoted with subscript L, M, and G, respectively. In the following, the different equations of state and solution procedures for the individual models are introduced.

2.2.1 Gas Phase

For an ideal gas flow, we distinguish between a framework including full thermodynamics (i.e., with energy equation), and a barotropic approach, which can be isentropic, or, in this work, isothermal.

Ideal Gas

In the full thermodynamic case, the Navier-Stokes equations are solved in non-dimensional form. The pressure p is computed from the total energy

$$E = \frac{1}{\gamma - 1}p + \frac{1}{2}\rho u_i u_i. \tag{2.5}$$

The equation of state for an ideal gas is defined as

$$T = \kappa \mathrm{Ma}^2 \frac{p}{\rho} \tag{2.6}$$

with the reference Mach number Ma and the ratio of specific heats $\kappa = 1.4$. Temperature dependence of the viscosity and thermal conductivity is accounted for by a power law

$$\mu = \frac{T^{0.75}}{\mathrm{Re}} \tag{2.7}$$

and

$$k = \mu \frac{1}{(\kappa - 1)\mathrm{Ma}^2 \mathrm{Pr}} \tag{2.8}$$

with the reference Reynolds number, Re, and Prandtl number, Pr.

Isothermal, Ideal Gas

In the context of a two-fluid approach, see below, the gas phase is modelled as an isothermal, ideal gas

$$\rho_G = \frac{p}{\mathrm{R} T_{ref}} \tag{2.9}$$

at reference temperature $T_{ref} = 293.15$ K. R_G denotes the specific gas constant, we use $\mathrm{R}_G = 287.06$ J/(kg K) for air. The speed of sound for air at reference temperature is

$$c_G = \sqrt{\kappa \mathrm{R}_G T_{ref}} = 343.24 \text{ m/s}. \tag{2.10}$$

2.2.2 Single-Fluid Cavitation Model

In the following, the single-fluid cavitation model is presented. After a brief discussion of the homogenous mixture approach, we introduce cavitation models for liquid water and for ISO 4113 Diesel fluid.

Homogenous Mixture Cavitation Model

Assuming a high concentration of nuclei, a liquid starts to evaporate where the local pressure drops below a critical value, that is, $p < p_c$. A straightforward approach is to use the saturation pressure of the liquid phase [62, 198] as the critical pressure, i.e.,

$$p < p_{sat}. \tag{2.11}$$

The formation of vapor can then be modelled by a homogenous mixture model in thermal and mechanical equilibrium. The actual vapor-liquid interface, that may consist of several small vapor bubbles inside one computational cell, is not reconstructed, unlike with sharp-interface methods, e.g., Lauer et *al.* [103, 104]. Surface tension thus is neglected.

In the framework of a finite volume representation the cell-averaged density may be written as

$$\rho = \alpha_v \rho_{vap} + (1 - \alpha_v)\rho_{liq}, \tag{2.12}$$

where α_v denotes the vapor volume fraction, and ρ_{liq} and ρ_{vap} are the densities of liquid water and pure vapor, respectively. Assuming that phase change occurs instantaneously and in local thermodynamic equilibrium, the densities of liquid and vapor are $\rho_{liq} = \rho_{sat,liq}$ and $\rho_{vap} = \rho_{sat,vap}$ if $0 < \alpha_v < 1$. Hence we can compute the local vapor volume fraction from

$$\alpha_v = \frac{V_{vap}}{V} = \begin{cases} 0 & , \rho \geq \rho_{sat,liq} \\ \dfrac{\rho_{sat,liq} - \rho}{\rho_{sat,liq} - \rho_{sat,vap}} & , \text{else.} \end{cases} \tag{2.13}$$

V_{vap} denotes the part of the volume V that is occupied by vapor, and $\rho_{sat,liq}$ and $\rho_{sat,vap}$ are the saturation densities of liquid water and pure vapor, respectively.

The homogenous mixture cavitation model described below introduces separate equations of state for the liquid and the liquid-mixture phase, which are modelled independently and thus offer a way to include models of different complexity. Depending on the local vapor volume fraction, we switch between the barotropic equations of state for the pure liquid ($\alpha_v = 0$), and a liquid-vapor mixture ($0 < \alpha_v < 1$). Often thermodynamic tables may be used to relate the thermodynamic quantities of complex fluids. In this work, since no data for Diesel-like fluids is available and the analytical equations of state are easy to solve, we do not follow this approach.

The homogenous-mixture model for water and Diesel-like fluid flows has been extensively validated, e.g., for turbulent wall-bounded water flows by Hickel at *al.* [84], and LES of turbulent, wall-bounded fuel fuel flows in a generic throttle by Egerer et *al.* [48].

Single-Fluid Cavitation Model for Water based on Tait Equation

Saurel *et al.* [156] and, e.g., Schmidt *et al.* [163] propose to model liquid water as a barotropic fluid by a modified Tait law

$$\rho_L = \rho_{sat,liq} \cdot \left(\frac{p + B}{p_{sat} + B} \right)^{1/N}, \; p \geq p_{sat}, \tag{2.14}$$

where p_{sat} is the saturation pressure for water, and $N = 7.1$ and $B = 3.06 \times 10^8$ Pa are fluid-specific parameters, see Tab. 2.1. The saturation quantities are temperature dependent. Throughout this work we use numerical values of $p_{sat} = 2340$ Pa and $\rho_{sat,liq} = 998.1618$ kg/m^3 for water at a reference temperature of $T_{ref} = 293.15$ K. A comprehensive study of the Tait model is given by Sezal [169].

The speed of sound of the liquid phase can be computed from

$$c_L = \left(\frac{N \cdot (p + B)}{\rho} \right)^{1/2}. \tag{2.15}$$

Table 2.1: Fluid parameters for water at $T_{ref} = 293.15$ K.

Property	Unit	Value
N	[-]	7.1
B	$[\times 10^8\ Pa]$	3.06
p_{sat}	[Pa]	2340
$\rho_{sat,liq}$	$[kg/m^3]$	998.1618

Assuming phase change along an isentropic equilibrium path in the mixture region, we integrate the definition of the isentropic equilibrium speed of sound of a homogenized two-phase mixture [54]

$$c_M = c_{eq} = \frac{L\rho_{sat,liq}}{\sqrt{c_{p,liq}T}}\frac{1}{\rho} + HOT, \tag{2.16}$$

which introduces the latent heat L, and compute the local equilibrium density as

$$\rho_M = \left(\frac{1}{\rho_{sat,liq}} - \frac{p - p_{sat}}{C}\right)^{-1}, p \leq p_{sat}, \tag{2.17}$$

neglecting higher order terms, HOT. The parameter C, as well as the saturation density for vapor, $\rho_{sat,vap}$, are temperature dependent. For the chosen reference temperature $T_{ref} = 293.15$ K, we use the following numerical values: $C = 1468.54$ Pa kg/m^3 and $\rho_{sat,vap} = 0.01731$ kg/m^3.

Viscous effects in the two-phase fluid are considered by a mixture viscosity model following Beattie *et al.* [11] as

$$\mu = (1 - \alpha_v)\left(1 + \frac{5}{2}\alpha_v\right)\mu_{liq} + \alpha_v\mu_{vap}, \tag{2.18}$$

where the viscosities for the liquid water and vapor phase at the reference temperature are $\mu_{liq} = 1.002 \times 10^{-3}$ Pa s and $\mu_{vap} = 9.727 \times 10^{-6}$ Pa s, respectively.

Simplified Single-Fluid Cavitation Model for Water

To obtain a formulation for liquid water and water vapor to include in the two-fluid two-phase model, see below, a model based on the definition of the isentropic speed of sound

$$c^2 = \left.\frac{\partial p}{\partial \rho}\right|_{s=const} \tag{2.19}$$

is used. Assuming a constant speed of sound $c = const.$ for each phase, that is, liquid and liquid-vapor mixture, integration of Eq. 2.19 from saturation density to the cell averaged density leads to a linearized equation of state

$$\rho = \rho_{sat,liq} + \frac{1}{c^2}(p - p_{sat}). \tag{2.20}$$

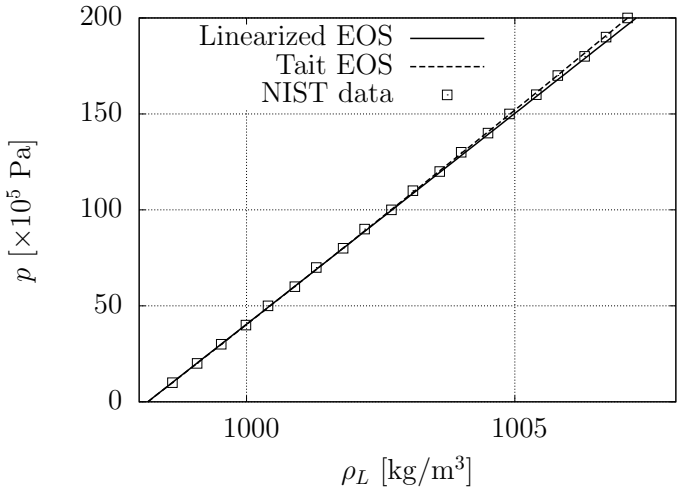

Figure 2.1: Comparison of linearized equation of state for liquid water to modified Tait equation [156] and NIST data [105].

Table 2.2: Relative error of linearized equation of state.

Pressure p [$\times 10^5$ Pa]	$\rho_{NIST}(p)$ [kg/m^3]	$\rho_{lin}(p)$ [kg/m^3]	$\lvert\varepsilon\rvert$
1.0	998.207	998.206	0.00038%
10.0	998.620	998.616	0.00042%
100.0	1002.692	1002.712	0.00116%
2000.0	1071.433	1089.179	1.41331%

For purely liquid water, that is, $p > p_{sat}$, the speed of sound is $c = c_L = 1482.35$ m/s at ambient conditions. Comparison to more accurate models, such as the modified Tait equation proposed by Saurel *et al.* [156], or NIST data for liquid water [105], shows negligible deviation even for high pressures, as shown in Fig. 2. The error of the linearized equation of state relative to accurate NIST data for liquid water [105]

$$\varepsilon = \frac{\rho_{NIST} - \rho_{lin}}{\rho_{NIST}} \tag{2.21}$$

is shown in Tab. 2.2 for a pressure range up to 2000 bar.

We assume that phase change occurs instantaneously and in local thermodynamic equilibrium. In this case, the same equation of state as introduced in Eq. 2.20 may be used, but a different speed of sound is employed.

Franc *et al.* [54] derive the equilibrium speed of sound in the two-phase region as

$$\frac{1}{\rho c^2} = \frac{\alpha}{\rho_v c_v^2} + \frac{1-\alpha}{\rho_l c_l^2} - \frac{(1-\alpha)\rho_l c_{p,l} T}{(\rho_v L)^2}. \tag{2.22}$$

Neglecting the last term results in the 'frozen' speed of sound. Franc *et al.* provide

numerical values for the two different definitions of the speed of sound at a void fraction of 50% in water, for the equilibrium state $c_{eq} = 0.08$ m/s, and for the frozen state $c_{frozen} = 3$ m/s. Brennen [16] finds that including phase-change effects results in a speed of sound which lies between these two bounds.

We consider an average of the speed of sound between a frozen and an equilibrium isentropic phase change in the two-phase region. We use a numerical value of $c = c_M = 1$ m/s in the two-phase region, which satisfies the observation of Brennen.

The combined equation of state for the liquid and liquid-vapor-mixture fluid component in a linearized approach is summarized as

$$\rho = \rho_{sat,liq} + \frac{1}{c^2}(p - p_{sat}), c = \begin{cases} c_L, & p \geq p_{sat} \\ c_M, & p < p_{sat} \end{cases}. \tag{2.23}$$

Single-Fluid Cavitation Model for ISO 4113 Diesel Fluid

For the simulation of ISO4113 air-free liquid Diesel-like fluid flows we apply a cavitation model based on the modified Tait equation, Eq. 2.14. This model is later extended to a generalized two-fluid two-phase model.

To determine the two fluid-specific parameters for the liquid phase of ISO 4113 Diesel fuel, N and B, we reformulate Eq. 2.14 and Eq. 2.15 as

$$\rho c^2 \left(\frac{\rho}{\rho_{sat,liq}}\right)^N - \rho c^2 - (p - p_{sat}) N \left(\frac{\rho}{\rho_{sat,liq}}\right)^N = 0 \tag{2.24}$$

and

$$B = \frac{\rho c^2}{N} - p. \tag{2.25}$$

We choose a specific reference state, $\{p_{ref}, \rho_{ref}, c_{ref}\}$, following Dongiovanni *et al.* [37], see Tab. 2.3. The saturation quantities for the pressure and density, p_{sat} and $\rho_{sat,liq}$ are found in Egerer *et al.* [48]. We assume a barotropic change of state at reference temperature $T_{ref} = 293.15$ K in the liquid regime. Actual inlet temperatures for realistic injectors in engines can be much larger. In the simulation of a nine-hole Diesel injector, unlike previous studies where we employ isentropic or fully energetic fluid models, we reproduce the underlying assumptions of the reference data of Huber and Ulbrich [88], who performed isothermal computations of the injection cycle at this reference temperature using a one-dimensional multi-domain simulation model.

The numerical values for the Tait coefficients N, B, as well as the saturation quantities p_{sat} and $\rho_{sat,liq}$ for ISO 4113 Diesel fluid at the reference temperature are summarized in Tab. 2.4.

We compare our model with an equation of state proposed by Dongiovanni *et al.* [37],

$$\rho(p, T) = K_{\rho 1} + \left[1 - exp\left(-\frac{p}{K_{\rho 2}}\right)\right] K_{\rho 3} p^{K_{\rho 4}}, \tag{2.26}$$

Table 2.3: Reference point for computation of Tait parameters.

Property	Unit	Value
p_{ref}	[$\times 10^8$ Pa]	1.0
ρ_{ref}	$[kg/m^3]$	864.7
c_{ref}	$[m/s]$	1704.8

Table 2.4: Fluid parameters for isothermal ISO 4113 Diesel fluid at $T_{ref} = 293.15$ K.

Property	Unit	Value
N	[-]	11.469
B	[$\times 10^8$ Pa]	1.191
p_{sat}	[Pa]	2218.0
$\rho_{sat,liq}$	$[kg/m^3]$	819.627

where $K_{\rho 1} = 822.8$ kg/m^3, $K_{\rho 2} = 145.8$ Pa, $K_{\rho 3} = 0.213$ kg/m Pa$^{-K_{\rho 4}}$, and $K_{\rho 4} = 0.76$ are here evaluated at T_{ref}. Our model for the liquid phase based on the Tait equation is in good agreement with reference data for pressures up to over 2000 bar, see Fig. 2.2.

In the two-phase region, that is, $p < p_{sat}$, we use a formulation of the linearized equation of state based on the integrated form of the isentropic speed of sound, see Eq. 2.20, and choose a constant mixture speed of sound

$$c_M = \left(\frac{p_{sat}}{\rho_{sat,liq}} \right)^{1/2}. \tag{2.27}$$

This leads to the linearized equation of state

$$\rho_M = \rho_{sat,liq} + \frac{1}{c_M^2}(p - p_{sat}),\ p < p_{sat}. \tag{2.28}$$

We limit the density to a value of $\alpha_{v,lim} = 99.5\%$.

Numerical values for the viscosities for the liquid and vapor phase of ISO4113 Diesel fuel at the reference temperature are $\mu_{liq} = 3100 \times 10^{-6}$ Pa s and $\mu_{vap} = 0.1 \times 10^{-6}$ Pa s, respectively.

2.2.3 Multi-Fluid Model for Cavitating Flows

The homogenous-mixture single-fluid model for cavitation introduced in Sec. 2.2.2 is extended by a component of non-condensable gas to a two-fluid mixture model. This approach is proposed by Mihatsch [118] for degassing effects in cavitation flows and erosion prediction. The method was partially implemented and extensively tested by T. Trummler [185].

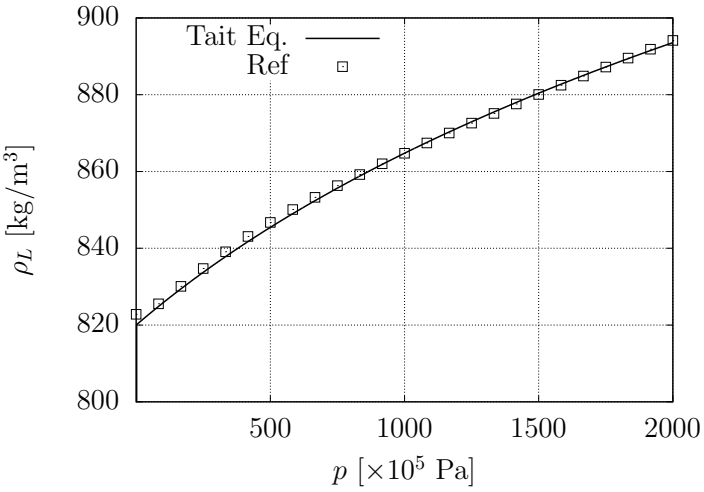

Figure 2.2: Comparison of barotropic equation of state in comparison with reference data of Dongiovanni *et al.* [37] for ISO4113 Diesel fuel.

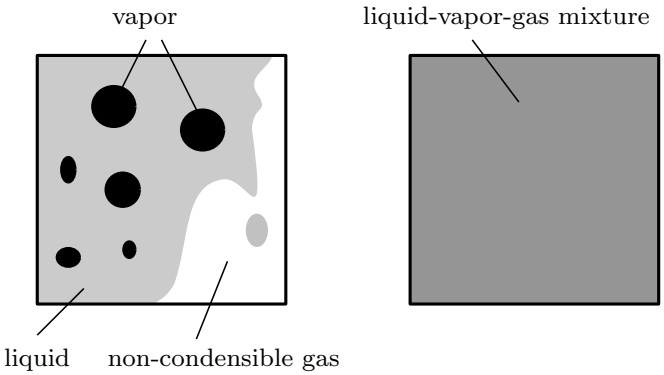

Figure 2.3: Homogenous-mixture model inside a computational cell of a finite volume discretization: resolved phase interfaces (left); numerical approximation (right).

Eulerian Two-Fluid Model

In this work, we propose a simple, closed-form barotropic two-fluid cavitation model including non-condensable gases. The thermodynamic model is an extension of the compressible framework for single-fluid implicit Large-Eddy Simulations of turbulent, cavitating flows, recently presented by Egerer *et al.* [48]. Compared to many previous approaches, such as a monolithic, Eulerian description of cavitating liquid and gas enables the analysis of nozzle and jet flows in one single simulation without domain-coupling issues or parameter calibration. Wave dynamic effects, which may propagate from the nozzle into the jet, and vice-versa, are fully represented. The framework allows to easily integrate fluid models with different properties and complexity for a broad range of applications.

In Fig. 2.3, the principle of the homogenous-mixture model inside a computational cell in the framework of a finite volume discretization is sketched. The actual interface of water in its liquid and vaporous state, that may consist of several discrete small vapor bubbles

inside one computational cell, as well as the interface between liquid (or liquid-vapor) and non-condensable gas, are not reconstructed, unlike with sharp-interface methods, e.g., Lauer *et al.* [103]. Surface tension is thus neglected. Instead, we consider the cell-averaged solution assuming negligible slip between the phases, that is, $u = u_L = u_M = u_G$, and equal pressure $p = p_L = p_M = p_G$.

The volume fraction of component $\Phi = \{L, M, G\}$ inside a control volume V is

$$\beta_\Phi = \frac{V_\Phi}{V} \quad \text{with} \quad \sum_\Phi \beta_\Phi = 1. \tag{2.29}$$

Accordingly, the mass fraction with respect to mass m is defined as

$$\xi_\Phi = \frac{m_\Phi}{m} \quad \text{with} \quad \sum_\Phi \xi_\Phi = 1. \tag{2.30}$$

The density ρ_Φ of component Φ can be written as

$$\rho_\Phi = \frac{m_\Phi}{V_\Phi} = \frac{\xi_\Phi m}{\beta_\Phi V} = \frac{\xi_\Phi}{\beta_\Phi}\rho, \tag{2.31}$$

and the averaged mixture density is

$$\rho = \frac{m}{V} = \sum_\Phi \beta_\Phi \rho_\Phi. \tag{2.32}$$

By using barotropic thermodynamic closure relations for each phase, the equation of state can be formulated in a suitable way to solve for the cell-averaged pressure $p = p(\rho)$. Hence, mixtures of non-condensable gas and pure vapor / pure liquid may occur locally, since we differentiate between purely liquid and vapor phase in water only based on the local pressure. Inter-diffusion of fluids occurs only due to turbulent mixing and numerical diffusion.

Finally, the local vapor volume fraction in the two-fluid two-phase model can be computed from

$$\alpha_v = \frac{V_{vap}}{V} = \begin{cases} 0 & , \rho \geq \rho_{sat,liq} \\ \beta_M \frac{\rho_{sat,liq} - \rho_M}{\rho_{sat,liq} - \rho_{sat,vap}} & , \rho < \rho_{sat,liq}. \end{cases} \tag{2.33}$$

Fluid viscosity in the two-fluid two-phase model is considered following Bensow and Bark [13] as

$$\mu_{mix} = \beta_{LM}[(1 - \alpha_v)\mu_{liq} + \alpha_v \mu_{vap}] + \beta_G \mu_G, \tag{2.34}$$

where the viscosities for the liquid, vapor-liquid-mixture, and gas phase are evaluated at the reference temperature $T_{ref} = 293.15$ K, respectively. The numerical values for water and ISO 4113 Diesel fluid are summarized in Tab. 2.5.

The model moreover offers a straightforward way for incorporating further extensions, such as the solution of gas into the liquid and degassing effects by adding a source term to the gas mass fraction transport equation. This may especially have an effect on cavitation

Table 2.5: Numerical values for viscosity of different phases at reference temperature $T_{ref} = 293.15K$.

Fluid	μ_{liq} [Pa s]	μ_{vap}[Pa s]	μ_G[Pa s]
Water	1.002×10^{-3}	9.727×10^{-6}	18.24×10^{-6}
ISO4113 Diesel Fluid	3.1×10^{-3}	0.1×10^{-6}	18.24×10^{-6}

collapse characteristics and, consequently, on the liquid jet when air is entrained into the nozzle.

Coupling of Multi-Fluid Model with Simplified EOS

A simple model for water jet flows injected into ambient air was developed by integrating the simplified equation of state for cavitating water flows introduced in Eq. 2.23 into the two-fluid two-phase framework. To obtain a closed form equation of state for all three phases, the individual closure relations for each phase are combined via Eq. 2.32 to

$$\rho = \beta_{LM}\left[\rho_{sat,liq} + \frac{1}{c^2}(p - p_{sat})\right] + \beta_G \frac{p}{\mathrm{R}_G T_{ref}},\ c = \begin{cases} c_L, & p \geq p_{sat} \\ c_M, & p < p_{sat} \end{cases}. \tag{2.35}$$

Following Eq. 2.29, which leads to the relation $\beta_{LM} = 1 - \beta_G$ for a two-fluid mixture, Eq. 2.35 can be written as a function of the gas mass fraction ξ_G using Eq. 2.31 as

$$\rho = \left(1 - \xi_G \frac{\rho \mathrm{R}_G T_{ref}}{p}\right)\left(\rho_{s,liq} + \frac{1}{c^2}(p - p_{sat})\right) + \xi_G \rho,\ c = \begin{cases} c_L, & p \geq p_{sat} \\ c_M, & p < p_{sat} \end{cases}. \tag{2.36}$$

The mixture pressure p is now obtained by solving the quadratic equation. The volume fraction of the liquid/liquid-vapor phase β_{LM} is computed from Eq. 2.31. In practice, we first solve for p for water in a purely liquid state, that is, the speed of sound is set to $c = c_L$. If no solution is found, we repeat this step for $c = c_M$.

Coupling of Multi-Fluid Model with Tait EOS

For the simulation of cavitating Diesel-like liquids interacting with a non-condensible gas phase we combine our two-fluid two-phase approach with our model for a Tait fluid, Eq. 2.14, and choose a set of Tait parameters $\{B, N\}$.

For a purely liquid flow, that is, $\xi_G = 0$ and $p > p_{sat}$, the Tait equation, Eq. 2.14, applies directly. Equally, for a mixture fluid without local gas component, that is, $\xi_G = 0$ and $p < p_{sat}$, we use the linear approach with a mixture speed of sound as defined in Eq. 2.27.

In the case of a local mixture of liquid/mixture and non-condensable gas component, that is, $0 < \xi_G < 1$, Eq. 2.32 can be written as

$$\rho = \beta_{L/M}\rho_{L/M} + \beta_G\rho_G \tag{2.37}$$
$$= (1-\beta_G)\rho_{L/M} + \beta_G\rho_G. \tag{2.38}$$

Combining Eqs. 2.31 and 2.9 leads to

$$\beta_G = \xi_G \frac{\rho R T_{ref}}{p}, \tag{2.39}$$

which can be used to rewrite Eq. 2.38 as

$$\rho = (1 - \xi_G \frac{\rho R T_{ref}}{p})\rho_{L/M} + \xi_G\rho. \tag{2.40}$$

For obtaining the pressure p from the above equation, we first evaluate the equation of state for a liquid-vapor-mixture, Eq. 2.28, for the fuel density $\rho_{L/M}$. This leads to the expression

$$(1 - \xi_G \frac{\rho R T_{ref}}{p})(\rho_{sat,liq} + \frac{1}{c_v^2}(p - p_{sat})) - (1-\xi_G)\rho = 0. \tag{2.41}$$

which can be solved analytically. If we find that the resulting pressure is higher than the saturation pressure of the liquid, we repeat this process using the equation of state for the liquid phase, Eq. 2.14, as

$$\left(1 - \frac{\rho\xi_G RT}{p}\right)\rho_{sat,liq}\left(\frac{p+B}{p_{sat}+B}\right)^{1/N} - (1-\xi_G)\rho = 0. \tag{2.42}$$

Figure 2.4 visualizes the functional behavior of Eq. 2.42. The non-linear equation $p = p(\rho, \xi_G)$ is solved with an iterative procedure.

We use an iterative solution procedure based on the Regula-Falsi-method, see, e.g., Dahlquist *et al.* [28], to compute the average cell pressure. The solution procedure is summarized as follows.

We define the residual

$$g(p) = \left(1 - \frac{\rho\xi_G RT}{p}\right)\rho_{sat,liq}\left(\frac{p+B}{p_{sat}+B}\right)^{1/N} - (1-\xi_G)\rho. \tag{2.43}$$

First, we determine a starting interval $[p_1, p_2]$ based on the local pressure of the previous timestep, p_{old} as shown in Algorithm 1.

Once the initial pressure interval is known, we run the Regular-Falsi method [28] to compute the updated cell pressure. The implementation used in this work is summarized in Algorithm 2.

The termination criteria are set to $g_{lim} = \varepsilon$ for the residual, where ε is a small number, and $i_{lim} = 100$ for the number of iterations. Since the functional behavior of Eq. 2.43 is well suited for iterative determination of roots usually only few iterations are necessary

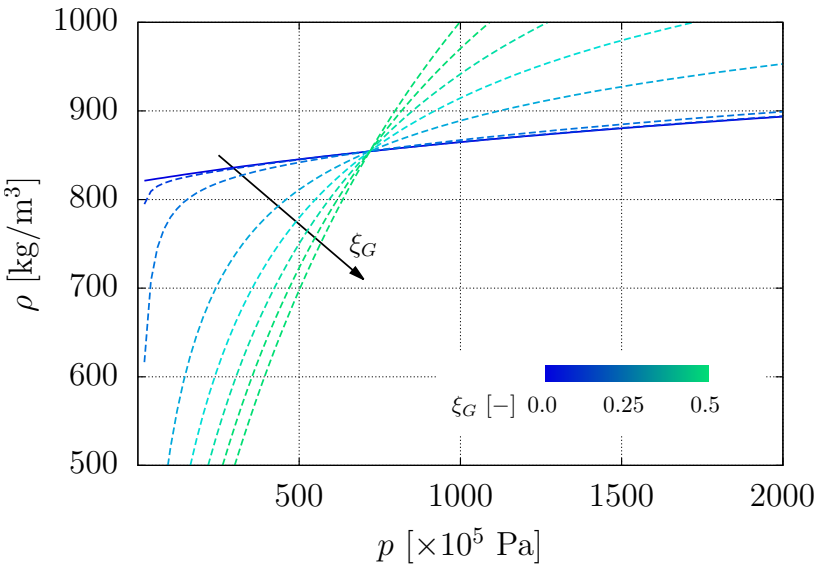

Figure 2.4: Average density over average cell pressure of the two-fluid two-phase fluid model based on the Tait equation for a range of different non-condensible gas mass fractions.

Algorithm 1 Find Start Interval $[p_1, p_2]$

$g_1 \leftarrow g(p_{old})$
$g_2 \leftarrow g(\max(p_{sat}, p_{old}/2))$
if $g_1 \cdot g_2 < 0$ **then**
  $p_1 \leftarrow p_{old}$
  $p_2 \leftarrow \max(p_{sat}, p_{old}/2)$
else if $g_1 > 0$ and $g_2 > 0$ **then**
  while $g(p_1) \cdot g(p_2) > 0$ **do**
    $p_1 \leftarrow p_2$
    $p_2 \leftarrow \max(p_{sat}, p_2/2)$
  end while
else
  while $g(p_1) \cdot g(p_2) > 0$ **do**
    $p_2 \leftarrow p_1$
    $p_1 \leftarrow 2 \cdot p_1$
  end while
end if

Algorithm 2 Determine p with Regula-Falsi-method

$g' \leftarrow g'_{init}$
$g_1 \leftarrow g(p_1)$
$g_2 \leftarrow g(p_2)$
while $|p_2 - p_1| > p_{lim}, |g'| > g_{lim}, i < i_{lim}$ **do**
  $s \leftarrow \frac{g(p_2)-g(p_1)}{p_2-p_1}$
  $p' \leftarrow p_1 - g_1/s$
  $g' \leftarrow g(p')$
  if $g_2 \cdot g' < 0$ **then**
    $p_1 \leftarrow p_2$, $p_2 \leftarrow p'$
    $g_1 \leftarrow g_2$, $g_2 \leftarrow g'$
  else
    $p_1 \leftarrow p_1$, $p_2 \leftarrow p'$
    $g_1 \leftarrow m \cdot g_1$, $g_2 \leftarrow g'$
  end if
  $i \leftarrow i + 1$
end while

to obtain a solution in the range of $p_{lim} = 1$ Pa. The adjustment factor is set to $m = 0.5$ (*Illinois algorithm* [38]).

2.3 Summary

This chapter has introduced the governing equations, i.e., the Navier-Stokes equations, which are used to model the fluid flows investigated in this work. The thermodynamic models used in this work have been discussed. Various models for closing the set of governing equations are available, which range from ideal and isothermal gas assumptions, to cavitation models based on the homogenous mixture approach. A single-fluid model, which allows to consider cavitation effects in a liquid, has been presented. The liquid and liquid-mixture phases are modelled either by a formulation of a generalized Tait equation for fluids, or a simplified linearized model based on the definition of the isentropic speed of sound. Introducing a non-condensible gas component, the cavitation model is extended to a barotropic two-fluid two-phase mixture model. The equation of state is solved either directly, where possible, or by an iterative method.

3 Numerical Method

In the following, we introduce our numerical approach. We briefly discuss the principle of implicit LES and then present the approach for cut-element based immersed boundary methods.

3.1 Mathematical Model

The computational domain Ω is divided into a fluid and solid domain, $\Omega_f(t)$ and $\Omega_s(t)$, which are separated by the interface $\Gamma(t)$ and may be time dependent. We solve the integral form of Eq. 2.1, where the integral is taken over the volume $\Omega_{i,j,k} \cap \Omega_f(t)$ of a computational cell (i, j, k) and time step $\Delta t = t^{n+1} - t^n$ as

$$\int_{t^n}^{t^{n+1}} \int_{\Omega_{i,j,k} \cap \Omega_f(t)} \left(\frac{\partial \mathbf{U}}{\partial t} + \nabla \cdot \mathbf{F}(\mathbf{U}) \right) dxdydz \; dt = 0. \tag{3.1}$$

Applying Gauss' theorem on Eq. 3.1 results in

$$\int_{t^n}^{t^{n+1}} \int_{\Omega_{i,j,k} \cap \Omega_f(t)} \frac{\partial \mathbf{U}}{\partial t} \; dV \; dt + \int_{t^n}^{t^{n+1}} \int_{\partial(\Omega_{i,j,k} \cap \Omega_f(t))} \mathbf{F}(\mathbf{U}) \cdot \mathbf{n} \; dS \; dt = 0, \tag{3.2}$$

where $\partial(\Omega_{i,j,k} \cap \Omega_f(t))$ denotes the wetted surface of a computational cell (i, j, k). The above equations are valid for a general spacial discretization. In the following, we consider

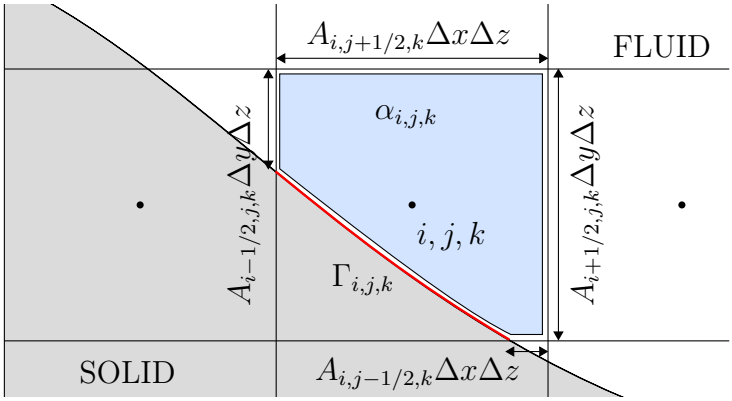

Figure 3.1: Two-dimensional sketch of a cut-cell (i, j, k).

a Cartesian mesh. Applying a volume average of the conserved variables

$$\overline{\mathbf{U}}_{i,j,k} = \frac{1}{\alpha_{i,j,k} V_{i,j,k}} \int_{\Omega_{i,j,k} \cap \Omega_f(t)} \mathbf{U} \; dxdydz, \tag{3.3}$$

where $V_{i,j,k} = \Delta x_i \Delta y_j \Delta z_k$ corresponds to the total volume of a cell $\Omega_{i,j,k}$ of a Cartesian grid, $\alpha_{i,j,k}$ corresponds to the fluid volume fraction, which becomes $0 < \alpha_{i,j,k} < 1$ in cut-cells, and $\overline{\mathbf{U}}_{i,j,k}$ is the vector of volume-averaged conserved quantities in the cut-cell, leads to

$$\begin{aligned}
\alpha^{n+1}_{i,j,k} \overline{\mathbf{U}}^{n+1}_{i,j,k} & \\
&= \alpha^{n}_{i,j,k} \overline{\mathbf{U}}^{n}_{i,j,k} \\
&+ \frac{\Delta t}{\Delta x_i} \left[A_{i-1/2,j,k} \mathbf{F}_{i-1/2,j,k} - A_{i+1/2,j,k} \mathbf{F}_{i+1/2,j,k} \right] \\
&+ \frac{\Delta t}{\Delta y_j} \left[A_{i,j-1/2,k} \mathbf{F}_{i,j-1/2,k} - A_{i,j+1/2,k} \mathbf{F}_{i,j+1/2,k} \right] \\
&+ \frac{\Delta t}{\Delta z_k} \left[A_{i,j,k-1/2} \mathbf{F}_{i,j,k-1/2} - A_{i,j,k+1/2} \mathbf{F}_{i,j,k+1/2} \right] \\
&+ \frac{\Delta t}{V_{i,j,k}} \mathbf{X}_{i,j,k}.
\end{aligned} \tag{3.4}$$

Here, $\mathbf{F}$ and A are the average numerical flux over a cell face and the effective fluid wetted cell face aperture of a cut-cell, respectively. Time-integration of the state vector is shown here for a forward Euler time integration scheme with a timestep Δt, which, e.g., corresponds to one sub-step when using a higher-order Runge-Kutta method. A sketch of a two-dimensional cut-cell is shown in Fig. 3.1. The flux $\mathbf{X}_{i,j,k}$ across the interface $\Gamma_{i,j,k} = \Gamma(t) \cap \Omega_{i,j,k}$, which is only present in cells cut by the interface, is discussed in detail below.

3.2 Turbulence Modeling

In the following, a brief introduction to the implicit LES model is presented. The discussion is based on the work of Hickel *et al.* [82], who in their studies implemented and validated the compressible version of the implicit LES scheme used in this work.

3.2.1 Introduction to Large-Eddy Simulation

For simplicity, consider a generic nonlinear one-dimensional transport equation

$$\partial_t \varphi + \partial_x F(\varphi) = 0. \tag{3.5}$$

Following Leonard [106], a convolution of Eq. 3.5 with a homogenous filter kernel G, which yields a linear low-pass filter operation

$$\bar{\varphi}(x) = \int_{-\infty}^{+\infty} G(x - x')\varphi(x')dx' = G * \varphi, \tag{3.6}$$

results in a transport equation for the filtered continuous solution $\bar{\varphi}$,

$$\partial_t \bar{\varphi} + G * \partial_x F(\varphi) = 0. \tag{3.7}$$

Subsequent projection onto a numerical grid with a constant spacing h, which yields $x_N = \{x_j\}$, leads to the discretized form of Eq. 3.7

$$\partial_t \bar{\varphi}_N + G * \partial_x F_N(\varphi_N) = -G * \partial_x \mathcal{G}_{SGS}. \tag{3.8}$$

The grid projection resembles an additional filtering operation in spectral space with cut-off at the Nyquist wavenumber $k_N = \pi/h$. Recovering the grid-projected part of the unfiltered solution, which is necessary to compute the non-linear term in Eq. 3.8, states the *soft deconvolution* problem, $\varphi_N = G^{-1} * \bar{\varphi}_N$, and is computed by an inverse-filter operation. Since wavenumbers with $k > k_N$ cannot be represented, the solution of this operation is $\varphi_N \neq \varphi$. This results in a subgrid stress tensor

$$\mathcal{G}_{SGS} = F(\varphi) - F_N(\varphi_N). \tag{3.9}$$

To find an appropriate model for $\mathcal{G}_{SGS}$ states the *hard deconvolution* problem.

Explicit LES models aim at directly modelling the subgrid stress tensor. Frequently used models include the classical approach of Smagorinsky [171], the scale similarity model of Bardina *et al.* [7], and the Dynamic Smagorinsky Model of Germano *et al.* [60]. An overview on explicit LES modelling and common approaches is provided, e.g., in Garnier *et al.* [58].

In contrast to *explicit* SGS models, *implicit* LES combines turbulence modelling and numerical discretization of the conservation equations. This approach is based on the premise that the numerical truncation error of the discretization $\mathcal{G}_N$ on grids usually used

for LES studies can outweight the modeling error, as has been shown, e.g., by Ghosal [61] and Kravchenko and Moin [99].

3.2.2 ALDM

In this work, we use an implicit LES approach based on the Adaptive Local Deconvolution (ALDM) method by Hickel *et al.* [80, 82]. ALDM is a nonlinear finite volume method and incorporates free parameters that control the truncation error. An implicit SGS model that is consistent with turbulence theory is obtained through parameter calibration, see Refs. [79, 80, 81] for details, such that the numerical error corresponds to the modeling error, i.e.

$$\mathcal{G}_N \approx -G * \partial_x \mathcal{G}_{SGS}. \tag{3.10}$$

The compressible version of ALDM [82, 83] can capture shock waves while smooth pressure waves and turbulence are propagated without excessive numerical dissipation. We also use ALDM for two-dimensional laminar test cases, where it acts as a slightly dissipative second-order centered scheme. ALDM is used to discretize the hyperbolic terms of the Navier-Stokes equations. The contribution to the flux from viscous stresses and heat conduction is discretized by a linear second-order centered scheme.

The discretization is based on a finite volume framework. This corresponds to a convolution of the unfiltered continuous solution with a top-hat-filter

$$G(\mathbf{x}, V_j) = \begin{cases} 1/V_j, & \mathbf{x} \in \Omega_j \\ 0, & \text{else.} \end{cases}, \tag{3.11}$$

where V_j corresponds to the cell volume or the grid spacing of cell Ω_j.

Cell Face Reconstruction

The values of the approximate reconstruction of the unfiltered solution, denoted with $\breve{\varphi}$, at the left (+) and right (−) cell face are computed from

$$\breve{\varphi}^{\mp}(x_{j\pm1/2}) = \sum_{k=1}^{K} \frac{1}{3} \sum_{r=0}^{k-1} \omega_{k,r}^{\mp}(\gamma_{k,r}, \bar{\varphi}_N) \breve{g}_{k,r}^{\mp}(x_{j\pm1/2}), \tag{3.12}$$

which includes a combination of Harten-type deconvolution polynomials

$$\breve{g}_{k,r}^{\mp}(x_{j\pm1/2}) = \sum_{l=0}^{k-1} c_{k,r,l}^{\mp}(x_N) \bar{\varphi}(x_{j-r+l}). \tag{3.13}$$

By choosing the grid-dependent coefficients $c_{k,r,l}^{\mp}(x_N)$ in a way that the polynomial $\breve{g}_{k,r}^{\mp}$ of degree $k-1$ provides an approximation of $\varphi(x_{j\pm\frac{1}{2}})$ on the order of k on a grid with

spacing Δx_j^k, Eq. 3.13 yields

$$\breve{g}_{k,r}^{\mp}(x_{j\pm1/2}) = \varphi(x_{j\pm1/2}) + \mathcal{O}(\Delta x_j^k). \tag{3.14}$$

The degree of the local approximation polynomials is being limited since lower orders of degree $1 \leq k \leq K = 3$ are dominant with respect to subgrid-scale modeling [82].

For $k = 1$, the dynamic weight $\omega_{k,r}^{\mp}$ in Eq. 3.12 is set to

$$\omega_{1,0}^{\mp} = 1.0. \tag{3.15}$$

Otherwise, i.e. for $1 < k \leq K$, $\omega_{k,r}^{\mp}$ is obtained from

$$\omega_{k,r}^{\mp}(\gamma_{k,r}, \bar{\varphi}_N) = \frac{\gamma_{k,r}\beta_{k,r}(\bar{\varphi}_N)}{\sum_{s=0}^{k-1}\gamma_{k,s}\beta_{k,s}(\bar{\varphi}_N)} \tag{3.16}$$

and introduces an adaptivity of the local deconvolution operator. Equation 3.16 contains free model parameters $\gamma_{k,r}$, see Tab. 3.1, and a measure for the smoothness of the solution

$$\beta_{k,r}(\bar{\varphi}_N, x_i) = \left(\varepsilon_\beta + \sum_{l=-r}^{k-r-2}\left[\bar{\varphi}(x_{i+m+1}) - \bar{\varphi}(x_{i+m})\right]^2\right)^{-2}, \tag{3.17}$$

where ε_β is a small number to avoid division by zero.

In this work, the compressible version of the simplified adaptive local deconvolution method (SALD) with one Gauss point per cell face is applied, which reduces the amount of computational operations without affecting the quality of the results, see Hickel *et al.* [78].

Numerical Flux Function

In addition to the reconstruction, the ALDM framework includes a suitable numerical flux function which acts on the advective flux and introduces a secondary regularization. A detailed discussion is provided by Hickel *et al.* [82].

The numerical flux function used in this work in a general form can be written as

$$\breve{C}_{j\pm1/2} = C\left(\varphi^*\right) - R^{\varphi}(\sigma, \breve{\varphi}^{\mp}, \bar{\varphi}) \cdot (\breve{\varphi}^{+} - \breve{\varphi}^{-}) \tag{3.18}$$

Here, the physical Navier-Stokes flux C is computed from the cell face value φ^*, which in classical ALDM [82] is defined as the arithmetic mean of both reconstructions of the unfiltered solution at the considered cell face,

$$\varphi^* = \frac{\breve{\varphi}^{+} + \breve{\varphi}^{-}}{2}. \tag{3.19}$$

The secondary regularization term R^{φ} acts on the reconstruction error $(\breve{\varphi}^{+} - \breve{\varphi}^{-})$.

Based on the definition of the advection flux in Eq. 2.2 for the i-th coordinate direction on a Cartesian grid, which can be written as

$$\mathbf{C}_i(U) = u_i \rho [1, u_1, u_2, u_3, E, \xi]^T. \tag{3.20}$$

ALDM defines the numerical density flux at an arbitrary cell face as

$$\breve{C}_i^{\rho} = \breve{u}_i^C \cdot \rho^* - R_i^{\rho} \cdot (\breve{\rho}^+ - \breve{\rho}^-) \tag{3.21}$$

with the transport velocity $\breve{u}_i^C$, which is defined below. The consistent numerical flux function for the momentum components in k-direction is

$$\breve{C}_i^{\rho u_k} = \breve{C}_i^{\rho} u_k^* - R_i^{\rho u_k} \cdot \rho^* \cdot (\breve{u}_k^+ - \breve{u}_k^-). \tag{3.22}$$

The numerical flux function for the energy equation, where applicable, is defined as

$$\breve{C}_i^{\rho e} = \breve{u}_i^C \cdot (\rho e)^* + u_k^* \left(\breve{C}_i^{\rho u_k} - \frac{u_k^*}{2} \breve{C}_i^{\rho} \right) - R_i^{\rho e} \cdot (\breve{\rho e}^+ - \breve{\rho e}^-). \tag{3.23}$$

The numerical flux for scalar quantities consistent with the ALDM scheme reads

$$\breve{C}_i^{\rho \xi} = \breve{u}_i^C \cdot (\rho \xi)^* - R_i^{\rho \xi} \cdot (\breve{\rho \xi}^+ - \breve{\rho \xi}^-). \tag{3.24}$$

The pressure flux is defined as

$$\breve{\mathbf{P}}_i = \begin{bmatrix} 0 \\ \delta_{i1} \breve{p}^* \\ \delta_{i2} \breve{p}^* \\ \delta_{i3} \breve{p}^* \\ \breve{u}_i^* \breve{p}^* \\ 0 \end{bmatrix}. \tag{3.25}$$

The interface pressure $\breve{p}^*$ hereby is computed form the arithmetic mean of the left sided and right sided interface pressure,

$$\breve{p}^* = \frac{\breve{p}^+ + \breve{p}^-}{2}. \tag{3.26}$$

The numerical transport velocity is computed following the the HLLC-Riemann-solver of Harten *et al.* [75] in a modified form [48, 84]

$$\breve{u}_i^C = u_i^* - \frac{\breve{p}^+ - \breve{p}^-}{\breve{\rho}^+ (S_R - \breve{u}_i^+) - \breve{\rho}^- (S_L - \breve{u}_i^-)}, \tag{3.27}$$

where

$$S_R = \max(\breve{u}_i^+, \breve{u}_i^-) + c \tag{3.28}$$

and

$$S_L = \min(\breve{u}_i^+, \breve{u}_i^-) - c \tag{3.29}$$

Table 3.1: Model parameters for ALDM reconstruction and flux computation

Parameter	Value
$\gamma^+_{2,0}$=$\gamma^-_{2,1}$	1
$\gamma^+_{2,1}$=$\gamma^-_{2,0}$	0
$\gamma^+_{3,0}$=$\gamma^-_{3,2}$	0.01902
$\gamma^+_{3,1}$=$\gamma^-_{3,1}$	0.08550
$\gamma^+_{3,2}$=$\gamma^-_{3,0}$	1-$\gamma^+_{3,0}$-$\gamma^+_{3,1}$
σ^ρ	0.615
$\sigma^{\rho u}$	0.125
$\sigma^{\rho e}$	0.615
$\sigma^{\rho\xi}$	0.615

denote estimates of the fastest right and left running wave speeds with the speed of sound c.

The dissipation matrix adding to the density, momentum, and energy flux finally is defined as

$$\mathbf{R}_i = \begin{bmatrix} R_i^\rho \\ R_i^{\rho u_1} \\ R_i^{\rho u_2} \\ R_i^{\rho u_3} \\ R_i^{\rho e} \\ R_i^{\rho\xi} \end{bmatrix} = \begin{bmatrix} \sigma^\rho |\breve{u}_i^+ - \breve{u}_i^-| \\ \sigma^{\rho u} |\breve{u}_1^+ - \breve{u}_1^-| \\ \sigma^{\rho u} |\breve{u}_2^+ - \breve{u}_2^-| \\ \sigma^{\rho u} |\breve{u}_3^+ - \breve{u}_3^-| \\ \sigma^{\rho e} |\breve{u}_i^+ - \breve{u}_i^-| \\ \sigma^{\rho\xi} |\breve{u}_i^+ - \breve{u}_i^-| \end{bmatrix} + f_s \frac{|\breve{u}_i^C| + |\breve{u}_i^+ - \breve{u}_i^-|}{2} \begin{bmatrix} 1 \\ 1 \\ 1 \\ 1 \\ 1 \\ 1 \end{bmatrix} \tag{3.30}$$

The values of σ^ρ,$\sigma^{\rho u}$, $\sigma^{\rho e}$, and $\sigma^{\rho\xi}$ are free model parameters, see Tab. 3.1. For a detailed discussion on the calibration process refer to Hickel *et al.* [82].

Since collapse events of vapor structures involve strong shock waves, a second term is added to the dissipation matrix that contains a sensor functional of Ducros *et al.* [39] to capture propagating discontinuities

$$f_s = \begin{cases} 1, & \frac{|\nabla\cdot\bar{\mathbf{u}}|}{|\nabla\cdot\bar{\mathbf{u}}|+||\nabla\times\bar{\mathbf{u}}||+\varepsilon_s} \geq 0.95 \\ 0, & \text{else} \end{cases}, \tag{3.31}$$

where $\varepsilon_s = 10^{-15}$. This modification adds numerical dissipation, which enhances the stability of the scheme.

Reconstruction and Flux Function for Density and Scalars

Due to large density gradients between water, water vapor, and gas, we modify the reconstruction of the cell face density ρ^* and scalar gas mass fraction ξ^* to enhance numerical stability. The right- and left-sided cell face values of a quantity φ hereby are not computed from Eqn. 3.12, but from a first order ($\dot{\varphi}$) or a second order reconstruction using an Van-Albada limiter function ($\ddot{\varphi}$) [190]. The first order method was implemented and

validated by Egerer *et al.* [48]. The second order method was investigated in great detail by Trummler [185] for the Van-Albada limiter as well as other reconstruction schemes. We choose between first and second order reconstruction in the applications discussed throughout this thesis based on the desired accuracy.

The reconstruction for the first order scheme yields

$$\dot{\varphi}^- = \bar{\varphi}_{j-1}, \tag{3.32}$$

$$\dot{\varphi}^+ = \bar{\varphi}_j. \tag{3.33}$$

Using a second order Van-Albada reconstruction we, compute

$$\ddot{\varphi}^- = \bar{\varphi}_{j-1} + \frac{\bar{\varphi}_j - \bar{\varphi}_{j-2}}{2} \cdot \frac{\max[(\bar{\varphi}_{j-1} - \bar{\varphi}_{j-2})(\bar{\varphi}_j - \bar{\varphi}_{j-1}), 0]}{(\bar{\varphi}_{j-1} - \bar{\varphi}_{j-2})^2 + (\bar{\varphi}_j - \bar{\varphi}_{j-1})^2 + \varepsilon}, \tag{3.34}$$

$$\ddot{\varphi}^+ = \bar{\varphi}_j - \frac{\bar{\varphi}_{j+1} - \bar{\varphi}_{j-1}}{2} \cdot \frac{\max[(\bar{\varphi}_j - \bar{\varphi}_{j-1})(\bar{\varphi}_{j+1} - \bar{\varphi}_j), 0]}{(\bar{\varphi}_j - \bar{\varphi}_{j-1})^2 + (\bar{\varphi}_{j+1} - \bar{\varphi}_j)^2 + \varepsilon}, \tag{3.35}$$

where ε is a small number to avoid a division by zero.

The cell face value (for density and scalar quantities) is subsequently obtained from

$$\varphi^* = \frac{1}{2}\left[(1 + \mathrm{sgn}(\breve{u}_i^C))\hat{\varphi}^- + (1 - \mathrm{sgn}(\breve{u}_i^C))\hat{\varphi}^+\right], \tag{3.36}$$

where $\hat{\varphi}^- = \{\dot{\varphi}^-, \ddot{\varphi}^-\}$ and $\hat{\varphi}^+ = \{\dot{\varphi}^+, \ddot{\varphi}^+\}$ denote the right- and left-sided cell face values for first and second order reconstruction, respectively, and $\breve{u}_i^C$ is the ALDM transport velocity, Eqn. 3.27.

For the second order upwind scheme, the density flux introduced in Eq. 3.24 is modified to

$$\breve{C}_i^\rho = \breve{u}_i^C \cdot \rho^* - \sigma^\rho |\breve{u}_i^+ - \breve{u}_i^-| \cdot (\ddot{\rho}^+ - \ddot{\rho}^-), \tag{3.37}$$

omitting any contribution of the shock sensor, since the reconstruction itself introduces a sufficient amount of dissipation.

The scalar transport in spatial direction i for both first and second order cell face reconstruction is computed from a reconstruction of the primitive variables

$$\breve{C}_i^{\rho\xi} = \breve{u}_i^C \rho^* \xi^*, \tag{3.38}$$

without further regularization. Hereby the gas mass fraction at the cell face ξ^* is reconstructed with the same scheme as the interface density as introduced in Eq. 3.36.

3.3 Conservative Immersed Boundary Method

In previous publications, the immersed boundary method for representing complex immersed solid obstacles or phase interfaces on Cartesian grids has been analysed either for incompressible fluids or for compressible gas-like fluids. In this work, we present a

conservative cut-cell method for compressible viscous LES of weakly compressible liquid fluid flows with cavitation effects through moving geometries. In stiff fluids, such as water or liquid fuels, an exact representation of the geometry (fluid volume fraction and face apertures in the cut-cells) is crucial as small errors in these quantities induce large artificial pressure oscillations in the vicinity of sharp corners. We will show that level-set based approaches [70, 114, 115, 116] fail to deliver the required accuracy. We propose to directly reconstruct the geometrical parameters from the cell intersection with a triangulated interface geometry of the immersed boundary rather than from a level-set field. The method provides sub-cell resolution of the geometry and handles flows through narrow closing or opening gaps in a straightforward manner. Since this cut-element method provides a sharp and accurate geometry representation, it is suitable for simulating the flow around obstacles with prescribed motion, as shown in this work, and moreover introduces a framework for fluid-structure interaction (FSI) problems, i.e., the interaction of fluid flow and deformable solid structures.

This section has partially been published in Örley et al. [132].

3.3.1 Geometry Computation

With previous approaches [70, 114, 115, 116] the geometric properties of the cut-cell (fluid face apertures A, the interface normal vector $\mathbf{n}$, and the fluid volume fraction $\alpha_{i,j,k}$) were obtained from a level-set field Φ, which represents a signed distance of a point in the domain to the immersed boundary. The value of the level-set field in a computational cell $\Phi_{i,j,k}$ around the interface is computed based on a search algorithm that finds the minimum distance to the next interface or by solving a diffusion equation. The level-set values are subsequently interpolated onto the cell corners and geometric quantities are computed assuming a linear variation. As a result, a piecewise linear approximation of the interface $\Gamma(t)$ is obtained, as shown in Fig. 3.2 (a). This method has been successfully applied for simple stationary boundaries, see [70, 84, 114, 115, 116]. When dealing with moving boundaries featuring sharp corners and complex geometries in liquid water flows, on the other hand, numerical artifacts can develop, which are particularly problematic for liquid-vapor phase transitions and can lead to unphysical local cavitation regions.

As an example, we consider the translation of a piston with rounded edges at a constant velocity $v_{geo} = -1\ m/s$ in water, see Fig. 3.3(a). The rounded edge is well resolved by the interface triangulation (orange line). The isoline for $\Phi = 0$ reconstructed by the level-set method is shown as a blue line. A significant smoothening of the corner compared to the original geometry is observed. As soon as the piston moves into neighboring cells, spurious pressure and density oscillations are generated with the level-set method, see Fig. 3.3(b), which result in strong, unphysical compressions and expansions in the monitor cells, see Fig. 3.4(a), where the density ρ of the five monitor cells defined in Fig. 3.3(a) is plotted over time.

The origin of this phenomenon is as a discontinuity in the fluid volume fraction of the cut-cells, as shown in Fig. 3.4(b). At $t \sim 0.03\ s$, a jump in the fluid volume fraction is detected in monitor cells 3, 4 and 5. With the mass being exactly conserved in the

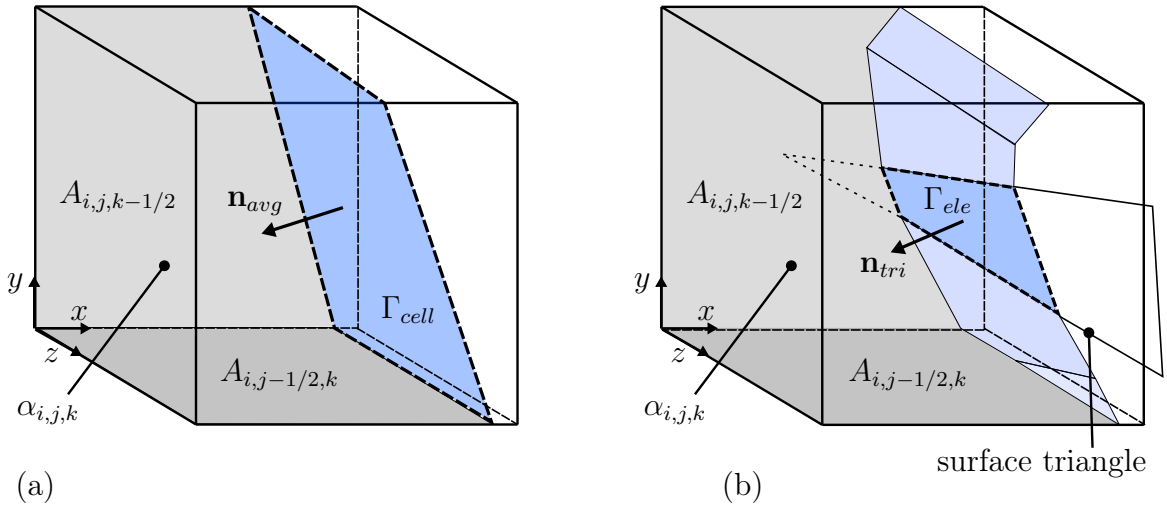

Figure 3.2: Computation of geometrical cut-cell properties based on a level-set field Φ (a) and on exact intersection with a provided surface triangulation (b).

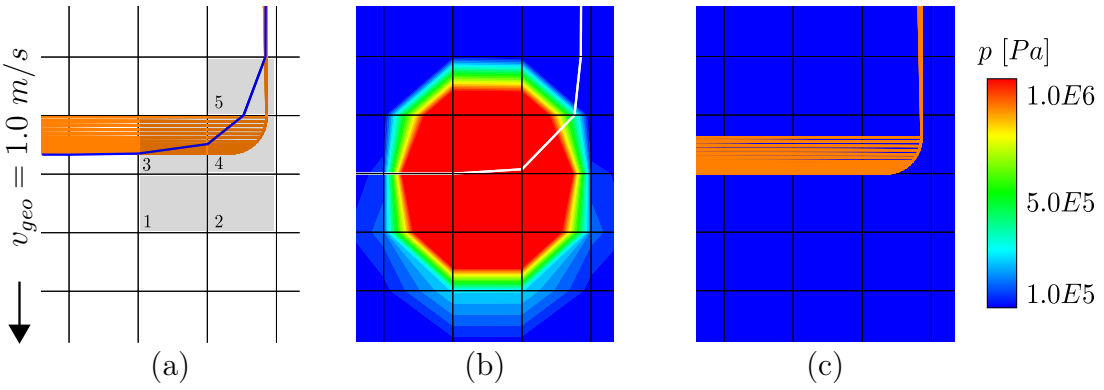

Figure 3.3: Motion of complex geometries (a); Level-set method: strong pressure oscillations occur when geometry moves into neighboring computational cell due to jump in fluid volume fraction (b); Cut-element method: oscillation-free pressure field with accurate geometry computation (c). Orange line: surface triangles. Blue/white line: wall location computed from level-set Φ.

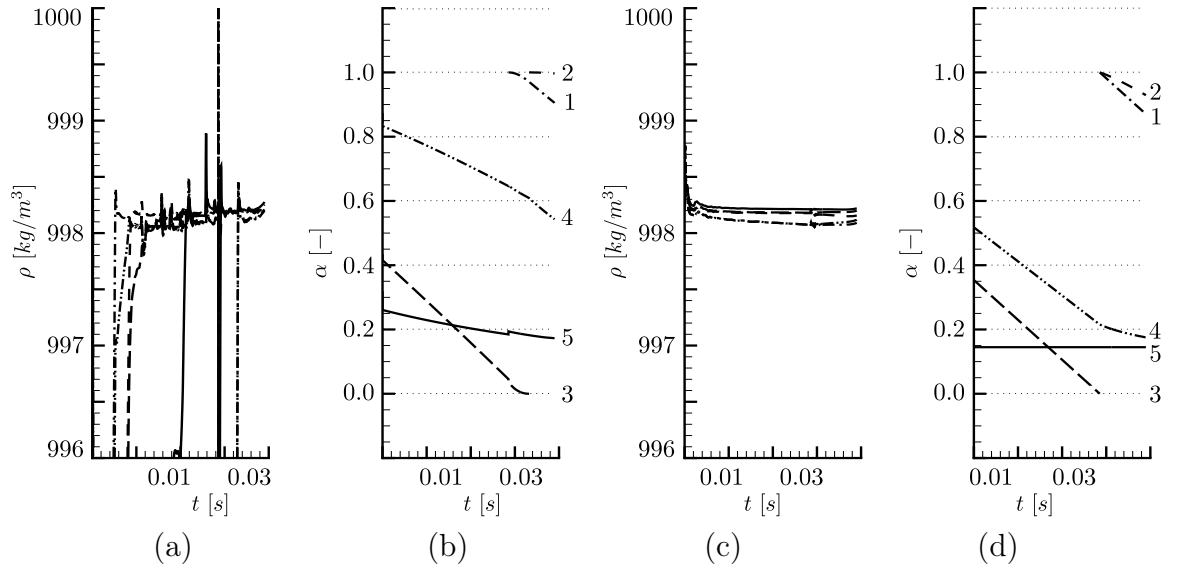

Figure 3.4: Density and fluid volume fraction α over simulation time t in monitored cells $1-5$ (see Fig. 3.3): -·-· monitor cell 1, - - - monitor cell 2, — — monitor cell 3 —·—·· monitor cell 4, — monitor cell 5; level-set based method (a), (b), and surface triangulation-based method (c), (d).

computational cell, this discontinuity in the density causes a very high pressure peak due to the low compressibility of liquid water. A phenomenon of this kind is observed for stiff equations of state, Eq. 2.14, and is much less pronounced for more compressible fluids such as air. Such small discontinuities of the volume fraction occur independently of the way the level-set field is computed. They result from truncation errors inherent to the grid based level-set representation once the geometry exhibits radii that are of the same order as the cell size. In particular, they are inevitable when the geometry has sharp corners.

A solution for this issue is to use a more accurate reconstruction of the geometrical parameters. We resort to the exact representation of the geometry based on the computational mesh and the provided surface triangulation, as shown in Fig. 3.2(b). While the level-set method leads to an averaged interface Γ_{cell} as an approximation of the geometry, the cut-element method represents the interface as a number of cut-elements Γ_{ele}. Each cut-cell contains and updates its respective individual set of cut-elements, which is also used to compute the interface exchange term $\mathbf{X}_{i,j,k}$ for each cut-cell as described below. The computation of the exact geometry is done by a sub-triangulation of the cell faces and a sub-tetrahedralization of the fluid volume.

Fig. 3.5 shows the main steps of this procedure for a single cut-element, which is computed from a surface triangle defined by its corner points $c = \{c_1, c_2, c_3\}$, its edges $e = \{e_1, e_2, e_3\}$ and the triangle normal vector $\mathbf{n}_{tri}$. First, we generate a set of corner vertices $\mathcal{V} = \{\mathcal{V}_1, \mathcal{V}_2, \mathcal{V}_3, ...\}$ for each cut-element contained in a computational cell (i, j, k), see Fig. 3.5(a). The set consists of three subsets, which are

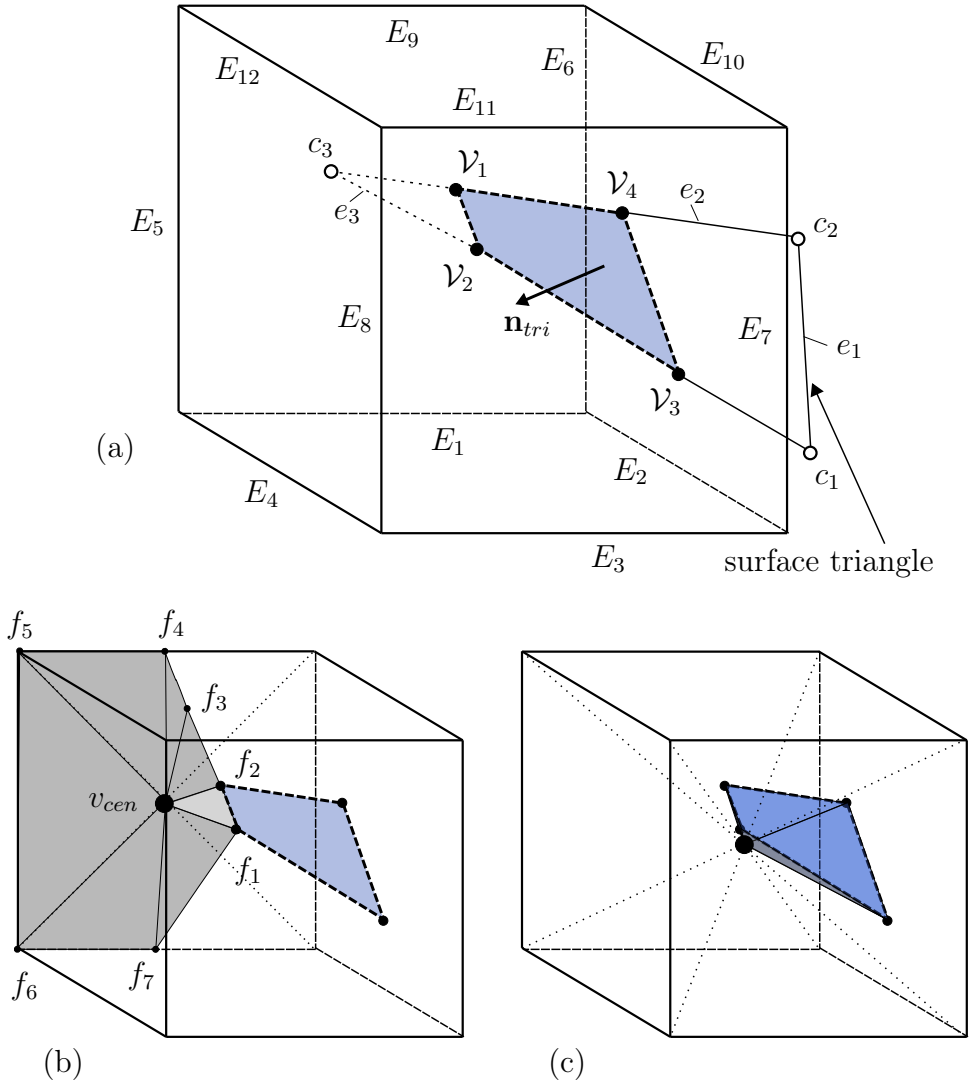

Figure 3.5: Algorithm for computation of geometry parameters based on cut-elements. Construction of set of element corner vertices $\mathcal{V}$ (top) and computation of wetted cell face area and fluid volume (bottom).

(1) surface triangle corner points c lying inside the computational cell

$$v_I = c \cap \Omega_{i,j,k}, \tag{3.39}$$

(2) intersection points of triangle edges e with the cell faces

$$v_{II} = e \cap \partial\Omega_{i,j,k}, \tag{3.40}$$

and

(3) intersection points of cell edges $E = \{E_1, E_2, ..., E_{12}\}$ with the triangle face Γ_Δ

$$v_{III} = E \cap \Gamma_\Delta. \tag{3.41}$$

Subsets v_I, v_{II} or v_{III} may be empty, depending on the position of the triangle with respect to the computational cell. In the example sketched in Fig. 3.5(a) only intersections of triangle edges with the front- and backside cell faces are found.

Subsequently, the full vertex list bounding the cut-element

$$\mathcal{V} = v_I \cup v_{II} \cup v_{III} \tag{3.42}$$

is sorted in a right-hand-system using the triangle normal. Double entries, which can occur when a triangle and cell edge intersect, are merged. This procedure is repeated until all surface triangles that intersect with the respective computational cell are captured.

To compute the wetted area A_w for a cell face, we extract a subset $f = \{f_1, f_2, ..., f_n\}$ of n points from set $\mathcal{V}$, containing all elements that belong to the cell face, and add all cell corners of this face that lie inside the fluid domain. After sorting the list using the cell-face normal vector, a triangulation is constructed by spanning triangles of two adjacent vertices of f and the cell-face centroid, v_{cen} (see, e.g., Fig. 3.5(b), where the wetted area of the backside cell face is defined by 7 points). The total wetted face area is obtained from

$$A_w = \Delta(f_n, f_1, v_{cen}) + \sum_{i=1}^{n-1} \left[\Delta(f_i, f_{i+1}, v_{cen})\right], \tag{3.43}$$

where $\Delta(\bullet, \bullet, \bullet)$ denotes the area magnitude of the triangle spanned by three points. In the same way, the area of a cut-element is computed as the sum of the triangle areas formed by two vertices of set $\mathcal{V}$ and the cut-element centroid. The fluid volume of the cell is computed as the sum of all polyhedra spanned by the area of all cut-elements and the cell centroid, see Fig. 3.5(c), and of all polyhedra spanned by the wetted face areas and the cell centroid.

Applying this technique to the aforementioned test case of a moving piston with a rounded edge results in a fluid volume fraction that is continuous in time, as shown in Fig. 3.4(d), and hence the pressure and density fields do not show spurious oscillations, see Figs. 3.3(c) and 3.4(c).

Table 3.2: Additional computational effort for moving geometry

Case	Grid	Computational overhead
In-line oscillating cylinder in a fluid at rest	coarse	16%
	medium	22%
	fine	19%
Flow past an in-line oscillating cylinder at $Re = 100$	coarse	4%
	fine	4%
Cavitating control valve		$\sim 50\%$
Nine-hole Diesel injector	coarse	$\sim 35\%$
	medium	$\sim 40\%$
	fine	$\sim 35\%$

For the simulations involving moving geometries, such as those discussed below, the necessary geometry parameters have to be updated in each time-step. The computational overhead for geometry reconstruction for the examples presented in this paper compared with an identical, but stationary geometry, is summarized in Tab. 3.2. The overhead depends on surface triangulation, grid resolution, and the number of cut-cells and thus is strongly case dependent. Furthermore we found that an optimization of the parallel code implementation in the control valve case may significantly enhance the computational efficiency and is thus subject to current investigations.

3.3.2 Treatment of Gaps

With the cut-element method outlined above it is possible to represent more than one solid boundary within one cell, see Fig. 3.6. To account for this fact we compute a net face aperture of cell faces cut by multiple boundaries. The fluid volume fraction is treated accordingly. The computation of the effective cell face aperture for n solid boundaries inside the computational cell can be written as

$$A_{eff,i,j,k} = 1 - \left[\sum_n (1 - A_{n,i,j,k}) \right] \tag{3.44}$$

and the fluid volume fraction

$$\alpha_{eff,i,j,k} = 1 - \left[\sum_n (1 - \alpha_{n,i,j,k}) \right]. \tag{3.45}$$

Note that Eqs. 3.44 and 3.45 are based on the (physical) requirement that solid obstacles do not overlap.

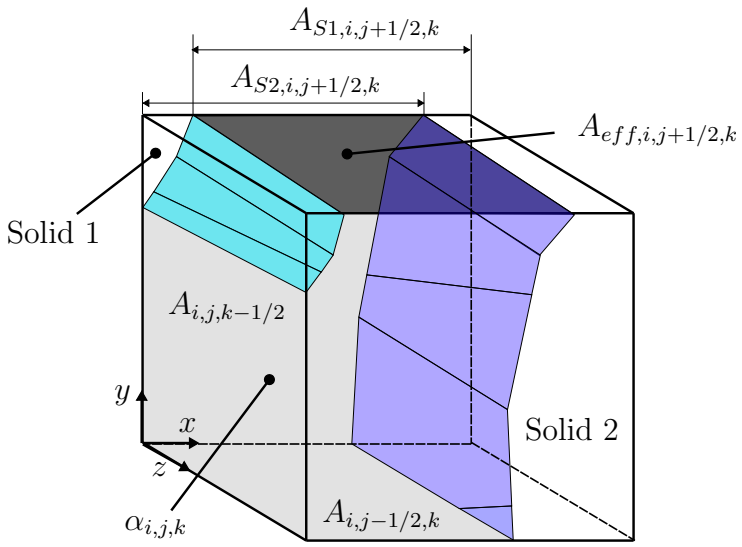

Figure 3.6: Cut-cell with multiple solid bodies. Effective face aperture $A_{eff,i,j+1/2,k}$ is computed from individual contributions from each of the two solid bodies $A_{S1,i,j+1/2,k}$ and $A_{S2,i,j+1/2,k}$.

3.3.3 Interface Exchange Term

Interaction of the fluid with a solid interface is modelled by an interface exchange term $\mathbf{X}_{i,j,k}$, as introduced in Eq. 3.4. Following the geometrical approach introduced above, we can write the interface exchange term as a sum of all individual contributions of all cut-elements contained within this computational cell in a consistent way as

$$\mathbf{X}_{i,j,k} = \sum_{ele} \mathbf{X}_{ele}. \tag{3.46}$$

The element based interface exchange term $\mathbf{X}_{ele}$ includes the source terms for pressure, viscous effects and heat transfer at the element interface

$$\mathbf{X}_{ele} = \mathbf{X}^{p}_{ele} + \mathbf{X}^{\nu}_{ele} + \mathbf{X}^{ht}_{ele}. \tag{3.47}$$

The pressure term is

$$\mathbf{X}^{p}_{ele} = \begin{bmatrix} 0 \\ p_{\Gamma,ele}\Delta\Gamma_{ele}\ n_1^{\Gamma,ele} \\ p_{\Gamma,ele}\Delta\Gamma_{ele}\ n_2^{\Gamma,ele} \\ p_{\Gamma,ele}\Delta\Gamma_{ele}\ n_3^{\Gamma,ele} \\ p_{\Gamma,ele}\Delta\Gamma_{ele}\ \left(\mathbf{n}^{\Gamma,ele}\cdot\mathbf{v}^{\Gamma,ele}\right) \end{bmatrix}, \tag{3.48}$$

where $\Delta\Gamma_{ele}$ is the element surface area, $\mathbf{n}^{\Gamma,ele} = [n_1^{\Gamma,ele}, n_2^{\Gamma,ele}, n_3^{\Gamma,ele}]$ is the element normal vector obtained directly from the surface triangle, and $\mathbf{v}^{\Gamma,ele}$ is the interface velocity. The element interface pressure $p_{\Gamma,ele}$ is obtained by solving a one-sided face-normal Riemann problem with a suitable approximate or exact Riemann solver.

The viscous stress at the boundary is modelled by

$$\mathbf{X}_{ele}^{\nu} = \begin{bmatrix} 0 \\ D_1 \\ D_2 \\ D_3 \\ C \end{bmatrix}, \tag{3.49}$$

where the contribution to the momentum equation is

$$\mathbf{D} = \int_{\Gamma_{ele}} \overline{\tau} \cdot \mathbf{n}^{\Gamma,ele} dS \tag{3.50}$$

and the contribution to the energy equation is

$$C = \int_{\Gamma_{ele}} (\overline{\tau} \cdot \mathbf{v}^{\Gamma,ele}) \cdot \mathbf{n}^{\Gamma,ele} dS. \tag{3.51}$$

$\overline{\tau}$ denotes the local viscous stress tensor, which we approximate as in [115].

In case of an isothermal interface, the heat transfer across the fluid-solid-boundary

$$q = \int_{\Gamma_{ele}} k \nabla T \cdot \mathbf{n}^{\Gamma,ele} dS, \tag{3.52}$$

needs to be taken into account within the flux balance of the cut-cell by the heat transfer term

$$\mathbf{X}_{ele}^{ht} = \begin{bmatrix} 0 \\ 0 \\ 0 \\ 0 \\ q \end{bmatrix}. \tag{3.53}$$

3.3.4 Ghost-Cell Boundary Conditions for Solid Walls

Cells in the solid part of the computational domain near the interface, so-called ghost-cells, contain ghost states that allow boundary conditions at the interface to be satisfied without requiring a modification of interpolation stencils in the finite-volume reconstruction scheme. For this purpose, we apply the ghost-cell methodology as originally proposed by Mittal et *al.* [123] and further extended to stationary and moving boundary cut-cell methods by Pasquariello et *al.* [138]. Finding the ghost-points and extending the solution into the solid region does not require the fully detailed cut-cell geometry. We therefore perform this procedure based on the average face centroid and normal vector of the cut-cell, which is an average of all contained cut-elements weighted by their area. In a first step, ghost-cells $\mathbf{x}_{GP}$ that contribute to the interpolation stencil of the baseline discretization are identified, see Fig. 3.7. Next, for each ghost-cell the boundary intercept point $\mathbf{x}_{BI}$ is computed such that the line segment $\overline{\mathbf{x}_{GP}\mathbf{x}_{BI}}$ intersects the immersed boundary in

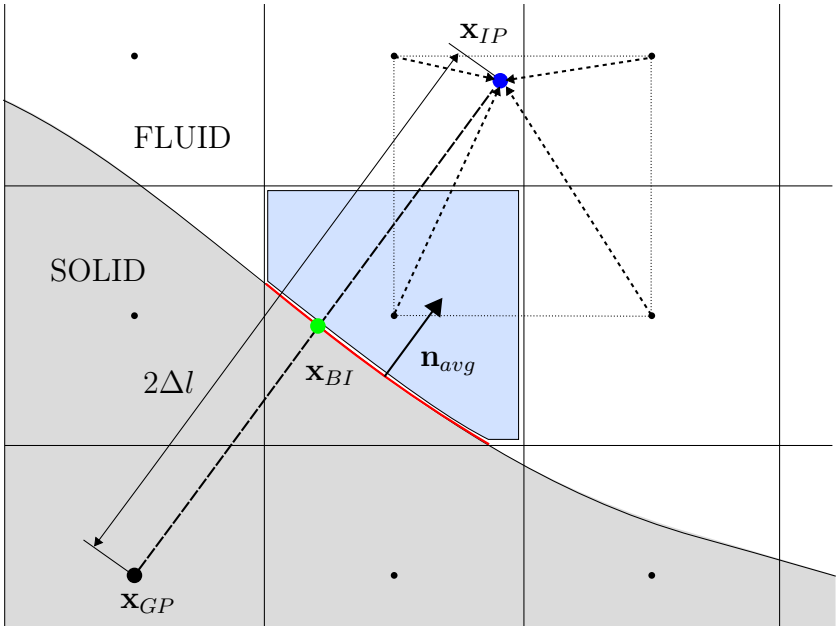

Figure 3.7: Construction of the ghost-cell extending procedure for a cut-cell (i, j, k).

$\mathbf{x}_{BI}$ normal to the interface segment. The line segment is extended into the fluid region to find the image point

$$\mathbf{x}_{IP} = \mathbf{x}_{BI} + \mathbf{n}^{\Gamma,avg} \cdot \Delta l, \tag{3.54}$$

where $\Delta l = ||\mathbf{x}_{BI} - \mathbf{x}_{GP}||$ denotes the distance between the ghost-cell and the boundary intercept. Once the image point has been identified, a bilinear (2-D) or trilinear (3-D) interpolation is used to calculate the value of a quantity ϕ_{IP} at the image point x_{IP}. Ghost-cell values are obtained using a linear approximation along the line $\overline{\mathbf{x}_{GP}\mathbf{x}_{BI}}$ that implicitly satisfies the boundary conditions at the boundary intercept location $\mathbf{x}_{BI}$. For Dirichlet boundary conditions, ghost-cell data are obtained as

$$\phi_{GP} = 2 \cdot \phi_{BI} - \phi_{IP} + \mathcal{O}(\Delta l^2), \tag{3.55}$$

whereas Neumann boundary conditions are imposed as

$$\phi_{GP} = \phi_{IP} - 2 \cdot \Delta l \left.\frac{\partial \phi}{\partial n}\right|_{\mathbf{x}_{BI}} + \mathcal{O}(\Delta l^2). \tag{3.56}$$

3.3.5 Treatment of Small Cut-Cells

The time step Δt is adjusted according to the CFL condition for the underlying Cartesian grid. To achieve a stable time integration also for small cut-cells without severe time step restriction, we adopt the conservative mixing procedure from Meyer et *al.* [115]. The conserved quantities in small cut-cells are mixed with larger neighboring cells in a conservative way, see Fig. 3.8 , where the exchange rate of mass, momentum and energy

between two cells is controlled by weights β defined as

$$\begin{aligned}
\beta^{x}_{i,j,k} =& |n_1^{\Gamma,avg}|^2 \ \alpha_{mix_i,j,k} \\
\beta^{y}_{i,j,k} =& |n_2^{\Gamma,avg}|^2 \ \alpha_{i,mix_j,k} \\
\beta^{z}_{i,j,k} =& |n_3^{\Gamma,avg}|^2 \ \alpha_{i,j,mix_k} \\
\beta^{xy}_{i,j,k} =& |n_1^{\Gamma,avg} n_2^{\Gamma,avg}| \ \alpha_{mix_i,mix_j,k} \\
\beta^{xz}_{i,j,k} =& |n_1^{\Gamma,avg} n_3^{\Gamma,avg}| \ \alpha_{mix_i,j,mix_k} \\
\beta^{yz}_{i,j,k} =& |n_2^{\Gamma,avg} n_3^{\Gamma,avg}| \ \alpha_{i,mix_j,mix_k} \\
\beta^{xyz}_{i,j,k} =& |n_1^{\Gamma,avg} n_2^{\Gamma,avg} n_3^{\Gamma,avg}|^{2/3} \ \alpha_{mix_i,mix_j,mix_k}.
\end{aligned} \tag{3.57}$$

The weights are normalized in such a way that

$$\beta^{x}_{i,j,k} + \beta^{y}_{i,j,k} + \beta^{z}_{i,j,k} + \beta^{xy}_{i,j,k} + \beta^{xz}_{i,j,k} + \beta^{yz}_{i,j,k} + \beta^{xyz}_{i,j,k} = 1. \tag{3.58}$$

The mixing flux $\mathbf{M}^{trg}_{i,j,k}$ from a cut-cell (i,j,k) to a suitable target cell trg is subsequently computed from

$$\mathbf{M}^{trg}_{i,j,k} = \xi(\alpha_{i,j,k}) \cdot \frac{\beta^{trg}_{i,j,k}[(V_{trg}\alpha_{trg}\overline{\mathbf{U}}^{*}_{trg})V_{i,j,k}\alpha_{i,j,k} - (V_{i,j,k}\alpha_{i,j,k}\overline{\mathbf{U}}^{*}_{i,j,k})V_{trg}\alpha_{trg}]}{V_{i,j,k}\alpha_{i,j,k}\beta^{trg}_{i,j,k} + V_{trg}\alpha_{trg}} \tag{3.59}$$

where $\overline{\mathbf{U}}^{*}_{i,j,k}$ and $\overline{\mathbf{U}}^{*}_{trg}$ are the vectors of conserved quantities in the cut and target cell before mixing.

The parameter $\xi(\alpha_{i,j,k})$ is introduced to achieve a smooth blending between full mixing in cut-cells with a fluid volume fraction smaller than a threshold value α_{th}, and no mixing in large cut-cells. This step is important when dealing with moving boundaries, where a blending factor of the form

$$\xi(\alpha_{i,j,k}) = \begin{cases} 0 & , \alpha_{i,j,k} \geq \alpha_{th} \\ 1 & , \text{else,} \end{cases}, \tag{3.60}$$

with a threshold $\alpha_{th} < 1$ would generate a discontinuity in the flux redistribution and can generate pressure artifacts [164]. We choose a simple linear blending factor defined as

$$\xi(\alpha_{i,j,k}) = \begin{cases} 0 & , \alpha_{i,j,k} = 1 \\ \frac{1-\alpha_{i,j,k}}{1-\alpha_{th}} & , 1 > \alpha_{i,j,k} > \alpha_{th} \\ 1 & , \text{else,} \end{cases}, \tag{3.61}$$

where α_{th} is set to 0.6 in all simulations presented in this paper. We also evaluated other continuous functionals $\xi(\alpha_{i,j,k})$, and found that the particular choice of ξ had little effect on the results.

After advancing the solution in time, the volume averaged conserved variables of cut and

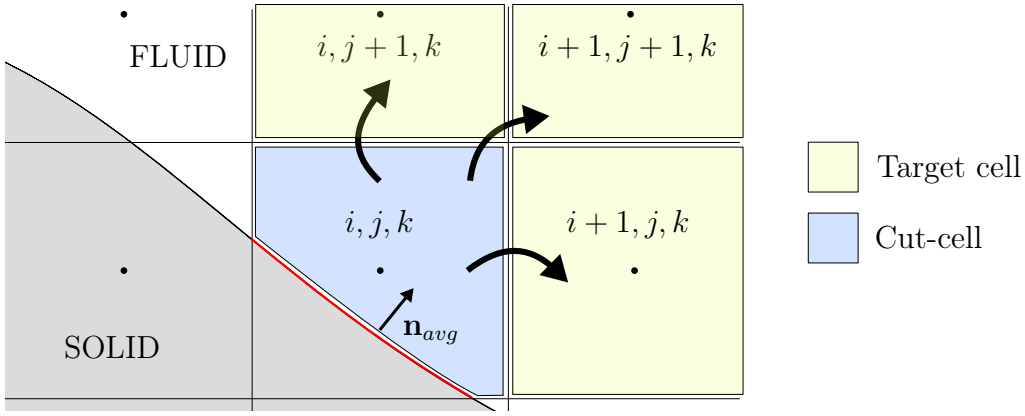

Figure 3.8: Conservative mixing procedure of a small cut-cell (i, j, k).

target cells are updated with

$$\overline{\mathbf{U}}_{i,j,k} = \overline{\mathbf{U}}^*_{i,j,k} + \frac{\mathbf{M}^{trg}_{i,j,k}}{\alpha_{i,j,k} V_{i,j,k}} \tag{3.62}$$

and

$$\overline{\mathbf{U}}_{trg} = \overline{\mathbf{U}}^*_{trg} - \frac{\mathbf{M}^{trg}_{i,j,k}}{\alpha_{trg} V_{trg}}, \tag{3.63}$$

3.4 Time Integration

For time integration, the conditionally stable explicit third-order Runge-Kutta method of Gottlieb and Shu [65] is used. This time-discretization scheme is strongly stable for CFL ≤ 1. The time-step Δt in all problems presented here is limited by the propagation speed of acoustic waves and is computed from

$$\Delta t = \mathrm{CFL} \cdot \frac{1}{\frac{|u|+c}{\Delta x} + \frac{|v|+c}{\Delta y} + \frac{|w|+c}{\Delta z}} \tag{3.64}$$

with u, v, w being the velocity components and c the speed of sound, respectively. For liquid flows, the speed of sound becomes $c = c_{liq}$, which is approximately 1500 m/s for the pressure range used in this study, and hence the time-step Δt is reduced to the order of 10^{-10}s. This time step size is also needed for resolving wave dynamics which dominate flow evoluion at such small scales.

3.5 Code Implementation

For our simulations we use the finite-volume Cartesian multi block flow solver *INCA*. The code is developed at the Institute of Aerodynamics and Fluid Mechanics at the Technische

Universität München. It is used in various fields of research, including shock boundary layer interaction [69, 71, 136], multi-fluid problems [103, 104], aircraft airodynamics [114, 117, 200], supersonic combustion chambers [45, 46, 47], shock induced turbulent mixing in Richtmyer-Meshkov instabilities [180, 181, 182, 183, 184], and shock induced combustion processes [34].

The program sequence is sketched in Algorithm 3. The algorithm includes the main steps related to the treatment of immersed boundaries. *INCA* is written in Fortran and uses MPI and OpenMP libraries for massively parallalelized simulations on supercomputers. For moving-boundary problems, we have extended the partitioning mechanism to account for the number of moving- and non-moving cut-cells on a block, which add additional weight to the grid block in a preprocessing step.

To minimize computational costs, *INCA* is equipped with local grid refinement capabilities at block interfaces based on hanging nodes. In this work, the refinement level is limited to a maximum of 2, i.e., the cell number with respect to a finer / coarser block is at most doubled / halved, respectively. Local grid refinement is automated based on various criteria, such as density gradients, cut-cell and wall regions, or manually selected refinement regions. Additionally, a comprehensive and powerful tool for mesh generation and visualization, *INCA-BLOXX*, has been developed by Eberhardt [45].

3.6 Summary

In this chapter the numerical approach has been discussed. The compressible Navier-Stokes equations are solved in the computational fluid domain. Turbulent dissipation is considered by the Adaptive Local Deconvolution Method of Adams *et al.* [1] and Hickel *et al.* [80, 82]. The discretization scheme is optimized for cavitating flows by modifying the flux functions for density and scalars to a first or second order upwind reconstruction.

We have presented a framework for improving and extending cut-cell based immersed boundary methods with an emphasis on LES of weakly compressible and cavitating liquid flows. In the simulation of fuel injection systems the accurate treatment of moving and stationary parts is critical and generates additional complexity for the numerical method. Moreover, the method must be able to handle the opening and full closing of gaps in a conservative way.

Purely level-set based methods were found to be unsuitable for such applications. Strong artificial pressure and density fluctuations especially in cells in the vicinity of sharp corners of moving geometries in weakly compressible liquids were observed with such approaches. It has been shown that numerical errors of the grid-based level-set representation lead to a discontinuous evolution of fluid volume fraction in these cells.

For the computation of geometry parameters of cells cut by the interface we found it necessary to replace the level-set based approach by a more detailed representation of the fluid-solid interface. Intersections of the finite-volume cells with a given surface triangulation of the solid geometry are determined. With this conservative cut-element method we are able to compute the fluid volume fraction in a cut-cell directly from an arbitrarily

Algorithm 3 INCA flow solver

Setup simulation:
- distribute blocks on compute nodes
- setup domain
- initialize stationary IBs and walls
- initialize probes and sensorplanes

Run simulation:
repeat
  compute timestep Δt
  save old solution
  repeat
    compute interface exchange term
    compute physical fluxes
    scale physical flux in CCs with effective face apertures
    add interface exchange term to flux
    if last RK step **then**
      update moving geometries
      - shift stl-triangles
      - detect cuts with updated geometry
      - compute face apertures and CC volumes
      - update entries of moving IBs in BSP-tree
    end if
    switch CCs to conservative quantities
    advance fluid solution
    treat CCs
    - apply mixing to small CCs
    - return to cell-averaged quantities in CCs
    - extend solution at IBs
    update thermodynamics
  until RK steps reached
  write output
  compute statistics
until stopflag reached

accurate surface triangulation without further approximation. Sharp corners thus are represented with sub-cell resolution. Also, the treatment of closing or opening gaps becomes straightforward. The original interface interaction term, that contains normal stresses, shear stresses, and heat flux at the solid interface in cut-cells [86, 115], was modified to operate directly on individual cut-elements inside the cell. The method is especially attractive for immersed moving rigid geometries with prescribed body motion, as presented in this work, as well as for deformable structures, where the position and forces on the solid surface may be exchanged between the fluid and a structural solver in a triangulated form without any further interpolation. We emphasize that the effectiveness of the method is not limited to simple solid geometry motion (e.g. translational only).

4 Validation of the Immersed Boundary Method

In the following chapter, the ability of our method to represent complex geometries is shown. First, we validate our method with canonical flows around an oscillating cylinder in a fluid at rest, an in-line oscillating cylinder in a free stream, and two moving cylinders interacting with each other. We then demonstrate that the method allows for an accurate prediction of flows around moving obstacles in weakly compressible liquid flows with cavitation effects for a cavitating 2-D mixer. In particular, we show that the cavitating flow through a closing high-pressure liquid fuel injector control valve, which is an example for a complex application with interaction of stationary and moving parts, can be predicted by the method.

This section has partially been published in Örley et al. [132].

4.1 Cylinder Flows

4.1.1 In-Line Oscillating Cylinder in a Fluid at Rest

A well-documented model problem [22, 72, 95, 107, 168, 195] is the interaction of an oscillating circular cylinder with a surrounding fluid at rest. The two key parameters are the Reynolds number Re = $U_{max}D/\nu$ and the Keulegan-Carpenter number KC =

U_{max}/fD, with U_{max} being the maximum velocity of the cylinder, D the diameter of the cylinder, $\nu = \mu/\rho$ the kinematic viscosity of the fluid, and f the characteristic frequency of the oscillation. We selected a setup corresponding to the experiments and numerical simulations reported by Dütsch *et al.* [44] at Reynolds number Re = 100 and Keulegan-Carpenter number KC = 5. The translational motion of the cylinder is prescribed by a harmonic oscillation of the cylinder center with $x_c(t) = -A\sin(2\pi ft)$, where $A = \mathrm{KC}/2\pi$ is the amplitude of the oscillation. We consider a computational domain with $L_x = 55D$ and $L_y = 35D$ with a convective outflow boundary condition applied at all boundaries. Three different grid resolutions were tested (coarse: 126 x 100, medium: 250 x 200, and fine: 500 x 400). Grid-stretching was applied towards the boundaries in such a way that a uniform grid of 40 x 40 (coarse), 80 x 80 (medium), and 160 x 160 (fine) was maintained in the region of $-D \leq x \leq D$ and $-D \leq y \leq D$, which corresponds to a cell size of $0.05D$, $0.025D$, and $0.0125D$ near the cylinder.

All computations are initialized in a fluid field at rest. A total time of $\Delta t_{trans} = 8T$ (eight cycle periods T) is computed prior to the analysis to allow for a decay of initial disturbances until periodic vortex shedding is established. We choose a Mach number of $Ma_\infty = 0.3$ based on the maximum velocity u_{max} in an ideal gas to allow for comparison with incompressible results reported in the literature.

In Fig. 4.1, iso-contour lines for the pressure (left) and vorticity field (right) are shown for four different phase angles. The pressure field is perfectly symmetric with the stagnation point located on the axis of motion. In Fig. 4.1 a/b, the cylinder moves to the left with a velocity U_{max}. Two counter-rotating vortices develop that separate at the turning point of the cylinder at the left-most location (Fig. 4.1 c/d). During the reverse cycle, the same process takes place. While moving back into its own wake, the vortex pair created in the previous half-cylce is pushed away by the cylinder, see Fig. 4.1 e/f. The results compare very well with results reported in the literature (e.g., Fig. 8 of Ref. [195] or Fig. 12 of Ref. [107]) and show that the present method for moving obstacles can properly capture the dynamic process without producing any spurious oscillations of the field quantities.

For a quantitative evaluation of our data, we extract velocity profiles in axial and lateral direction at different x-locations ($x = -0.6D$, $x = 0.0D$, $x = 0.6D$, and $x = 1.2D$) for various phase angles (180°, 210°, and 330°). Fig. 4.2 shows our results for the comparative grid study. Results for the coarse, medium and find grid differ very little. Results for the fine grid are compared to reference data from literature in Fig. 4.3. Lines denote the present study and the reference data of the numerical results of Liao *et al.* [107] and experimental data of Dütsch *et al.* [44] are shown with filled and empty symbols, respectively. The overall comparison is very good.

In Fig. 4.4 the time evolution of the in-line force acting on the cylinder, F_x, as well as the pressure force $F_{x,p}$ and viscous component, $F_{x,\nu}$, are shown together with results for F_x obtained from the boundary-conforming simulation of Dütsch *et al.* [44]. The force acting on the cylinder surface is obtained by summation of all cut-element interface exchange terms. Agreement with the reference data is very good, confirming that also integral quantities can be accurately computed with the present method.

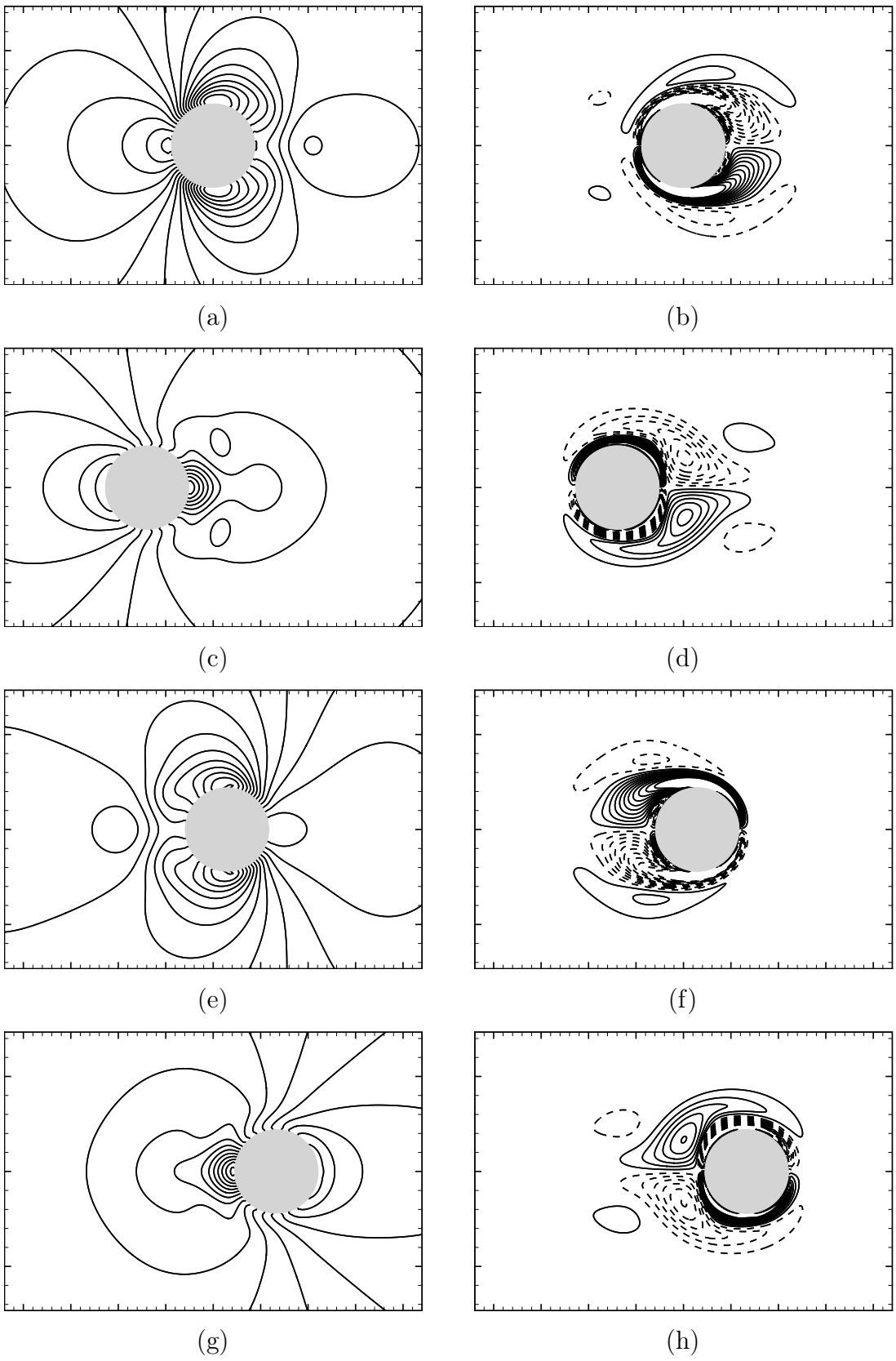

Figure 4.1: In-line oscillating cylinder in a fluid at rest (Re = 100 and KC = 5). Pressure (left) and vorticity contours (right) at four different phase-angles (top to bottom): 0°, 96°, 192°, 288°.

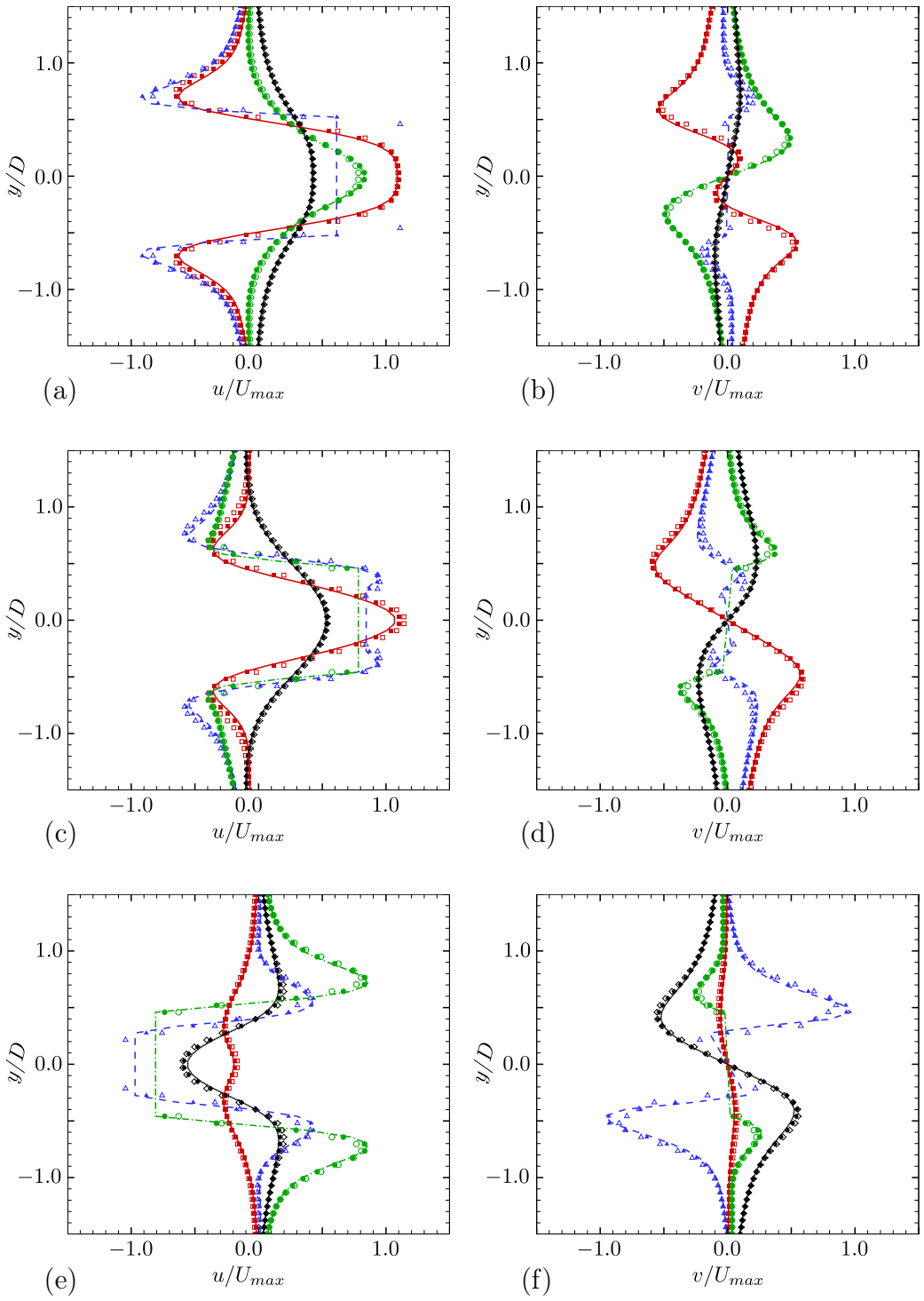

Figure 4.2: Grid resolution study for the in-line oscillating cylinder in a fluid at rest (Re = 100 and KC = 5). Comparison of velocity profiles in axial and lateral direction at 180° (a/b), 210° (c/d), and 330° (e/f) at four different x-locations: (— and □) $x = -0.6D$, (- - - and △) $x = 0.0D$, (-·- and ◯) $x = 0.6D$, and (··· and ◇) $x = 1.2D$. Empty symbols correspond to the coarse mesh (126 x 100), filled symbols correspond to the medium mesh (250 x 200), line plots correspond to the fine mesh (500 x 400).

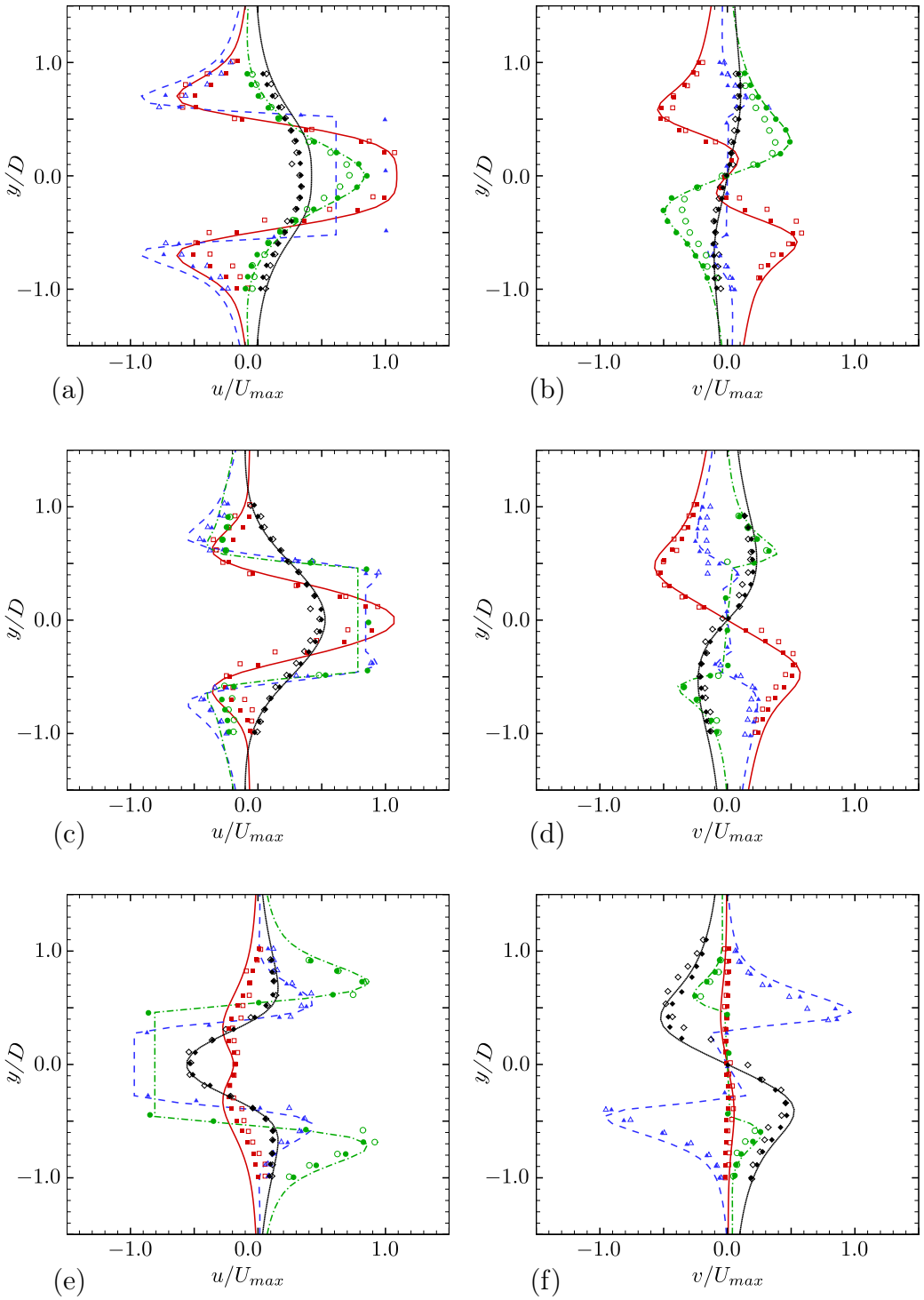

Figure 4.3: In-line oscillating cylinder in a fluid at rest (Re = 100 and KC = 5). Comparison of velocity profiles in axial and lateral direction at 180° (a/b), 210° (c/d), and 330° (e/f) at four different x-locations: (— and □) $x = -0.6D$, (- - - and △) $x = 0.0D$, (-·- and ◯) $x = 0.6D$, and (··· and ◇) $x = 1.2D$. Filled symbols correspond to the numerical results of Ref. [107], empty symbols to the experimental data of Ref. [44].

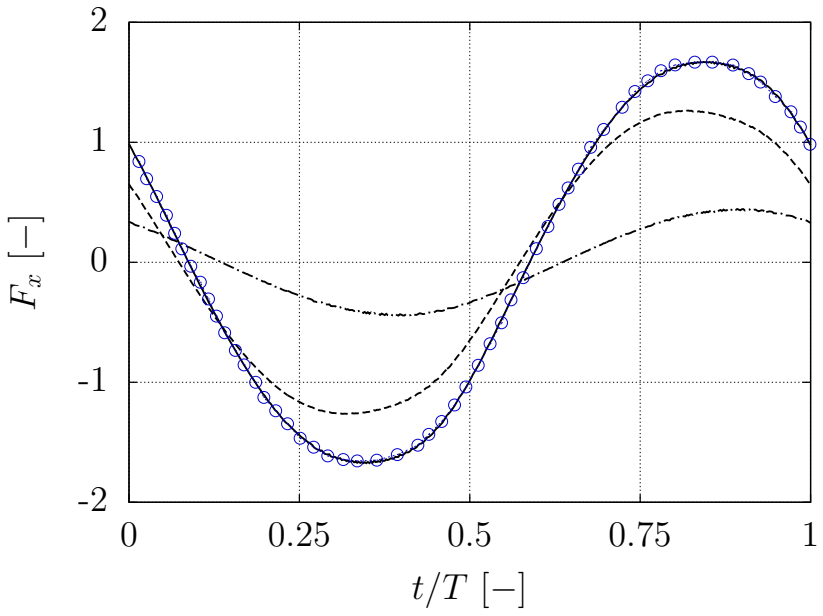

Figure 4.4: Time evolution of the in-line force acting on an oscillating cylinder in a fluid at rest (Re = 100 and KC = 5). Current simulation results: (—) F_x, (-·-) $F_{x,\nu}$, (- - -) $F_{x,p}$; (○) reference data of [44].

4.1.2 Flow Past an Oscillating Cylinder at Re=100

Another reference case often reported in the literature is the flow past an in-line oscillating cylinder in a free stream at a Reynolds number of Re = 100 based on free stream velocity u_∞ and cylinder diameter D [89, 107, 177]. According to experimental findings of Hurlbut *et al.* [89], choosing a oscillation frequency of the cylinder of approximately twice the Strouhal frequency of the vortex shedding causes a phase-locking, which effectively increases the drag coefficient $C_{D,mean}$ and maximum lift coefficient $C_{L,max}$.

We choose a computational domain with a total length of $L = 240D$ and a total height of $H = 60D$ to avoid spurious reflections at the in- and outflow boundary conditions. A local mesh refinement is applied around the cylinder. The resolution in the vicinity of the cylinder is $\Delta x = \Delta y = 0.025D$ for the coarse and $\Delta x = \Delta y = 0.0125D$ for the fine grid. As in the previous case, we choose a Mach number of $Ma_\infty = 0.3$ in an ideal gas environment. Non-reflecting boundary conditions are applied at the in- and outlet, whereas farfield boundary conditions are applied at the bottom and top.

The flow is evolved in time without oscillation of the cylinder until a periodic vortex shedding is observed. The resulting Strouhal number $\mathrm{St} = f_q U_\infty / D = 0.166$, with f_q being the vortex shedding frequency and U_∞ the free stream velocity is then used to modulate the motion of the cylinder by $u_c(t) = 2\pi f_c A \cos(2\pi f_c t)$, where u_c is the cylinder velocity and A is the amplitude of the oscillation. The prescribed frequency of the cylinder motion f_c is chosen as twice the vortex shedding frequency $f_c = 2f_q$. After initial transition the computed drag and lift coefficients are averaged over 7 shedding cycles.

Table 4.1: Comparison of lift and drag coefficients of in-line oscillating cylinder in a free stream at Reynolds number Re = 100

Re=100	f_c/f_q	$C_{D,mean}$	$C_{L,max}$
Kim*et al.* [96]	0	1.33	0.32
	2	-	-
Meyer *et al.* [115]	0	1.26	0.34
	2	-	-
Liao *et al.* [107]	0	1.36	0.34
	2	1.71	0.95
Hurlbut *et al.* [89]	0	1.41	0.31
	2	1.68	0.95
Su *et al.* [177]	0	1.40	0.34
	2	1.70	0.97
Present ($n = 40$)	0	1.44	0.36
	2	1.85	0.97
Present ($n = 80$)	0	1.39	0.33
	2	1.73	0.93

A qualitative analysis of the flow field is shown in Fig. 4.5. Here, the instantaneous vorticity contours are shown as a time series over one shedding cycle. A significant amplification of the vortical structures in lateral direction with respect to the free stream velocity and axis of cylinder motion is observed. A quantitative measure of this effect is provided in Tab. 4.1, showing the averaged drag and maximum lift coefficients for stationary and oscillating cases in comparison with results from literature. Additionally, results for computations without cylinder oscillation by Kim *et al.* [96] and Meyer *et al.* [115] have been included for comparison. The results show a good quantitative agreement with the reference data for the fine grid for both moving and non-moving cases, whereas small deviations in the drag coefficient are observed for the coarse grid. We conclude that our method is able to capture local and global flow properties for moving-boundary problems.

4.1.3 Two Interacting Moving Cylinders at Re=40

As a last validation case including multiple moving objects we study the interaction of cylinders with diameter D moving with respect to each other in a fluid at rest. This test case was first proposed by Russell and Wang [154] and was adopted by Xu and Wang [194] and Liao *et al.* [107]. The initial configuration is sketched in Fig. 4.6. In the following, spatial and temporal quantities are given in non-dimensional form. Reference values are given by $L^\star_{ref} = D^\star = 1$ m and $u^\star_{ref} = 1$ m/s.

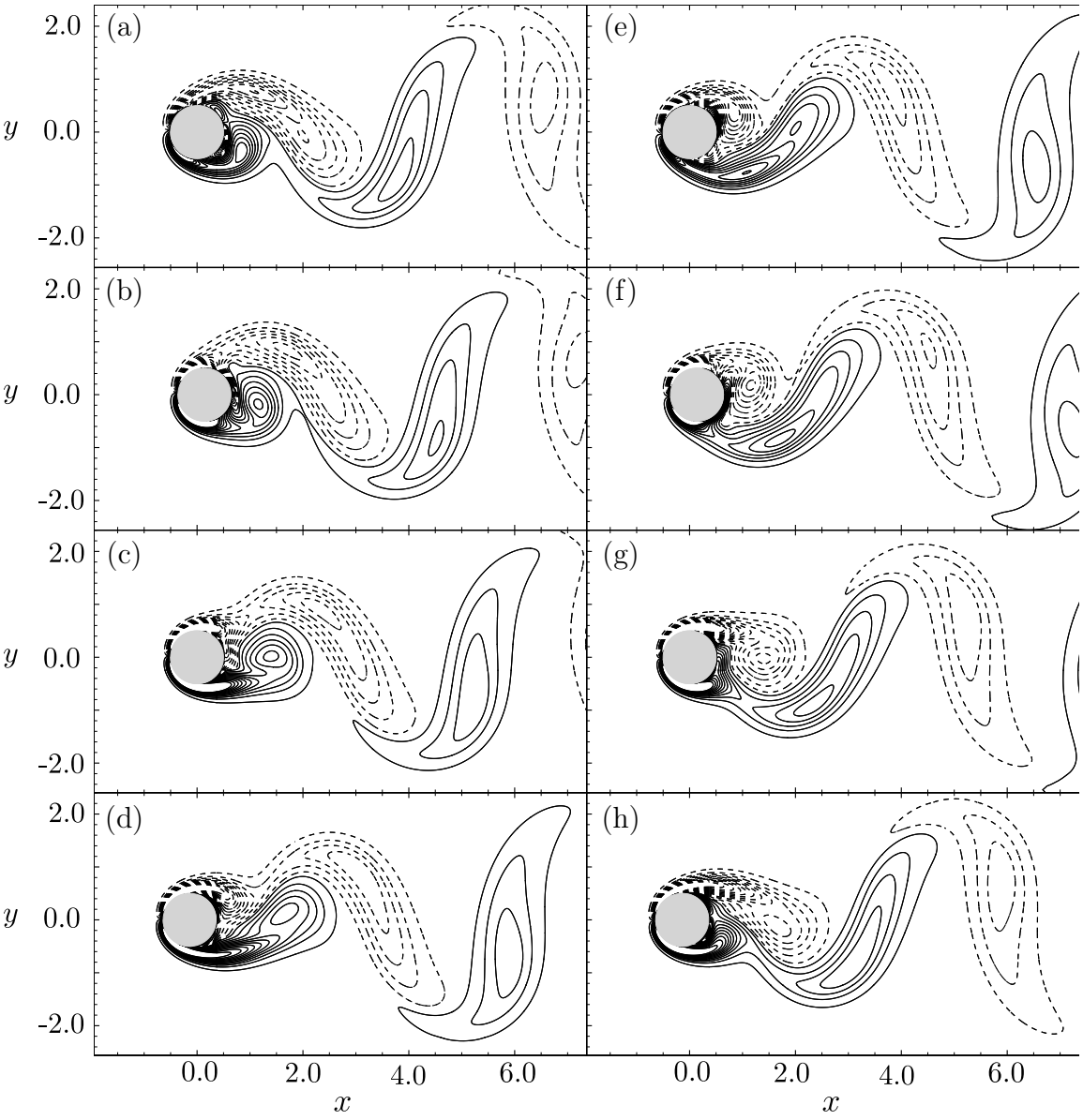

Figure 4.5: Instantaneous vorticity iso-contours of $-6 \leq \omega_z \leq 6$ in the vicinity and wake of an oscillating cylinder in a free stream at $Re = 100$. Solid and dotted lines show positive and negative values of ω_z, respectively: (a) $t = T/4$;(b) $t = T/2$;(c) $t = 3T/4$;(d) $t = T$;(e) $t = 5T/4$;(f) $t = 3T/2$;(g) $t = 7T/4$;(h) $t = 2T$; T is the oscillation period of the cylinder.

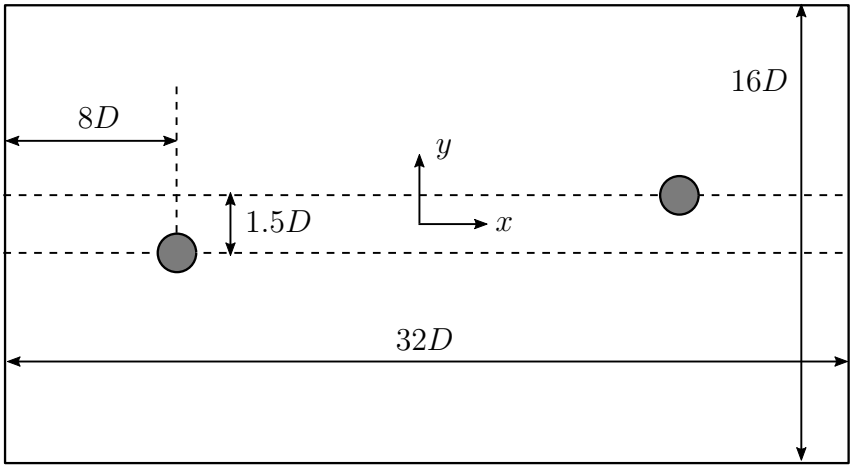

Figure 4.6: Initial configuration for two interacting, moving cylinders at Re=40. The total domain size is $32D \times 16D$.

We simulate a domain of spatial dimensions $32D \times 16D$. The cylinders are placed symmetrically at $8D$ away from the side-walls and with a distance of $1.5D$ to each other in y-direction. We maintain a constant grid spacing with 372×252 cells in the interaction region of $-3D \leq x \leq 3D$ and $-3D \leq y \leq 3D$. Otherwise, a grid stretching is applied to minimize computational costs. At all boundaries we apply a linear extrapolation of the solution. To compare our results with the incompressible reference data, we set the Mach number to $Ma = 0.1$ in an ideal gas environment.

The domain is initialized at rest. In the initial phase, $0 \leq t < 16$, we let the cylinders oscillate symmetrically about their initial position to avoid spurious pressure waves due to impulsive start of the cylinders. After that, we move the cylinders towards each other for a time period of $16 \leq t \leq 32$ at a Reynolds number Re=40. The motion of the cylinder is thus prescribed as

$$u_U = \begin{cases} -\cos(\pi t/4) & , 0 \leq t < 16 \\ -1 & , 16 \leq t \leq 32 \end{cases} \tag{4.1}$$

for the upper cylinder (denoted with subscript U), and

$$u_L = \begin{cases} \cos(\pi t/4) & , 0 \leq t < 16 \\ 1 & , 16 \leq t \leq 32 \end{cases} \tag{4.2}$$

for the lower cylinder (denoted with subscript L).

The resulting flow field for the interaction of the two moving cylinders at time $t = 24$, at which the cylinders are at their closest position, is shown in Fig. 4.7. The upper figure shows vorticity contours, the lower figure shows the pressure contours at the same instant in time. A strong rise in vorticity magnitude is observed, which goes hand in hand with a decrease in pressure. Otherwise the flow field is perfectly symmetric and no spurious pressure oscillations are detected. At time $t = 32$, Fig. 4.8, the two cylinders have passed each other. The vorticity contours reveal the interaction of the two wakes. The plots compare well to the results presented by Xu and Wang [194].

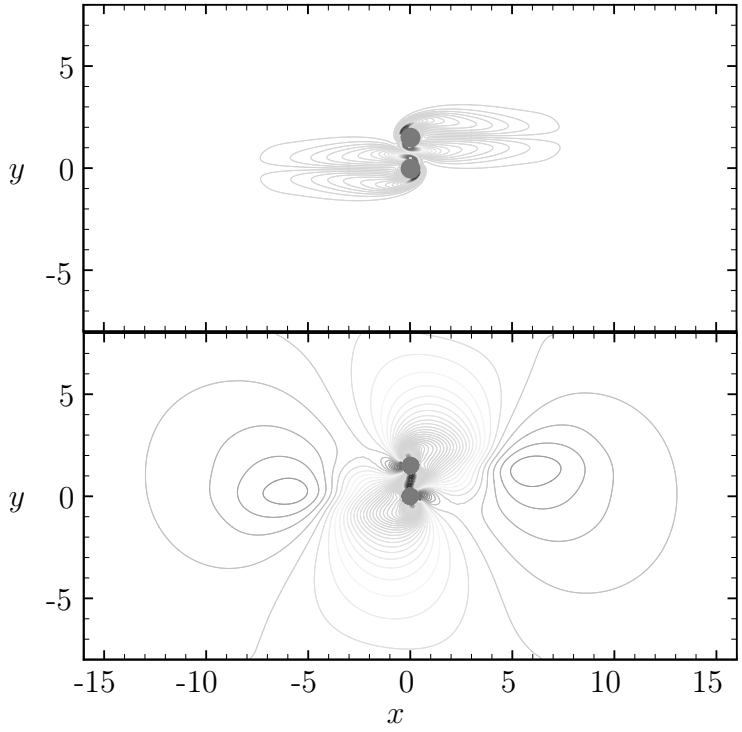

Figure 4.7: Contours of vorticity (upper figure) and pressure (lower figure) around two interacting cylinders at time $t = 24$.

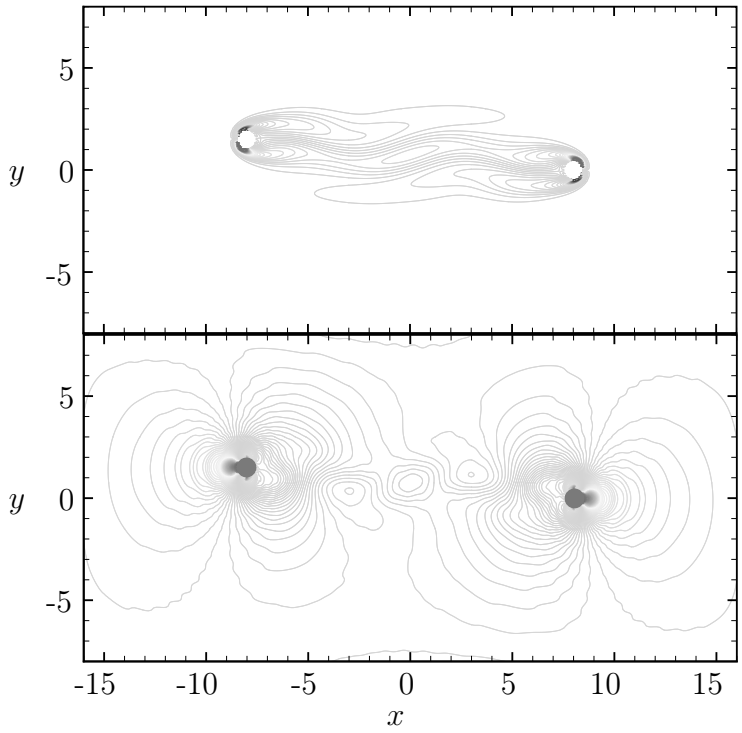

Figure 4.8: Contours of vorticity (upper figure) and pressure (lower figure) around two interacting cylinders at time $t = 32$.

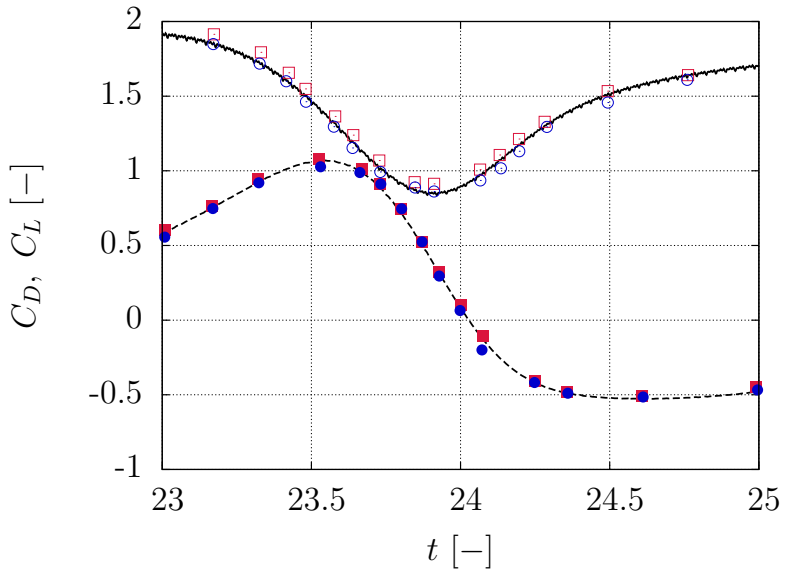

Figure 4.9: Lift coefficient C_L (- - - and filled symbols) and drag coefficient C_D (— and empty symbols) of the upper cylinder obtained from our simulation together with reference data of Liao *et al.* [107] (□) and Xu and Wang [194] (○).

A good quantitative agreement is also found in integral quantities. Figure 4.9 shows the lift coefficient C_L and drag coefficient C_D of the upper cylinder when passing the lower cylinder obtained from our simulation together with reference data of Liao *et al.* [107] and Xu and Wang [194]. The agreement with the reference data is very good. Both coefficients show almost no oscillations.

4.2 Moving Boundaries in Cavitating Flows

We apply the cut-element method to problem sets demonstrating its ability to deal with complex boundaries including sharp corners, stiff equations of state and flows with strong interaction of cavitation and turbulence. For the following test cases, we apply a single-fluid two-phase cavitation model based on the Tait equation introduced in Sec. 2.2.2.

4.2.1 Rotating Cross

First, we focus on rotating geometries in liquid water as a generic test case with possible application to turbopumps or ship propellers. We compute the flow around a rotating cross in liquid water, as sketched in Fig. 4.10, and compare our results with that obtained with a finite-volume ALE approach [36] on a body fitted grid within an inertial frame of reference. In this validation case physical viscosity is suppressed. The reference data of the finite-volume ALE approach were provided by Bernd Budich.

The setup is two-dimensional, the initial pressure is $p_{init} = 1\ bar$ and the surrounding fluid is at rest. The rotation is instantaneously started at the begin of the simulation with a constant angular velocity $\omega_z = 20\ rad/s$ around the axis of symmetry. Cavitation occurs due to strong expansions at concave corners of the moving geometry. The geometry is contained in a tank of significantly larger dimensions to minimize the effect of pressure waves reflected at the domain boundaries. In the ALE computations, the computational domain is circular with the same maximum dimensions as for the Cartesian grid. The mesh in the vicinity of the cross is shown in Fig. 4.11. The geometry is discretized with 20 cells (medium mesh) across the face of the bar d. The body-fitted grid (Fig. 4.11(a)) features a strong refinement towards the hub, whereas the Cartesian grid (Fig. 4.11(b)) maintains a constant grid spacing also in regions far from the hub.

A grid resolution study on a grid with 10 cells (coarse mesh) and 40 cells (fine mesh) across the face of the bar d has been performed. In Fig. 4.12 we present the vortex structures for all three grids at an angular position of 240° as well as 1% vapor-fraction contours shown as a red line. Significant differences in the main vortical structures are observed when comparing the coarse and the medium grid. Between the medium and the fine grid, the differences reduce to small-scale vortical structures that do not initiate cavitation. Otherwise, the overall agreement is good and the large-scale vortices are well resolved. Please note that in inviscid simulations full grid convergence cannot be achieved, since a mesh refinement recovers successively smaller vortical structures.

The strong initial acceleration leads to cavitation of the fluid at the suction side of the bars. This effect is more pronounced for the larger axis. This initial vapor sheet collapses after a short time, which is shown as a time series in Fig. 4.13 and is assessed with respect to prediction accuracy of the immersed boundary method. The collapse creates strong shock waves. A good agreement between the two different approaches is observed. The discretization scheme for the ALE method applies an up to second order reconstruction of the flow quantities, as well as a dissipative numerical flux function and thus, compared to the ALDM method, results in a stronger damping of small-scale acoustic waves caused by the collapse of vapor structures.

Figure 4.14 shows the instantaneous velocity magnitude at angular positions 120°, 240° and 360°. The 1% vapor-fraction contour is shown as a red line. The results for both methods are in good overall agreement. The results obtained on the medium Cartesian grid exhibit more small-scale details outside of the rotation region, where the body-fitted ALE grid is too coarse to resolve small vortical cavitation structures.

This effect is also observed in the integrated vapor volume fraction, see Fig. 4.15. The total vapor volume fraction α_{tot} for the medium and fine grid immersed boundary method, which again show similar results, is constantly larger than that for ALE due to the resolution of the small cavitating vortical structures in the outer region. On the coarse immersed boundary mesh, only the largest cavitating structures are resolved, and the total vapor volume fraction is underestimated.

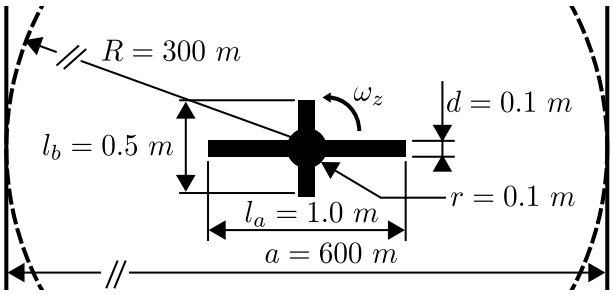

Figure 4.10: Setup for the simulation of the flow field around rotating cross in liquid water. Solid line: immersed boundary domain; dashed line: body fitted grid domain.

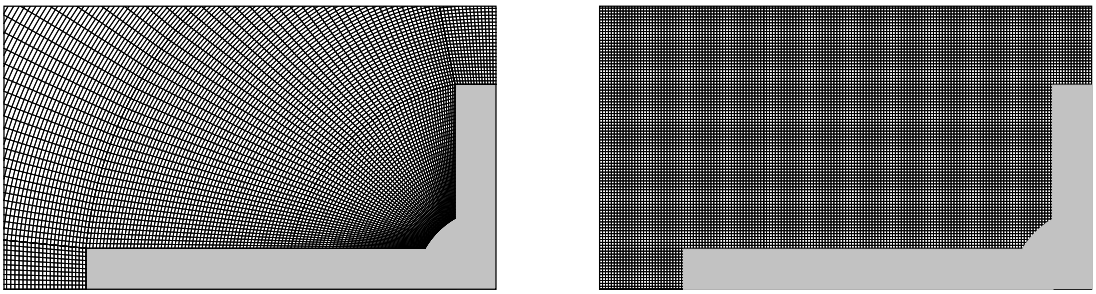

Figure 4.11: Mesh for the rotating-cross setup. Body-fitted grid for ALE simulation (a) and Cartesian grid for immersed boundary simulation (b)

4.2.2 Cavitating Flow through a Closing Control Valve

As a complex demonstration of the capability of our method we show results for a three-dimensional, viscous simulation of the flow through a high-pressure fuel injector control valve. We assess the effect of moving boundaries on the interaction of turbulence with cavitation.

The setup of the problem is sketched in Fig. 4.16. A round nozzle of diameter $d = 1.1\ mm$ opens into a square plenum with a width $H = 5.0\ mm$ containing the control valve needle. The needle has a diameter of $D = 1.5\ mm$ and is rounded at its tip. The valve seat is rounded with a radius of $r = 0.68\ mm$. The mesh used for the simulation is shown in Fig. 4.17. We use a total of $3.78 \cdot 10^6$ computational cells. The smallest cells in the vicinity of the valve seat are cubic with an edge length of $\Delta x = \Delta y = \Delta z = 10\ \mu m$. Mesh refinement is applied in the regions of interest and grid coarsening is used towards the in- and outflow channel. All channel walls and the control valve needle surface are no-slip walls.

The fluid domain is extended to the left and right to a total length of $x = \pm 1\ m$ to minimize artifacts from the farfield boundary conditions during the stimulated time span. Initially, the fluid domain is filled with water at rest. Upstream and downstream of the valve seat, the fluid is initialized with a pressure of $p_{high} = 200\ bar$ (shaded in red in Fig. 4.16) and $p_{low} = 1\ bar$ (shaded in blue), respectively. This imbalance creates a

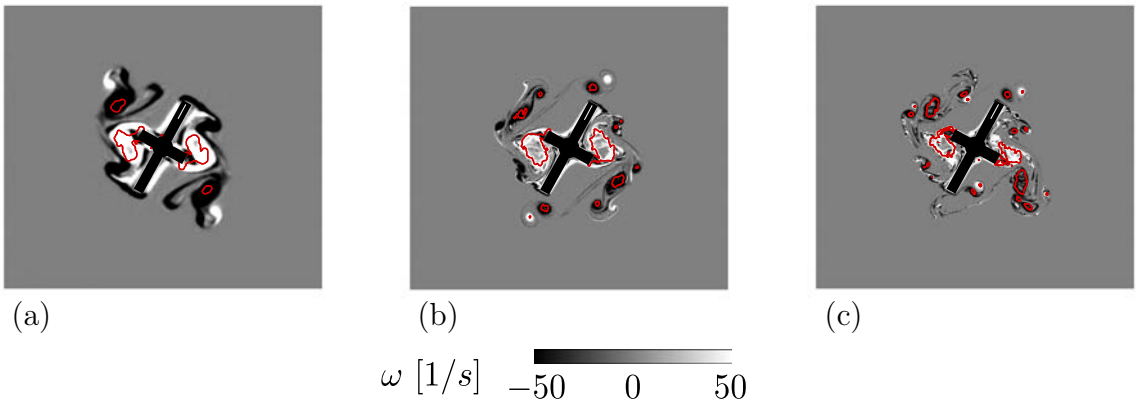

Figure 4.12: Instantaneous vorticity contour at 240° for three immersed boundary grid levels coarse (left), mid (center) and fine (right); 1% vapor iso contour shown as red iso line.

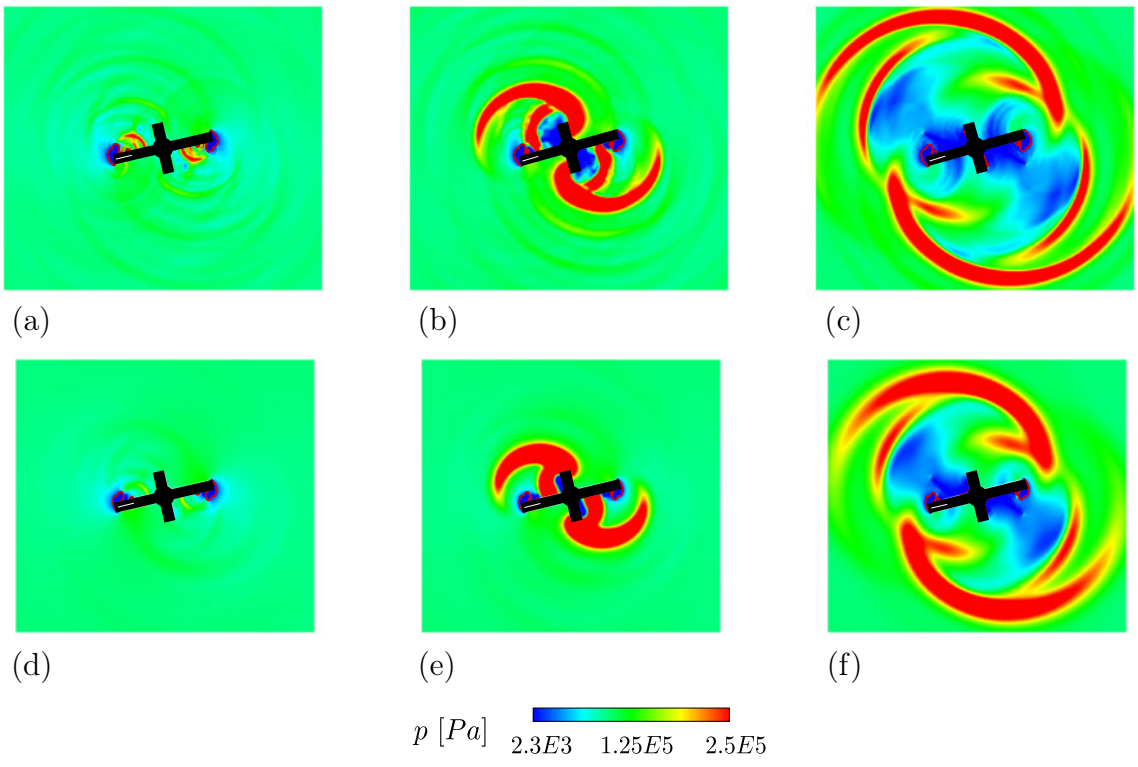

Figure 4.13: Pressure and 1%-vapor iso contour (red line) during collapse of the vapor structures created during initial acceleration. Immersed boundary (top) and ALE approach (bottom).

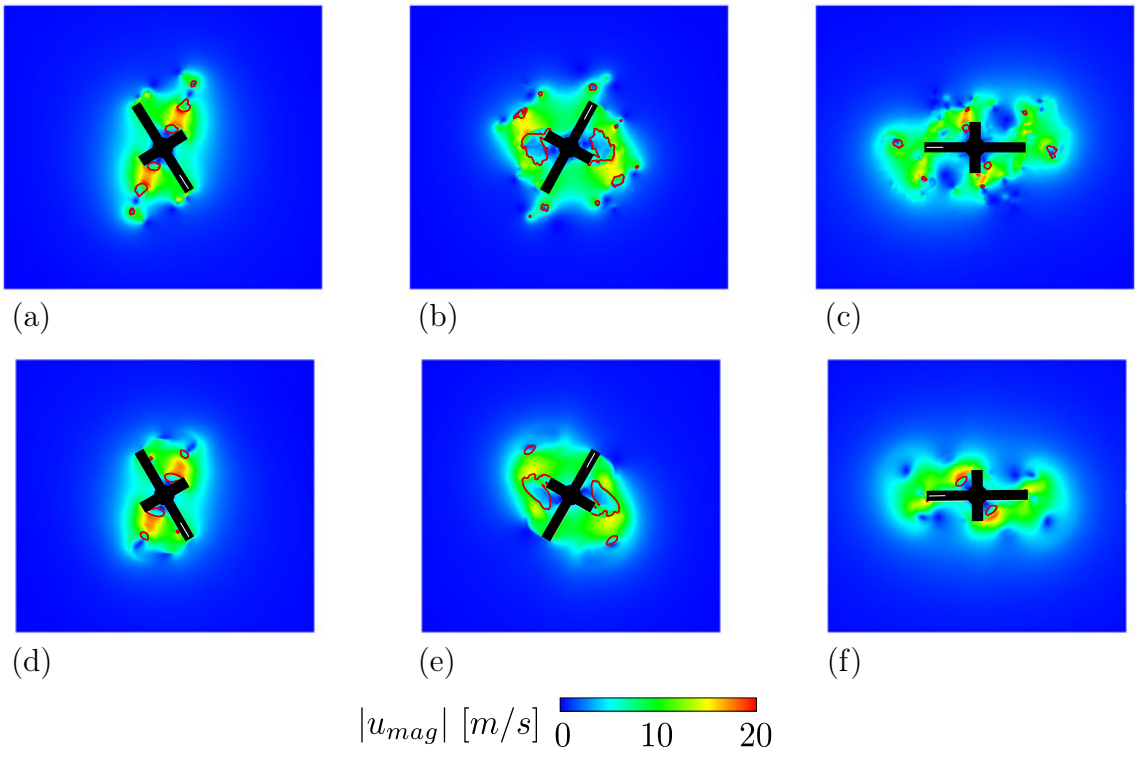

Figure 4.14: Instantaneous velocity magnitude at 120°, 240° and 360° (left to right); 1% vapor iso contour shown as red iso line. Immersed boundary (top) and ALE approach (bottom).

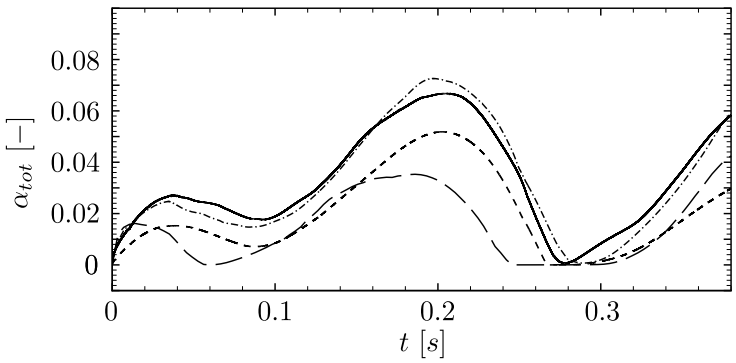

Figure 4.15: Integral vapor volume fraction α over time for ALE simulation (- -) and immersed boundary simulation: coarse (— —), medium (-·-) and fine (—) grid.

Riemann problem, where the left-running expansion wave accelerates the liquid towards the right and causes a steady flow into the outflow chamber.

The simulation is initialized with the needle sitting at its rightmost position (valve fully open). After starting the simulation, the needle is kept at rest for a time $\Delta t_{init} = 0.01\ ms$ to allow for an initial flow development. During the closing process, the needle is moved towards the valve seat over a distance of $\Delta l = 0.5\ mm$ with a constant velocity until the gap between the needle surface and the seat is sealed.

The time histories of the vapor volume fraction and the needle position are shown in Fig. 4.18 for three different closing speeds. It can be seen that a higher needle speed creates a larger total vapor volume fraction.

To assess the impact of the moving body on the flow field in detail, we present a visualization of instantaneous iso-contours of the Q-criterion $Q = 1.0 \cdot 10^{11}\ s^{-2}$ colored by the axial velocity and the vapor volume fraction $\alpha = 0.05$ in Fig. 4.19. Snapshots are taken at the instant in time where the needle reaches a position of $\Delta x = 0.49\ mm$, that is, for a gap width of 0.01 mm. For comparison, we include a snapshot for a stationary needle (Fig. 4.19(a)-(b)) as well as snapshots for moving needles with closing speeds of $u_{c1} = 1\ m/s$ (Fig. 4.19(c)-(d)), $u_{c2} = 5\ m/s$ (Fig. 4.19(e)-(f)) and $u_{c3} = 10\ m/s$ (Fig. 4.19(g)-(h)).

A significant impact on the turbulent structures is obvious when comparing the stationary simulation to a simulation with a moving boundary. In all moving cases, vortical structures are intensified as when compared to the stationary simulation. In addition, larger vapor structures are found outside the gap region. When comparing the different closing speeds, it is observed that a faster needle velocity suppresses the transition to a fully developed turbulent flow. Large vortex rings are visible in case of the fastest closing speed u_{c3}. Already for the slower closing speed u_{c2} these rings break up into smaller vortical structures. In case of very slow needle velocity, u_{c1}, a transition to developed turbulence is visible. The impact of the vortical structures on the vapor sheet formed by cavitation in the valve seat is apparent.

For slower speeds, the interaction with turbulent fluctuations ruptures the vapor sheet into smaller clouds, which are convected downstream in the vicinity of the surface. Thus, in terms of a prediction of erosion risk of the surface due to collapsing cavitation structures, this observation suggests that a high shutting speed could be beneficial despite of the larger vapor production. In this case, the main part of the vapor is contained in stable vortex rings far away from the surface of the needle. Small vapor clouds near the needle surface, in contrary, have a higher hydrodynamic aggressiveness and may cause significant damage to the surface structure during collapse. The needle motion in this setup may thus be considered as a key parameter to capture the correct turbulent characteristics of the flow and the erosion risk due to cavitation.

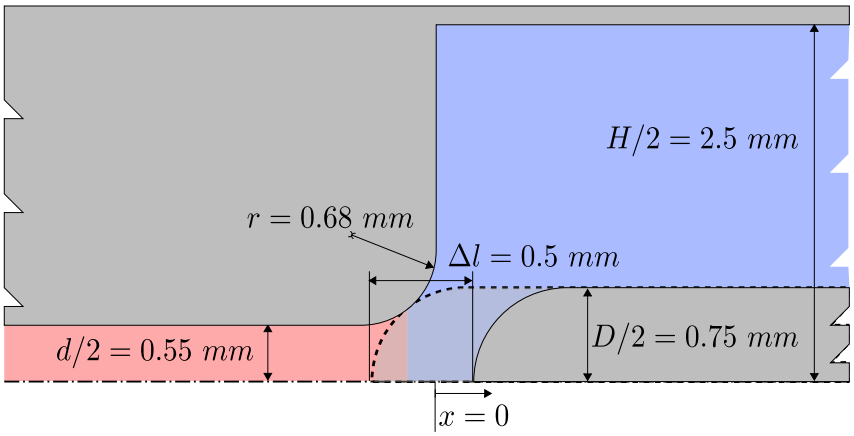

Figure 4.16: Setup for the closing-valve simulation shown as a half section. In- and outflow volume extend to $x_{min} = -1$ m and $x_{max} = +1$ m.

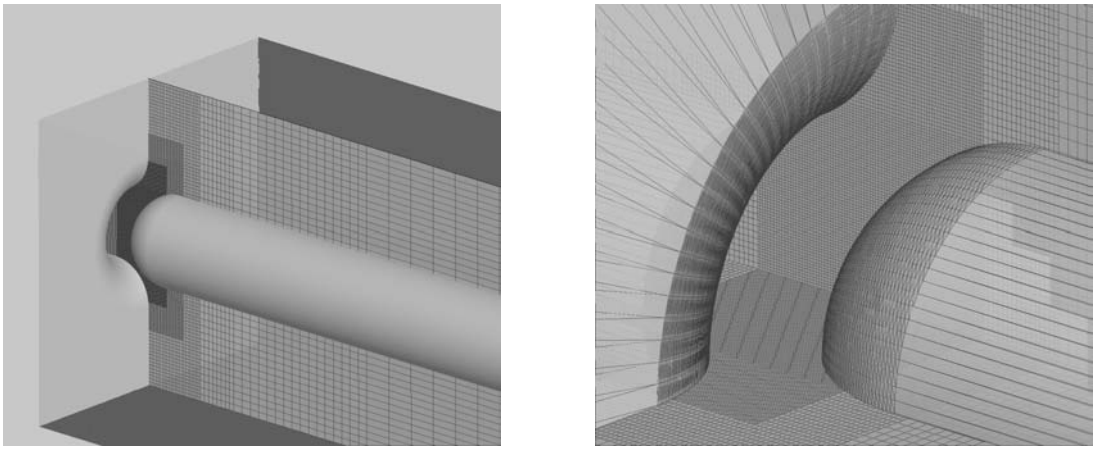

(a) (b)

Figure 4.17: Mesh and surface triangulation for the closing valve simulation.

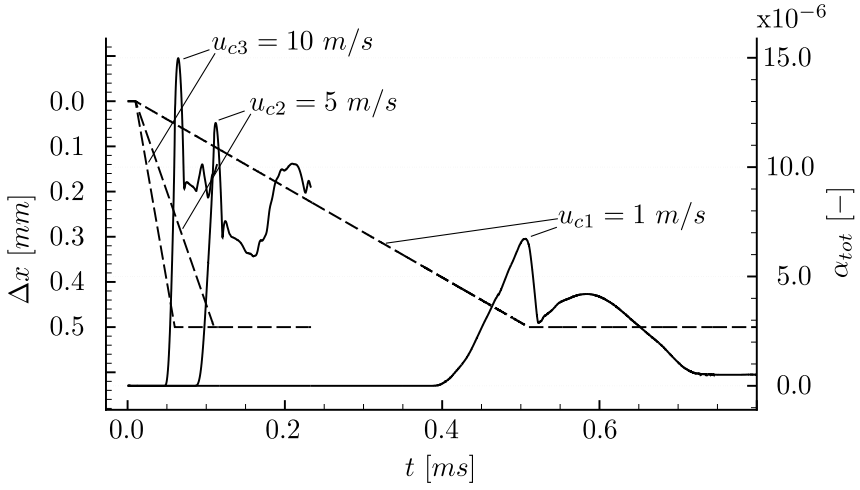

Figure 4.18: Integral vapor volume fraction α_{tot} (—) and needle position Δx (- - -) over time for needle closing speeds of $u_{c1} = 1\ m/s$, $u_{c2} = 5\ m/s$ and $u_{c3} = 10\ m/s$.

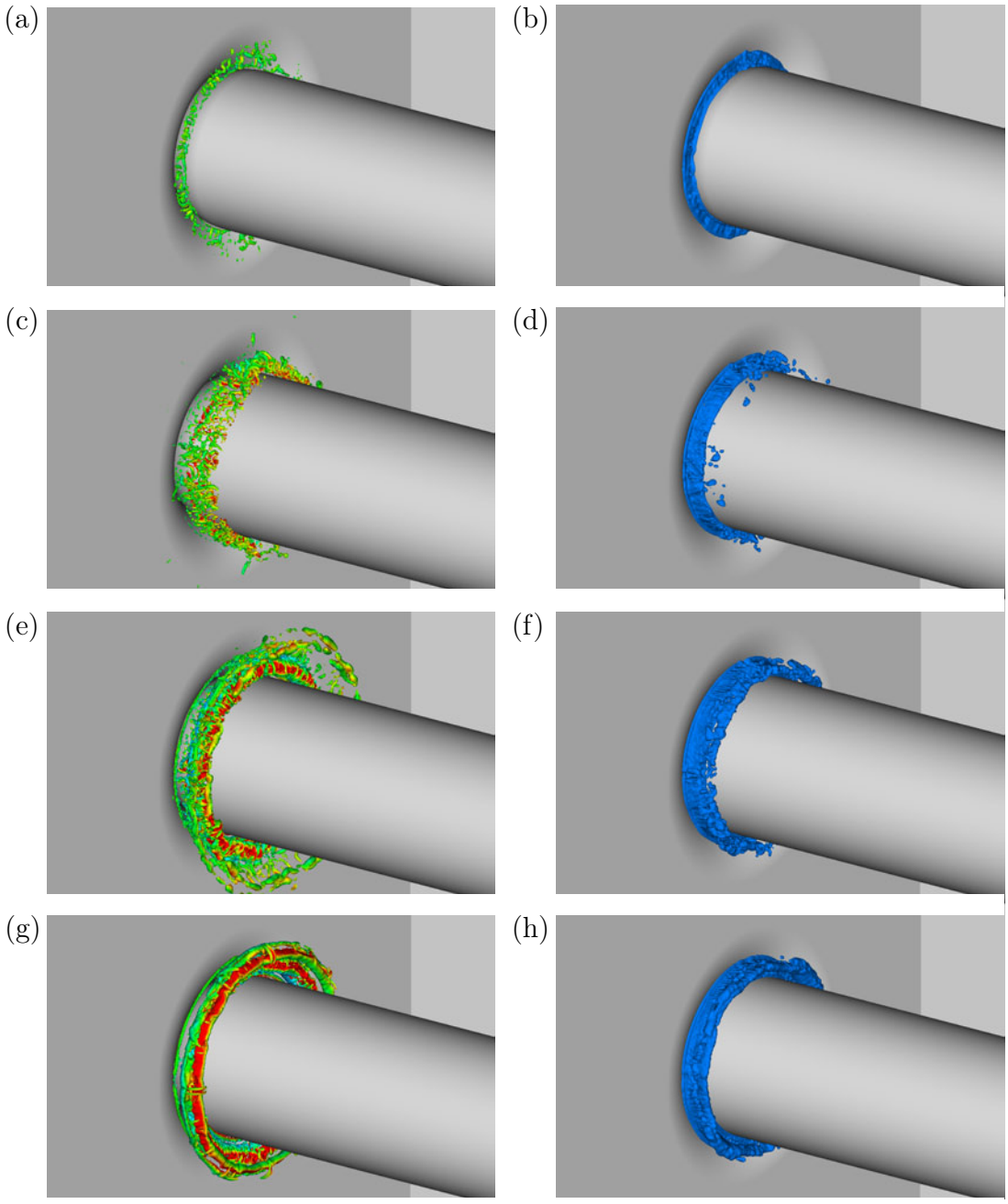

Figure 4.19: Visualization of instantaneous iso-contours of the Q-criterion $Q = 1.0 \cdot 10^{11}\ s^{-2}$ colored by the axial velocity (left column) and of the vapor fraction $\alpha = 0.05$ (right column). Snapshots are taken at the same position of the valve needle $\Delta x = 4.9\ mm$ for a stationary needle and closing speeds of $u_{c1} = 1\ m/s$, $u_{c2} = 5\ m/s$ and $u_{c3} = 10\ m/s$ (from top to bottom row).

4.3 Summary

To account for complex stationary and moving obstacles in cavitating flows, we have extended the Conservative Immersed Interface Method (CIIM) of Meyer *et al.* [70, 114, 115, 116] to represent solid geometries with sub-cell resolution.

Validation studies for oscillating and moving cylinders showed excellent agreement with the reference data with respect to flow structures and in terms of integral values such as lift and drag coefficients. A newly proposed test-case of a two-dimensional rotating mixer with sharp corners in liquid water showed good agreement with results obtained by Bernd Budich with a finite-volume ALE approach on a body-fitted grid.

We demonstrated the overall capability of our method for a three-dimensional simulation of the cavitating flow through a generic control valve, which is important for applications in fuel injection systems. The cut-element immersed boundary method shows good performance for cavitating flows of stiff liquids without exhibiting spurious pressure and density fluctuations at the interface which have rendered previous cut-cell approaches unsuitable for such flows.

5 Validation of the Cavitation- and Two-Fluid Model

In this chapter we discuss the performance of our thermodynamic models. First, we investigate simple collapse phenomena of isolated single bubbles without and with the presence of solid walls. Then, we present an extensive study of cavitating jet break-up inside a gas phase.

5.1 Single Bubble Collapse Events

We first validate our thermodynamic model for water without the effect of an additional gas content. In this study, we use the barotropic cavitation model based on the Tait equation for the liquid phase and the homogenous mixture model for the two-phase region, see Sec. 2.2.2. We investigate three-dimensional collapse events of vapor bubbles in the free field and in the vicinity of a solid wall.

5.1.1 Isolated Single Bubble Collapse

The temporal evolution of isolated single bubble collapse events has been extensively studied by theoretical and experimental approaches. The growth and collapse of a spherical

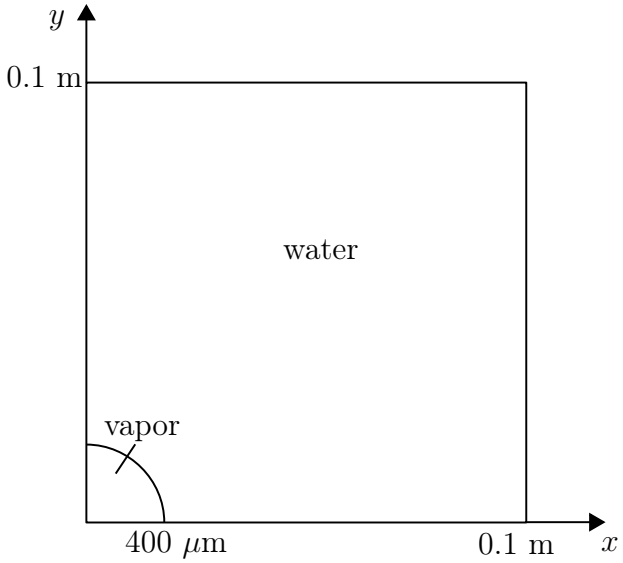

Figure 5.1: Schematic setup of collapse of an isolated single bubble.

vapor bubble, neglecting viscosity and surface tension, is described by the Rayleigh-Plesset equation

$$R\ddot{R} + \frac{3}{2}\dot{R}^2 = \frac{p_L - p_\infty}{\rho_\infty}, \tag{5.1}$$

see e.g. Young [197]. Here, R is the bubble radius, $\dot{R}$ and $\ddot{R}$ are the first and second time derivative, i.e., the velocity and acceleration of the bubble surface towards the bubble center, p_L is the pressure at the bubble surface, i.e., $p_L = p_{sat}$, and p_∞ and ρ_∞ are the pressure and density of the free field.

The bubble collapse time can be obtained by integration of Eq. 5.1 and was proposed by Rayleigh [148] as

$$t_{Rayleigh} \approx 0.915 R_0 \sqrt{\frac{\rho_\infty}{p_\infty - p_{sat}}}, \tag{5.2}$$

with the initial bubble radius R_0.

Following Sezal *et al.* [169] and Lauer *et al.* [104], we simulate the collapse of a spherical vapor bubble of radius $R = 400 \times 10^{-6}$ m. The setup is sketched in Fig. 5.1. The bubble is initialized with a vapor content of $\alpha_{init} = 99\%$. The free field pressure is set to $p_\infty = 1$ bar. We place the bubble at the center of a domain with length 0.1 m. Since the problem can be regarded as symmetrical, we only simulate one-eight of the bubble and apply symmetry boundary conditions where applicable, and outlet boundary conditions, otherwise. To assess the effect of grid resolution, we investigate three levels of grid refinement with 22 (coarse), 44 (medium), and 88 cells (fine).

The temporal evolution of the normalized bubble radius R/R_0 over normalized time $t/t_{Rayleigh}$ is shown in Fig. 5.2. The reference data shows the solution of the Rayleigh-Plesset equation. Even on very coarse grids, the collapse process is captured with good accuracy. We observe a grid convergence for the fine grid level, which shows excellent agreement with the reference data.

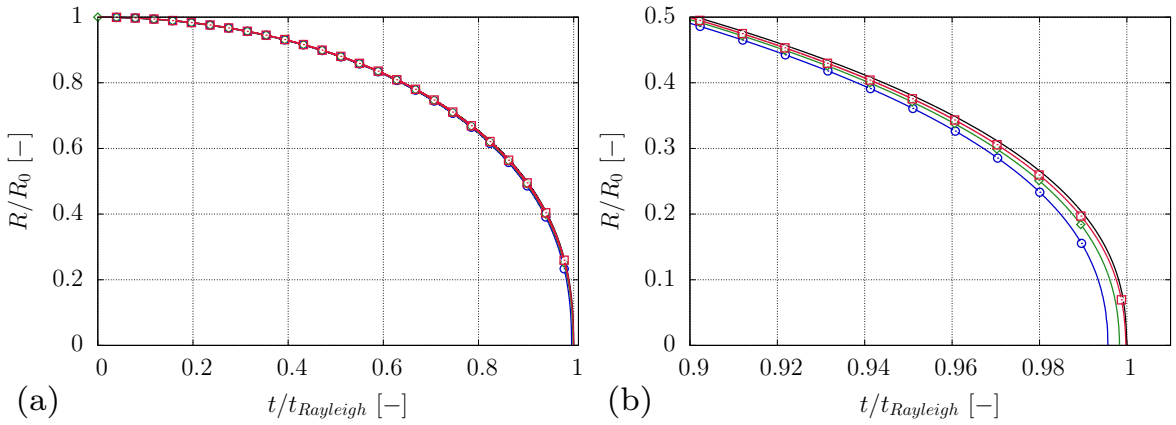

Figure 5.2: Temporal evolution of normalized bubble radius R/R_0 obtained on coarse (-○-), medium (-◇-), and fine grid (-□-), together with reference data (—).

5.1.2 Bubble Collapse near a Solid Wall

We investigate the collapse of a single, spherical vapor bubbles near a solid wall to compare our results to Lauer *et al.* [104] obtained with a two-fluid model including a sharp interface between gaseous and liquid phase. We adopt the setup of Lauer *et al.* and consider a single bubble with an initial radius of $R_0 = 400 \times 10^{-6}$ m, who's center is placed at a distance $d = 416 \times 10^{-6}$ m off the wall, see Fig. 5.3. The bubble is initialized with a vapor content of $\alpha_{init} = 99\%$. The free field pressure is set to $p_\infty = 100$ bar, which corresponds to a high-pressure environment typically found in the context of high-pressure pumps, control nozzles, and Diesel injectors. The grid spacing the vicinity of the bubble is equidistant and corresponds to a grid resolution of approx. 90 cells per initial bubble radius. Towards the outer boundaries, which are modelled as outflows and are located at a distance of $x, y, z = \pm 0.1$ m from the bubble center, we apply a grid stretching. We simulate the full bubble to evaluate asymmetries in the flow field during and after the bubble collapse.

Figure 5.4 shows the temporal evolution of the collapse process. At $t = 4.16 \times 10^{-6}$ s, Fig. 5.4(a), the early stage of the liquid jet is already visible. A region of increased pressure causes an acceleration of liquid towards the bubble center and, thus, towards the wall. At $t = 4.44 \times 10^{-6}$ s, Fig. 5.4(b), the liquid jet has already penetrated through most of the bubble and has impacted on the lower wall at $t = 4.51 \times 10^{-6}$ s, Fig. 5.4(c). This mechanism is considered to hold the greatest potential for surface erosion due to stresses inside the wall material. The impinging jet causes a strong shock wave, which travels back into the field and causes a collapse of the remaining vapor regions at $t = 4.57 \times 10^{-6}$ s, Fig. 5.4(d). A subsequent expansion wave interacts with vortical structures, Fig. 5.4(e/f), which originate from the liquid jet, and cause the evaporation of liquid and, finally, a secondary collapse at $t = 4.83 \times 10^{-6}$ s, Fig. 5.4(g). The liquid jet is deflected away from the point of impact in radial direction and rolls up in a vortex ring, Fig. 5.4(h). In the vortex core, vapor regions are found at $t = 5.12 \times 10^{-6}$ s, Fig. 5.4(i), which collapse and may cause the emission of shock waves and thus potential surface erosion around the jet impact point at later times, Fig. 5.4(j). Our results, which are obtained with a very

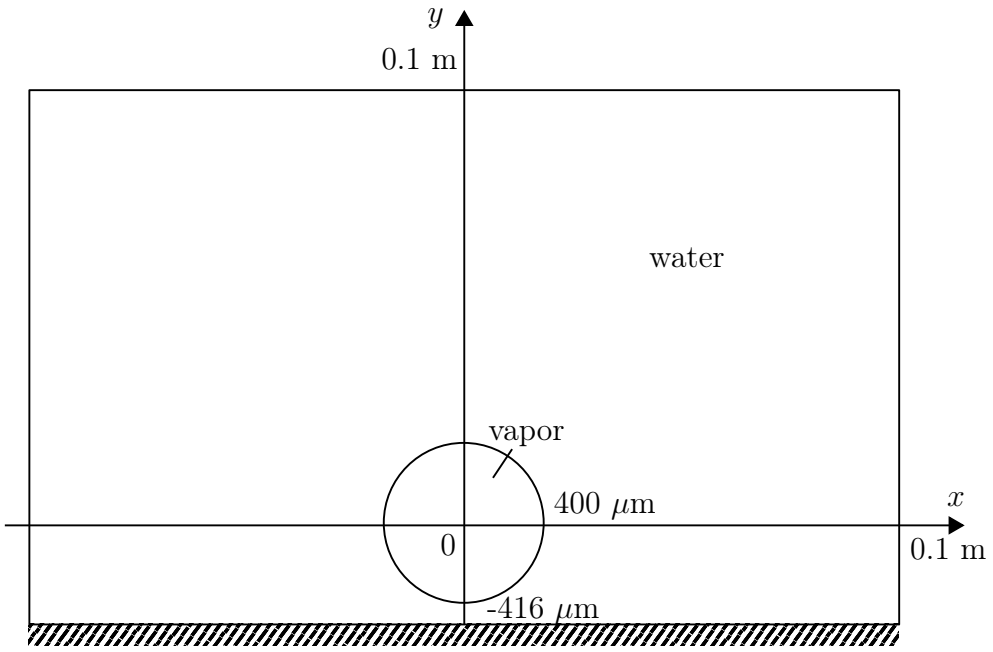

Figure 5.3: Schematic setup of collapse of a single bubble near a solid wall.

simple model, compare well to the findings of Lauer *et al.* [104], and in addition describe the formation of vapor in the low pressure regions after the initial collapse.

A three-dimensional view of the bubble surface visualized by the iso-surface of vapor volume fraction and the evolution of wall pressure are shown in Fig. 5.5. We study the effect of fluid viscosity. At $t = 4.29 \times 10^{-6}$ s, Fig. 5.5(a), the liquid jet is already developing. The first rebound is shown in Fig. 5.5(b). Differences between viscous and inviscid fluid description are found for times later than $t = 4.67 \times 10^{-6}$ s, Fig. 5.5(c). In the inviscid case, a higher rate of vapor production is found than in the viscous simulation. In combination with the inviscid wall, this circular vapor structure is convected further away from the impact point than in the viscous case, and is attached to the wall. In the viscous case, a stable, cavitating vortex ring is found, which only becomes disturbed and asymmetrical due to small asymmetries in the flow field at later times.

5.2 LES of Cavitating Nozzle Jets and Liquid Jet Break-Up

Finally, to validate our thermodynamic model including non-condensable gas effects, we investigate the complex break-up of a cavitating liquid injected into ambient air. The considered configuration follows the general setup of a reference experiment, and is a generic reproduction of a scaled-up fuel injector or control valve as found in an automotive engine. Due to the experimental conditions it operates, however, at significantly lower pressures. LES results are compared to the experimental reference for validation. Three different operating points are studied, which differ in terms of the development of

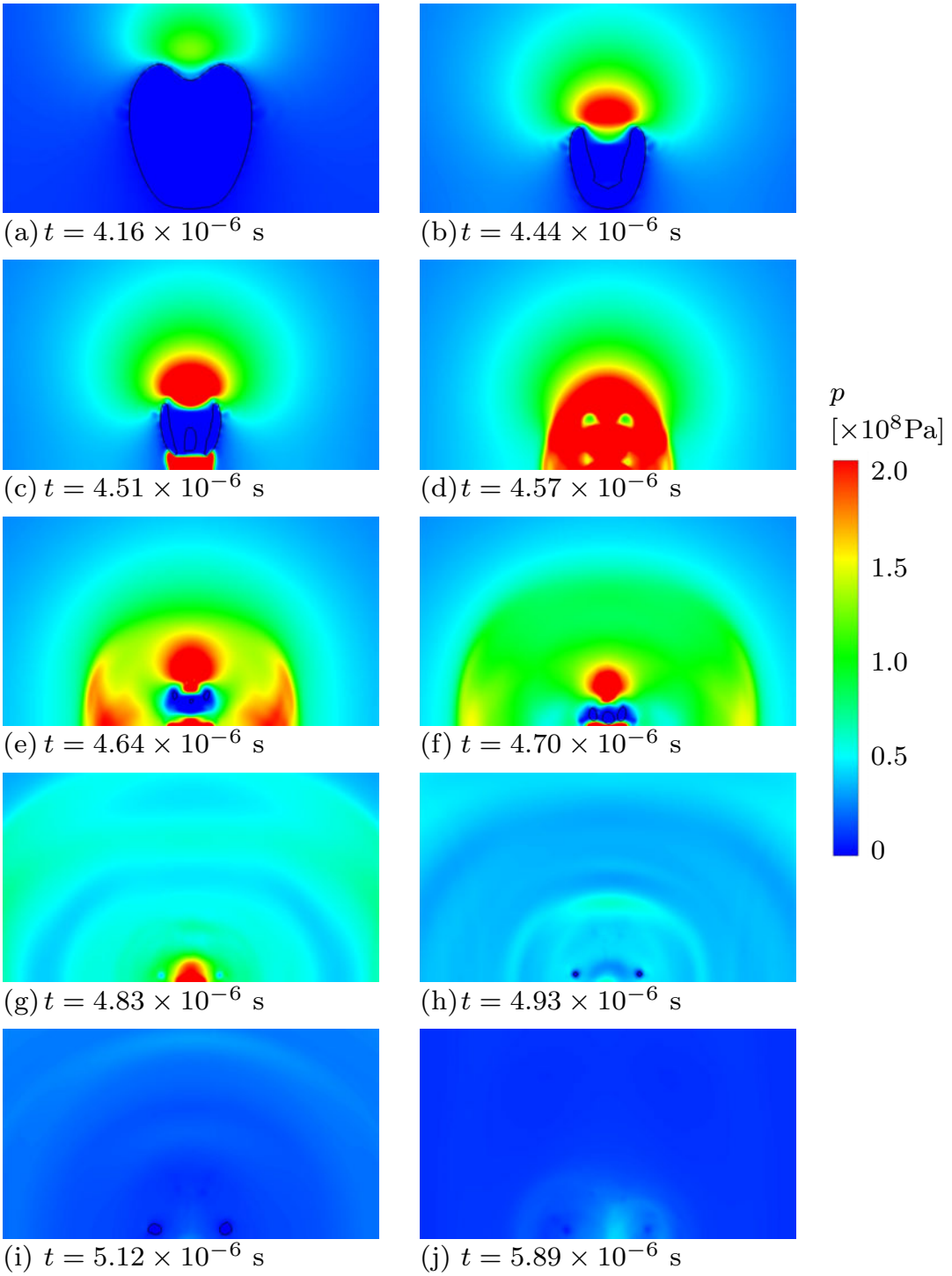

Figure 5.4: Collapse event of a single, spherical vapor bubble near a solid wall including viscous effects. Snapshots of instantaneous pressure field and iso-line of $\alpha = 5\%$ vapor fraction on the symmetry plane.

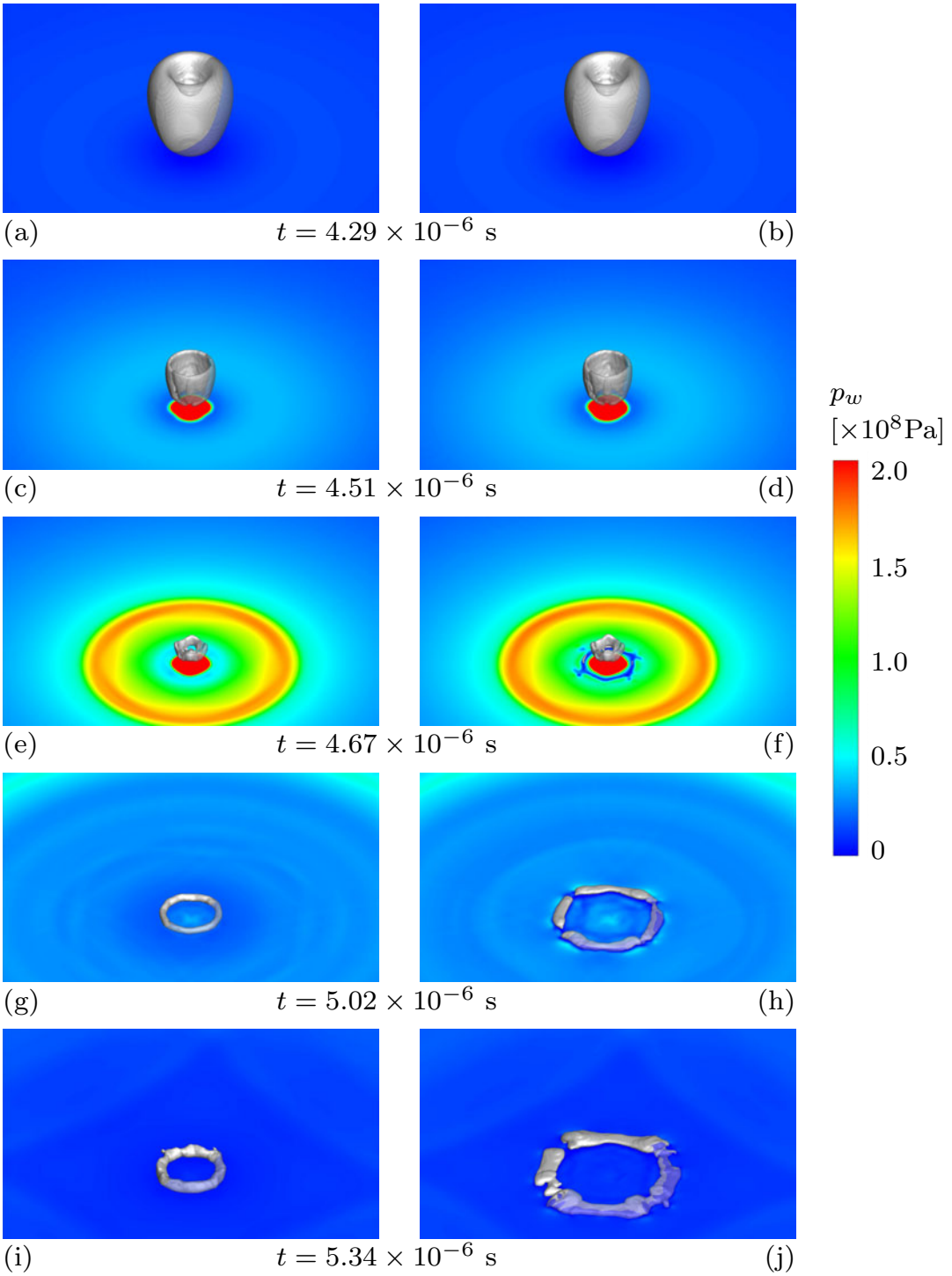

Figure 5.5: Comparison of single bubble collapse near a solid wall with (left column) and without (right column) considering viscous effects. Instantaneous wall pressure field p_w and iso-surface of $\alpha = 5\%$ vapor fraction.

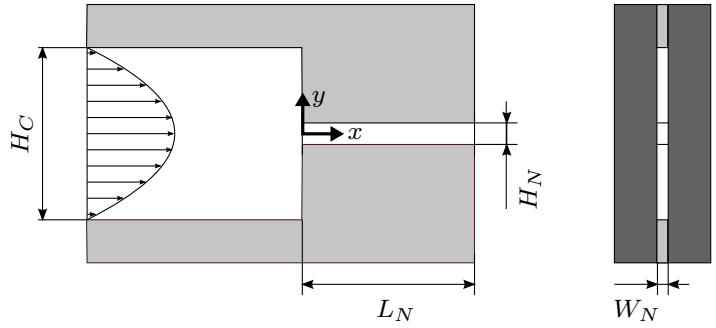

Figure 5.6: Schematic of the nozzle: side view (left), back view (right).

cavitation regions and the jet break-up characteristics. In the following test case, which involves a cavitating liquid water jet injected into air, we use the linearized equation of state for liquid water and liquid-vapor-mixtures described in Sec. 2.2.3.

This section has partially been published in Örley et al. [134]. Reprinted with permission from Örley, F., Trummler, T., Hickel, S., Mihatsch, M. S., Schmidt, S. J., & Adams, N. A. (2015). Large-eddy simulation of cavitating nozzle flow and primary jet break-up. Physics of Fluids, 27(8), 086101. Copyright 2015, AIP Publishing LLC. The simulation setup and grid was partially developed by T. Trummler [185], who in her work also performed preliminary studies on the cavitating channel flow for the presented and other operating points.

5.2.1 Setup and Grid

In the following, we present the experimental and computational setup, aside with a grid sensitivity study.

Experimental Setup

The setup adopted for this validation study was presented by Sou *et al.* [174, 175] and can be regarded as a large-scale, generic fuel injector as found in many automotive applications. A schematic of the setup is shown in Fig. 5.6. Dimensions are summarized in Tab. 5.1. The rectangular nozzle geometry consists of acrylic flat plates as front and back walls to gain optical access, and thin stainless steel plates of width $W_N = 1 \times 10^{-3}$ m to form the nozzle geometry of height $H_N = 4 \times 10^{-3}$ m and length $L_N = 16 \times 10^{-3}$ m. Upstream of the nozzle, the duct height is $H_C = 32 \times 10^{-3}$ m, which corresponds to a contraction ratio of 8:1, and can thus be regarded as a slot flow. The nozzle opens into a large reservoir of quiescent ambient air. In the following, we refer to the symmetry line crossing the nozzle inlet plane as the origin of an underlying Cartesian coordinate system.

Tap water at $T_w = 292$ K was processed through an air separation tank and used as working fluid. A plunger pump was used to control the flow rate and to prescribe a

Table 5.1: Geometric dimensions of the 2D nozzle

Parameter	H_N	L_N	W_N	H_C
Value [$\times 10^{-3}$ m]	4.0	16.0	1.0	32.0

cavitation number

$$\sigma = \frac{p_\infty - p_s}{0.5 \rho_L U_N^2}, \tag{5.3}$$

where $p_\infty = 1$ atm $= 1.01325 \times 10^5$ Pa corresponds to the surrounding pressure, ρ_L is the liquid density and U_N is the mean streamwise liquid velocity inside the nozzle. This non dimensional parameter relates the pressure difference of the surrounding and vapor pressure to the local dynamic pressure. The Reynolds number is defined as

$$Re = \frac{U_N H_N}{\nu_L} \tag{5.4}$$

with the liquid kinematic viscosity ν_L. Furthermore, we define the non dimensional cavitation length L_c^* as the ratio of the mean streamwise extent of the cavitation zone and the nozzle length L_N. The Weber number based on the nozzle height is

$$We = \frac{\rho_{liq,\infty} U_N^2 H_N}{\sigma_s}, \tag{5.5}$$

where σ_s is the surface tension coefficient.

Sou *et al.* [174, 175] investigated a variety of cavitation numbers $\sigma = \{0.65, 0.78, 1.27\}$. The non-dimensional parameters for the operation points investigated in this numerical study are provided in Tab. 5.2. The non-condensable gas-to-liquid dynamic viscosity ratio is $\eta = \mu_{gas,\infty}/\mu_{liq,\infty} = 1.82 \times 10^{-2}$ and the non-condensable gas-to-liquid density ratio is $\lambda = \rho_{gas,\infty}/\rho_{liq,\infty} = 1.21 \times 10^{-3}$. Note that, since surface tension is not included in our present model and the Weber number thus becomes infinity, we only focus on primary break-up, which is driven by inertia. This simplification is supported by the low non-condensable gas-to-liquid density and viscosity ratio, and the high Reynolds numbers. We do not consider secondary break-up and atomization, which is significantly affected by surface tension, in this work.

Sou *et al.* [174, 175] investigated a variety of cavitation numbers, where smaller values of σ represent cases of higher cavitation intensity. In Tab. 5.3, the different cases selected for this study are summarized together with their cavitation and jet characteristics observed in the experiment. For cavitation numbers $\sigma > 1.2$, no cavitation was observed ($L_c^* = 0$) and the jet was characterized as 'wavy jet'. For $0.75 \leq \sigma \leq 1.2$, cavitation zones at the inlet region of the nozzle started to develop ($L_c^* \sim 0.2 - 0.4$), while the liquid jet characteristics were not altered. A further decrease in the cavitation number to $0.55 < \sigma < 0.75$ led to a growth of the cavitation zones almost up to the whole nozzle length ($L_c^* \sim 0.8 - 0.9$) and enhanced primary jet break-up and jet atomization was observed.

Optical data were sampled by transmitted light imaging. Furthermore, quantitative data

Table 5.2: Experimental conditions investigated by Sou *et al.* [174, 175].

Mean liquid velocity U_N [m/s]	Cavitation number σ [−]	Reynolds number Re [−]	Weber number We [−]
12.5	1.27	50'000	8'562
16.0	0.78	64'000	14'029
17.5	0.65	70'000	16'783

Table 5.3: Experimental conditions proposed by Sou *et al.* [174, 175].

Cavitation number σ	Cavitation characteristics	Jet surface
1.27	No cavitation	Wavy jet
0.78	Developing Cavitation	Wavy jet
0.65	Supercavitation	Spray

for mean velocity and velocity fluctuations are available from LDV measurements. The water was seeded with silicone carbide particles. The effect of the particles on the flow-field was found to be negligible [175].

Computational Setup

The computational domain used in our study is sketched in Fig. 5.7 showing the block structure. The nozzle is connected to a large outlet region of $W_O = 160 \times W_N$, $H_O = 75 \times H_N$, and $L_O = 17.5 \times L_N$, which is employed to resemble the injection into free ambient air while avoiding any influence of the boundary conditions.

A total of $\Delta x = 24 \times 10^{-3}$ m of the inlet duct is computed to avoid spurious influence of the inlet boundary condition. At the inlet we prescribe a purely liquid water flow, i.e., $\xi_{G,in} = 0.0$. If not stated otherwise, we set a laminar, doubly parabolic stream-wise velocity profile

$$u = \frac{9}{4} U_B \left[1 - \left(\frac{y}{H_C/2} \right)^2 \right] \left[1 - \left(\frac{z}{W_N/2} \right)^2 \right], \tag{5.6}$$

The bulk velocity, $U_B = U_N/8$ according to the ratio of slot and inlet area, is set to match the corresponding Reynolds number for each operating point. We use Neumann conditions for the pressure at the inflow boundary and the density is computed from Eqn. 2.23. At the outlet we apply a static pressure boundary condition $p(y,z) = (p_{\text{out}} + p_{\text{lc}}(y,z))/2$, which is computed from the static pressure in the last cell layer, $p_{\text{lc}}(y,z)$, and the prescribed pressure $p_{\text{out}} = 1$ atm. This methodology reduces spurious reflections at the outlet while asymptotically maintaining the desired outlet pressure. All other quantities are extrapolated linearly. Walls are treated as adiabatic with no-slip condition for the velocity components and Neumann conditions for all other quantities. The domain is initialized at rest and is filled with purely liquid water without non-condensable gas

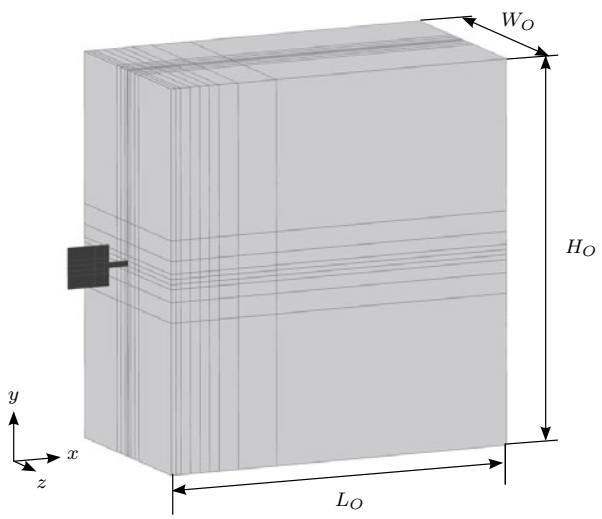

Figure 5.7: Computational domain and block structure of the quasi two-dimensional throttle (shaded dark gray) connected to a large outflow reservoir (shaded light gray).

component (i.e. $\xi_G = 0$) inside the nozzle for $x < 16 \times 10^{-3}$ m, and gas (i.e. $\xi_G = 1$) for $x \geq 16 \times 10^{-3}$ m in the outlet region. The initial pressure is set to $p_{\text{init}} = 1$ atm.

We discretize the domain on a Cartesian block-structured mesh. To reduce computational cost we employ a successive grid refinement in the nozzle and near nozzle inlet and outlet during the simulation. For each case, initially we let the mean flow develop over a long period of time of approximately 100 flow-through times of the nozzle on a coarse grid, which consists of roughly 2.7×10^6 cells. As soon as the flow has developed, we refine the grid over several intermediate levels until the final grid resolution is reached. We ensure a steady or periodic signal of the global vapor mass fraction at each level before refining the grid. In every step, the grid is refined near the nozzle wall and outflow region by a ratio of 2 : 1, and the solution of the previous level is interpolated onto the refined grid. At grid interfaces of different resolution, we apply a conservative interpolation procedure. We propagate the flow solution on three intermediate grids before sampling data on the fine grid. The fine grid, which is shown in Fig. 5, contains 43.1×10^6 cells with a smallest cell size of 3.91×10^{-6} m at the nozzle walls and at the inlet and outlet edges. An analysis on the grid convergence behavior is given below.

Three-dimensional statistical data of the flow field was sampled on the fine grid every 100 computational time steps ($\Delta t_s \approx 0.6 \times 10^{-7}$ s), which corresponds to a sampling frequency of $f_s \approx 14$ MHz, over an interval of at least $\Delta t_{avg} = 3 \times 10^{-3}$ s, which corresponds to approx. three flow-through times of the nozzle. Time averaged quantities are denoted by $\langle \bullet \rangle$.

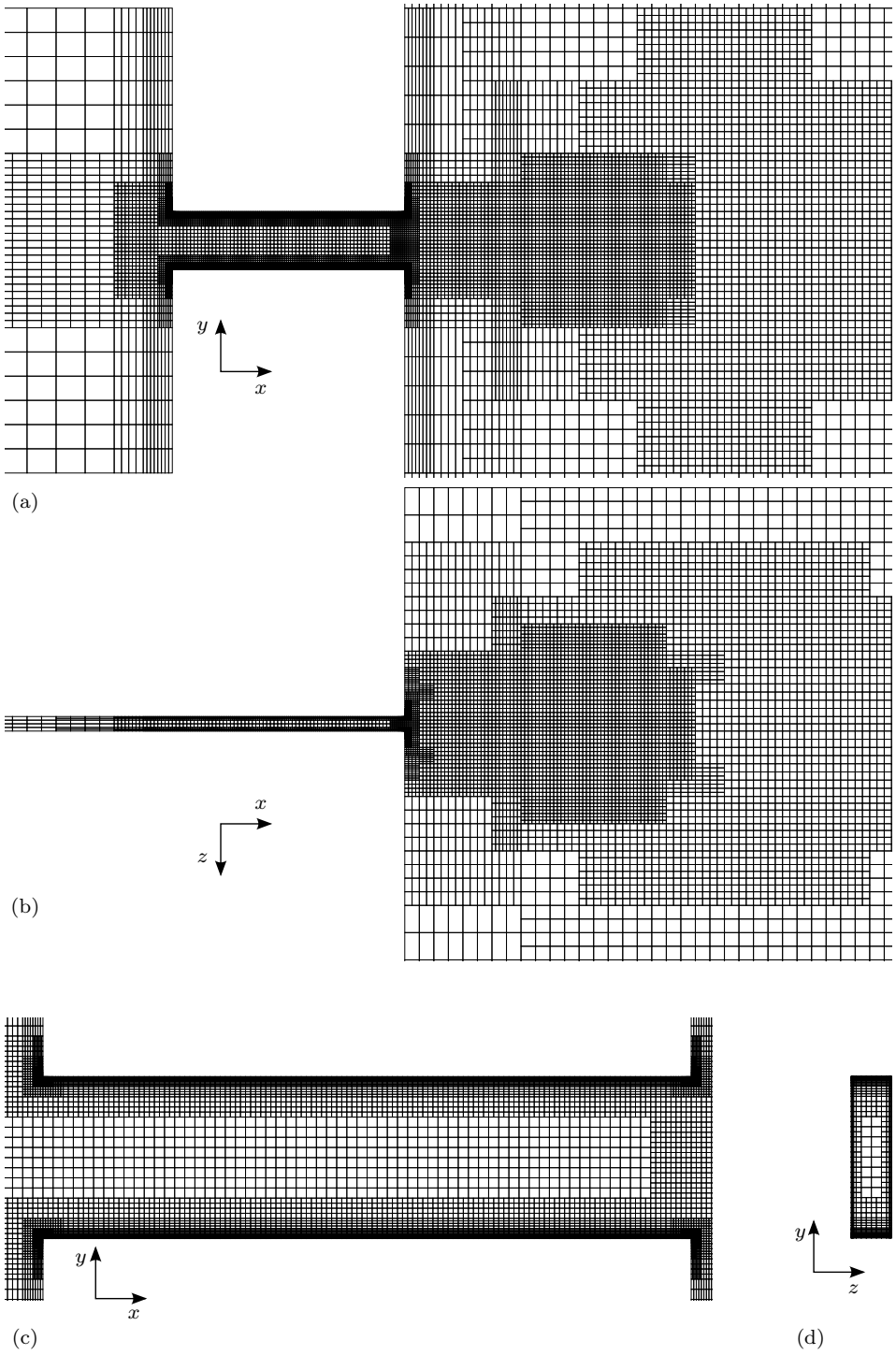

Figure 5.8: Computational grid of the full computational domain: (a) x-y view in the z symmetry plane; (b) x-z view in the y symmetry plane; (c) x-y view in the z symmetry plane of the nozzle region; (d) y-z view in the nozzle cross-section. Only every fourth grid line is shown.

Grid Sensitivity Study

To demonstrate the grid convergence behavior, we present simulation results for the developing cavitation number $\sigma = 0.78$. As discussed above, we apply 5 different grids, which range from a very coarse grid, three intermediate grids, to the final fine grid. We initiate our simulation on the coarse grid (level 1). We then interpolate the solution to the intermediate grids (level 2-4) and, finally, the fine grid (level 5) as soon as a steady behavior of the flow is found. Figure 5.9 shows the grid in the nozzle region (left column) along with instantaneous iso-surfaces of 10%-vapor-volume fraction (right column) for the coarse grid, Fig. 5.9(a/b), the intermediate level 2, Fig. 5.9(c/d), level 3, Fig. 5.9(e/f), and level 4, Fig. 5.9(g/h), grids, as well as the fine grid, Fig. 5.9(i/j). Additionally, Fig. 5.10 shows the time evolution of the global vapor volume fraction. Grid levels are marked with the corresponding numbers.

The level 1 grid is too coarse to predict regions of vapor productions, but is used to develop the mean flow field. Already on the level 2 grid, a converged flow behavior is found with respect to the global void fraction. Further refinement to level 3 and higher introduces a lower shedding frequency, but does not alter the mean value of the vapor volume fraction. Small scale vapor structures finally are already fully resolved on the level 3 grid.

These findings are also confirmed by the turbulence statistics. Figure 5.11 shows the mean and fluctuating velocity components for the level 3, level 4, and level 5 grids at different channel positions. We find a good agreement between all three levels.

5.2.2 Analysis of Cavitating Channel Flow

Cavitation Characteristics

We first compare our numerical results with the available experimental data for three operating points. Figure 5.12 shows transmitted light images of instantaneous vapor structures observed in the experiment (right column) in comparison with LES results for the depth-averaged instantaneous vapor volume fraction $\langle\alpha\rangle_z$ (middle column) and time- and depth-averaged vapor volume fraction $\langle\langle\alpha\rangle\rangle_z$ (right column).

For a high cavitation number, $\sigma = 1.27$, no cavitation is observed in the experiment, see Fig. 5.12(a). The LES simulation, Fig. 5.12(b-c), predicts a small amount of vapor to be generated in the shear layer at the nozzle inlet. In contrast to the nozzle geometry in the experiment, which is assumed to exhibit a small, but unspecified radius due to manufacturing and hydrodynamic erosion, the numerical grid prescribes a perfectly sharp edge that promotes rupture of the liquid.

For moderate cavitation numbers, $\sigma = 0.78$, cavitation is observed in the shear layer up to approximately 35% of the nozzle length, see Fig. 5.12(d-f). In the simulation, these sheets show a periodic shedding, which is induced by the re-entrant jet near the wall. Furthermore, smaller, cavitating vortices driven by the shear layer detach and are convected downstream, where they collapse under the higher surrounding pressure. After

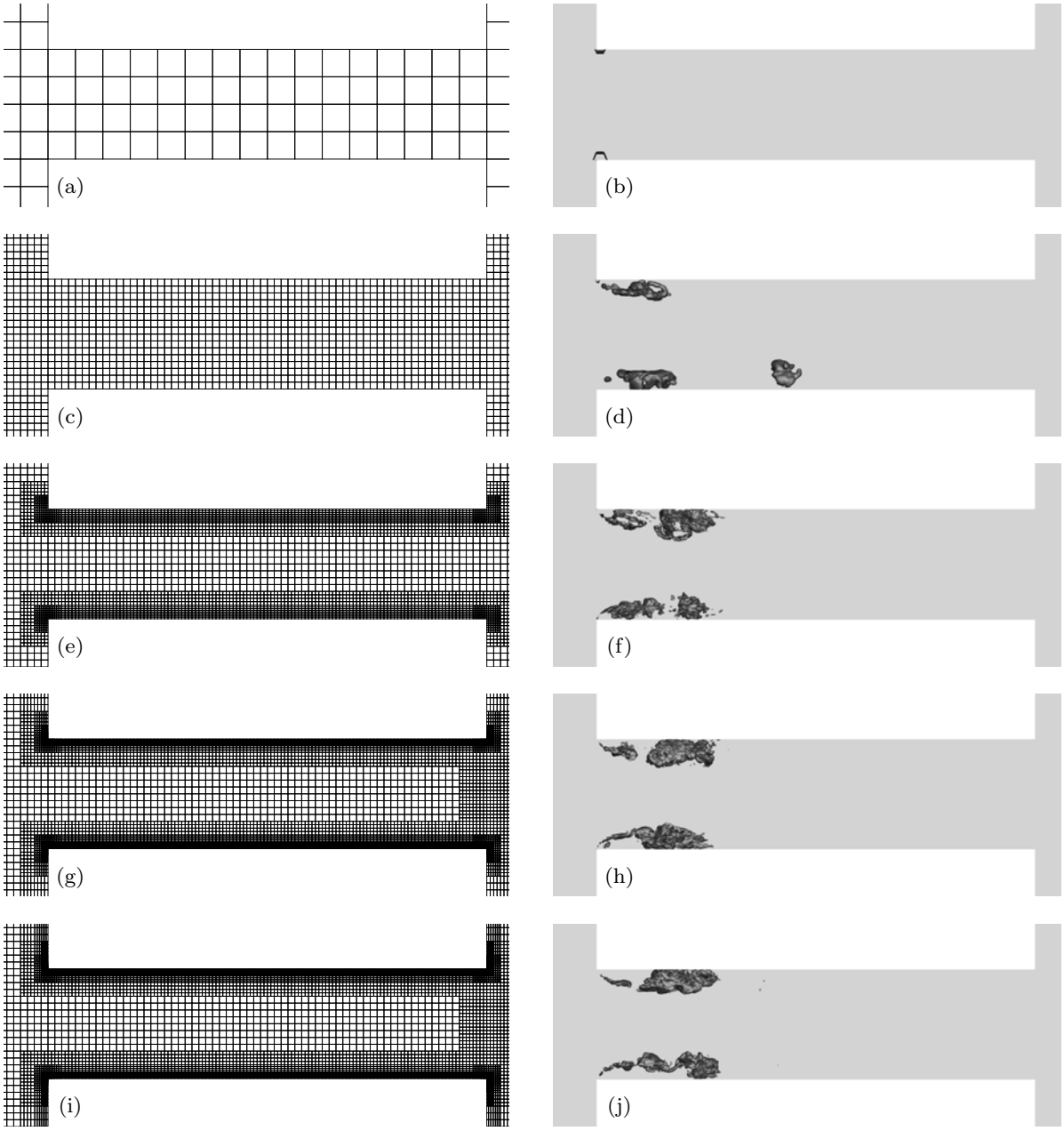

Figure 5.9: Computational mesh for all applied grid levels 1-5 (from top to bottom): x-y view of the mesh in the z symmetry plane (left column, only every fourth grid line is shown); instantaneous iso-surfaces of 10%-void fraction (right column).

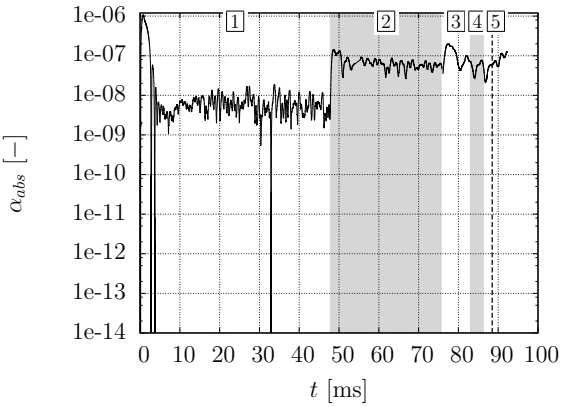

Figure 5.10: Temporal evolution of the global vapor volume fraction α_{abs} for $\sigma = 0.78$. Grid levels are marked with numbers; sampling on the finest grid is started at the position marked with a dashed line.

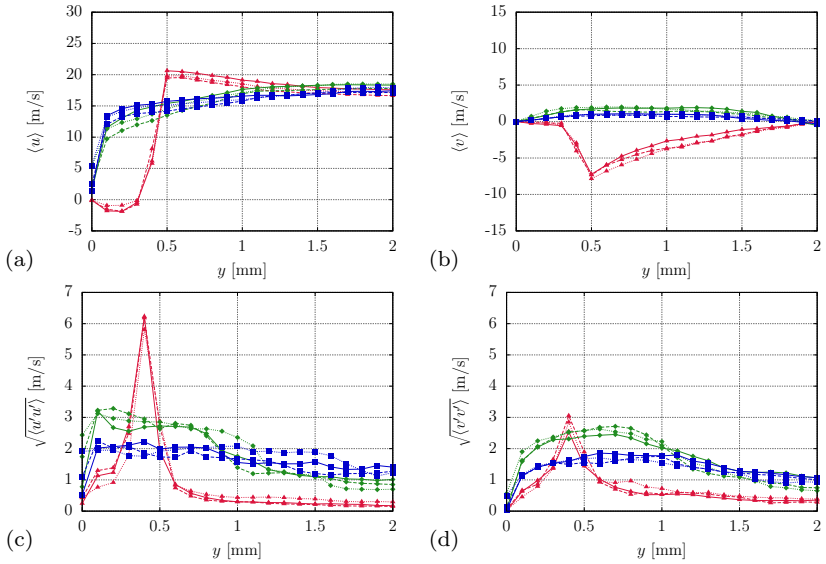

Figure 5.11: Grid convergence study: mean and fluctuating velocity components for $\sigma = 0.78$ at positions $x = 0.5$ mm (-△-), $x = 8.0$ mm (-◇-), and $x = 13.0$ mm (-□-) for grid level 3 ($\cdots$), grid level 4 (- - -), and grid level 5 (—).

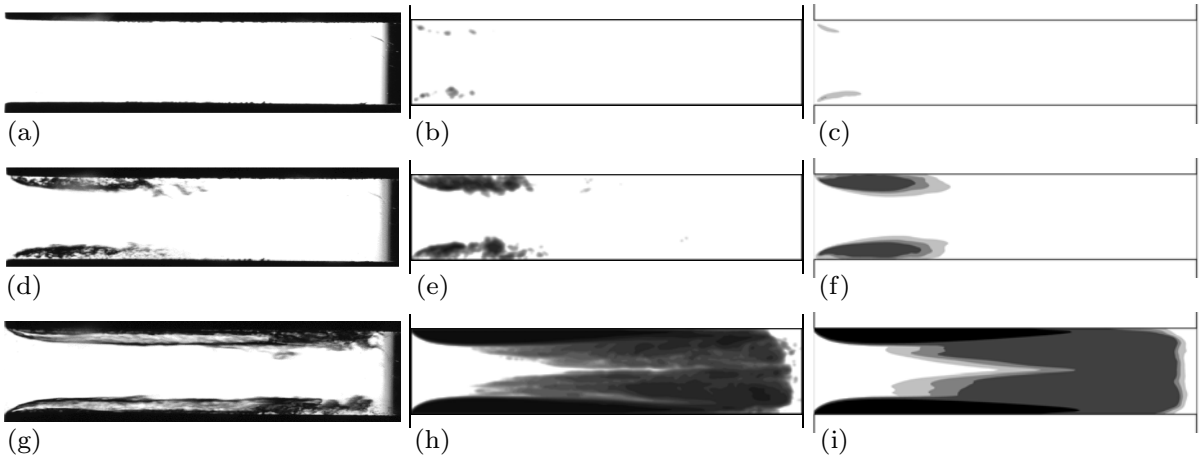

Figure 5.12: Side view of vapor structures inside the nozzle for $\sigma = 1.27$ (a-c), $\sigma = 0.78$ (d-f), and $\sigma = 0.65$ (g-i). Left column: instantaneous vapor structures observed in experiments [reprinted from A. Sou, S. Hosokawa, and A. Tomiyama, Int. J. Heat Mass Transfer 50, 3575 (2007) [174]. Copyright 2007, Elsevier]; middle column: contours of instantaneous, depth averaged vapor volume fraction $0.01 < \langle\alpha\rangle_z < 1.0$ in logarithmic scale; right column: contours of time and depth averaged vapor fraction $\langle\langle\alpha\rangle\rangle_z = \{0.01, 0.05, 0.1\}$.

very strong collapses a subsequent rebound and evaporation of liquid due to the induced expansion wave is observed in the LES.

The lowest cavitation number under investigation, $\sigma = 0.65$, is characterized by a super-cavitation state and forms a stable vapor sheet, which spans from the nozzle inlet to the outlet. In contrast to the experiments, Fig. 5.12(g), the LES predicts vapor regimes in the center of the nozzle starting at approximately 50% of the nozzle length, see Fig. 5.12(h-i). This can be attributed to large, cavitating vortical structures, which are discussed in detail below.

Based on the time and depth averaged vapor volume fraction, we determine the non

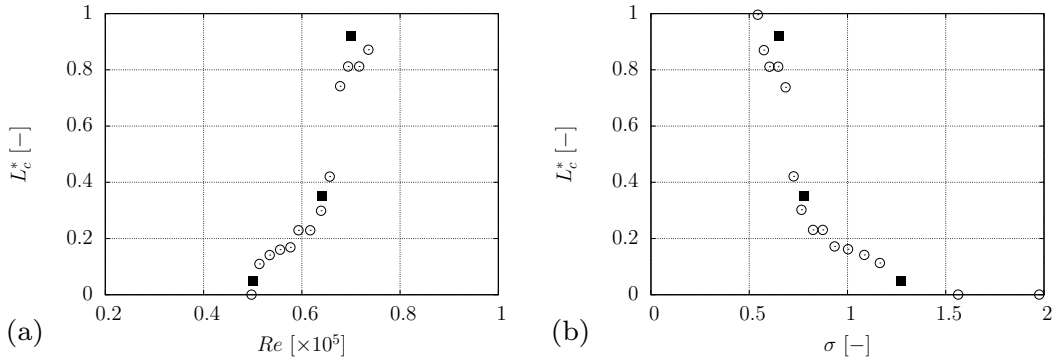

Figure 5.13: Non dimensional cavitation length L_c^* vs, Reynolds number Re (a) and cavitation number σ (b) from LES simulation (■) and experiments [174] (○).

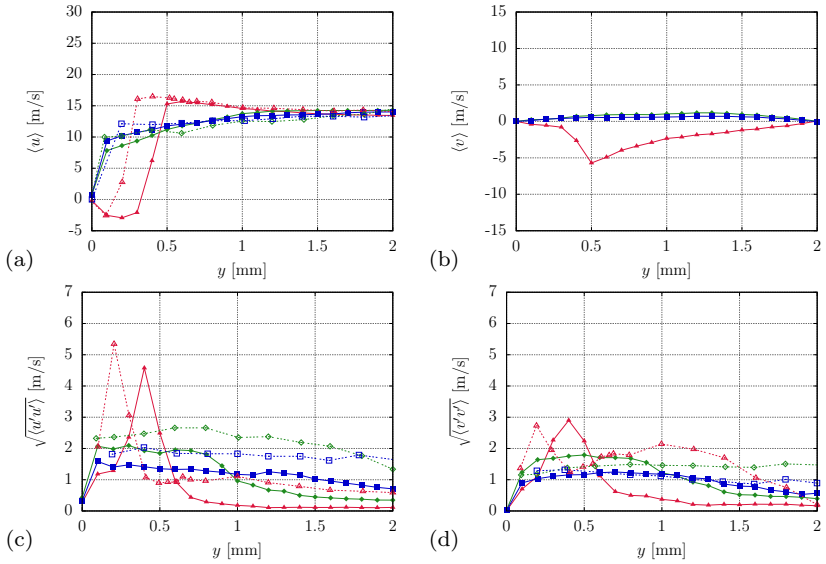

Figure 5.14: First operating point $\sigma = 1.27$: Mean and fluctuating velocity components at positions $x = 0.5$ mm (-△-), $x = 8.0$ mm (-◇-), and $x = 13.0$ mm (-□-); filled symbols / solid lines represent simulation results, empty symbols / dashed lines are experimental results [174, 175].

dimensional cavitation length L_c^*, which we define as the maximum stream-wise extent of the 5%-iso-contour of the time- and depth-averaged void fraction with respect to the nozzle length. Figure 5.13 shows L_c^* as a function of the Reynolds number (a) and of the cavitation number (b), together with corresponding experimental data. Our results are in very good agreement with the experiments by Sou *et al.* [174].

Velocity Fluctuations

A quantitative comparison with LDV measurements, where available, is given in Figs. 5.14-5.16. The plots show x and y components of mean velocities $\langle u \rangle$ and $\langle v \rangle$, and velocity fluctuations u' and v' on the z-symmetry plane over the half-width of the duct, where $y = 0$ corresponds to the nozzle wall and $y = 2$ mm to the centerline.

For a cavitation number of $\sigma = 1.27$, see Fig. 5.14, mean streamwise velocity components show excellent agreement between LES and experiment. An analysis of the velocity fluctuations reveals a significantly lower turbulence intensity, in particular in the v' component, at the centerline of the incoming flow at $x = 0.5$ mm, see Fig. 5.14(c-d). The high level of turbulence in the experimental data is assumed to be due to disturbances induced by the plunger pump system and by flow deflections and throttles upstream of the point of interest. Such effects cannot be accounted for in the LES. This is further elaborated in Sec. 5.2.2, where effects of the inflow boundary conditions are excluded as a cause for this disagreement between simulation and experiment. Towards the nozzle outlet the deviation of the velocity fluctuations in the core flow become smaller. At the edge of the shear layer, which is slightly wider in the LES, both simulation and experiment show peak values of the stream-wise turbulence intensity of approx. 30%.

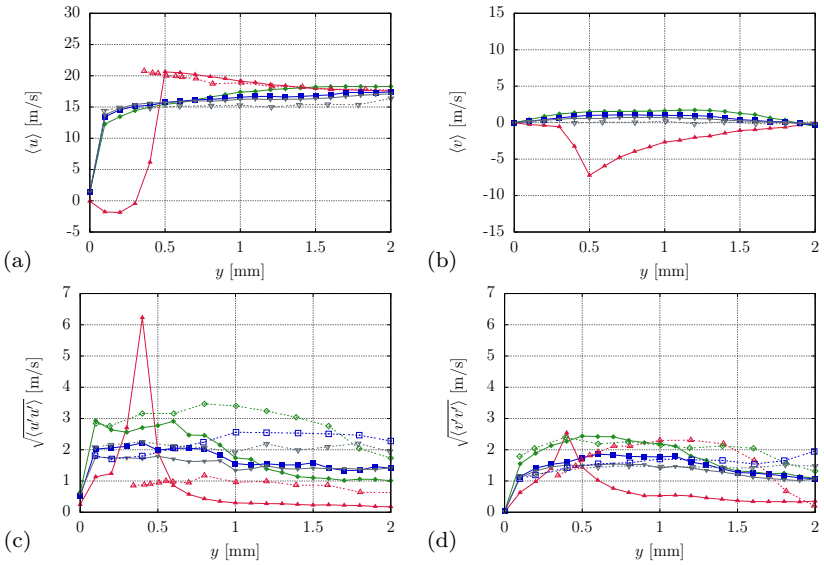

Figure 5.15: Second operating point $\sigma = 0.78$: Mean and fluctuating velocity components at positions $x = 0.5$ mm (-△-), $x = 8.83$ mm (-◇-), $x = 13.0$ mm (-□-), and $x = 15.0$ mm (-▽-); filled symbols / solid lines represent simulation results, empty symbols / dashed lines are experimental results [174, 175].

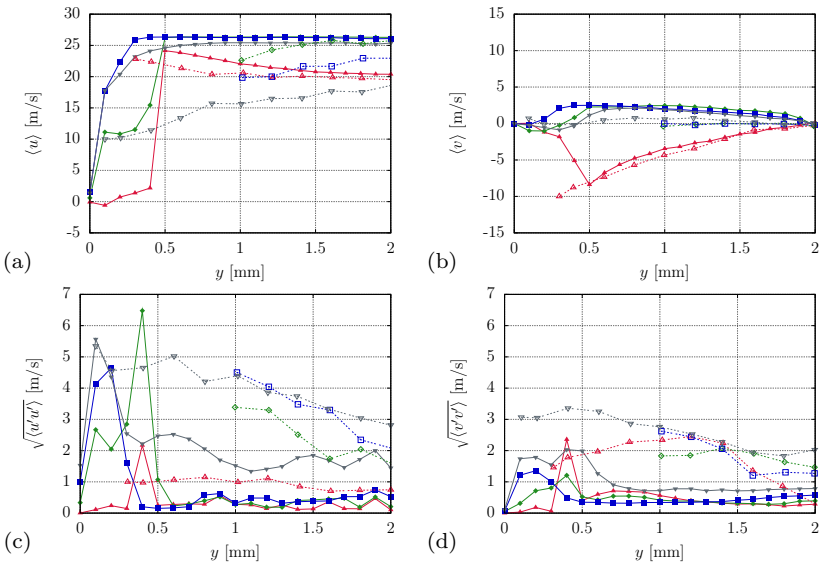

Figure 5.16: Third operating point $\sigma = 0.65$: Mean and fluctuating velocity components at positions $x = 0.5$ mm (-△-), $x = 8.0$ mm (-◇-), $x = 13.0$ mm (-□-), and $x = 15.0$ mm (-▽-); filled symbols / solid lines represent simulation results, empty symbols / dashed lines are experimental results [174, 175].

A good agreement is also found for a smaller cavitation number of $\sigma = 0.78$, see Fig. 5.15. Again, the level of turbulent fluctuations is underestimated at the inlet, but tends towards the experimental values in near-wall regions at the nozzle outlet, Fig. 5.15(c-d). LDV measurements in vapor regions are not possible. Hence, only the LES reveals the peak in the fluctuation quantities at the edge of the cavitating shear layer at $x = 0.5$ mm, and the back-flow region with values of negative stream-wise velocity in the range of 1.7 mm $< y <$ 2.0 mm inside the detached vapor sheet.

The results for a cavitation number of $\sigma = 0.65$ are shown in Fig. 5.15. In this case, the LES predicts larger water-vapor regions than the experiment in the downstream half section of the duct. Due to the smaller effective nozzle cross-section, this leads to a higher mean stream-wise velocity than measured in the experiment. The deviation of the mean velocity $\langle v \rangle$ in the range $0.3 < y < 0.5$ can likely be accredited to the slightly thicker boundary layer at this position due to the perfectly sharp inlet edge in the LES grid. Additionally, the vapor regions damp velocity fluctuations, see, e.g., Duke *et al.* [40] and Egerer *et al.* [48, 49]. Only after $x = 15$ mm a strong rise in turbulence intensity is observed when compared to velocity profiles located upstream of this position. This turbulence amplification is caused by collapse events at the end of the cavitation region and is further discussed below.

In summary, both a qualitative comparison in terms of position and size of vapor regions as well as a quantitative analysis of velocity fluctuations show good and reasonable, respectively, agreement between experiment and LES. For small cavitation numbers, the vapor regions are larger in the simulation, which causes damping of fluctuation quantities.

Discussion of the Inlet Boundary Condition

In the following, we discuss the lower level of turbulent fluctuations in the numerically predicted incoming flow field compared to the measurements of Sou *et al.* [174, 175]. Figure 5.17 summarizes the flow conditions at the nozzle inlet at $x = 0.5$ mm for all investigated cavitation numbers. The mean streamwise flow velocity shows a very good agreement between simulation and experimental data. In contrast, the core flow, which at this position is not affected by the growing boundary layer at the wall, contains a significantly lower level of velocity fluctuations in the LES. Especially the v' fluctuations are considerably larger in the experiment.

To quantify effects of boundary conditions in the inflow section, we conducted a simulation of the $\sigma = 0.78$ configuration including a periodic precursor simulation, as sketched in Fig. 5.18. The length of the precursor domain is $\Delta x = 0.01$ m. A forcing term is applied on the periodic precursor to maintain an average bulk velocity $u_{b,\sigma=0.78} = 2.0$ m/s. The instantaneous velocity field is then mapped onto the inlet boundary of the nozzle domain.

Fig. 5.19 shows the velocity components at the duct inlet for the experiment, for the LES with a prescribed laminar profile, and for the LES with precursor simulation. Very little difference is observed between the two simulation results. The thickness of the shear layer and the level of streamwise velocity fluctuations are essentially unaltered. v' fluctuation

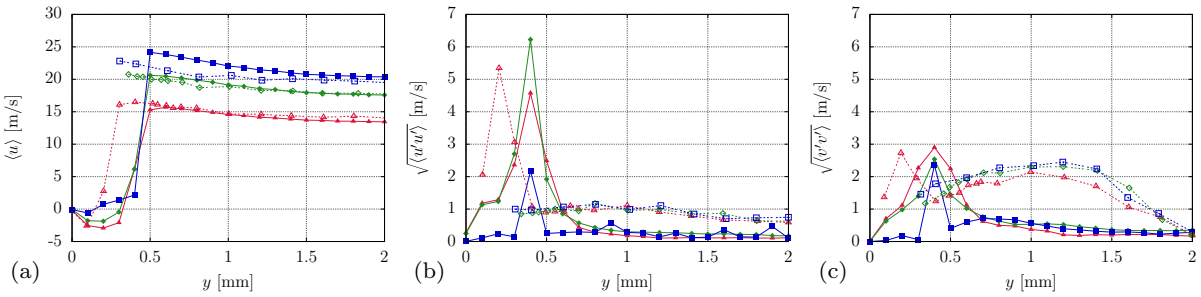

Figure 5.17: Mean and fluctuating velocity components at the nozzle inlet ($x = 0.5$ mm) for $\sigma = 1.27$ (-△-), $\sigma = 0.78$ (-◇-), and $\sigma = 0.65$ (-□-); filled symbols / solid lines represent simulation results, empty symbols / dashed lines are experimental results by Sou *et al.* [174, 175].

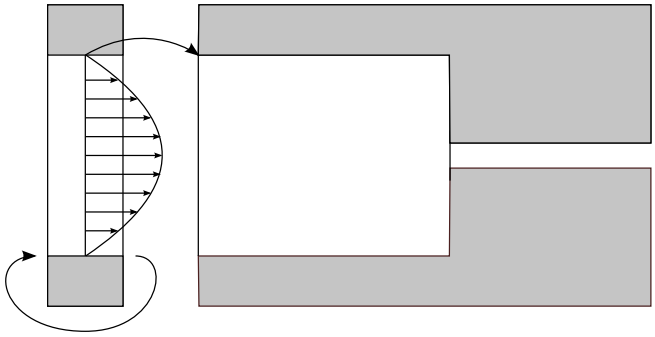

Figure 5.18: Schematic of the mapping strategy in the nozzle LES with precursor simulation.

components are slightly increased with a precursor simulation, but follow the trend of the results obtained without a precursor and with a prescribed laminar profile.

We therefore believe that the high level of turbulence intensity does not originate from grid underresolution of an otherwise turbulent nozzle flow. Note that the Reynolds number Re_τ based on the friction velocity and the boundary layer thickness of the nozzle flow is on the order of $Re_\tau \sim 100$. A more likely cause are disturbances induced by the pumping system, and by flow deflections and throttles and pipes connecting the nozzle domain with the experimental apparatus. These uncertainties cannot be accounted for in the LES without additional evaluation of the entire upstream flow.

Assessment of the Three-Dimensional Cavitating Nozzle Flow

In the following we analyze the three-dimensional flow field inside the nozzle. Figure 5.20 shows snapshots of iso-surfaces of coherent vortical structures visualized by the λ_2 criterion [91], together with cavitation regions and wall pressure.

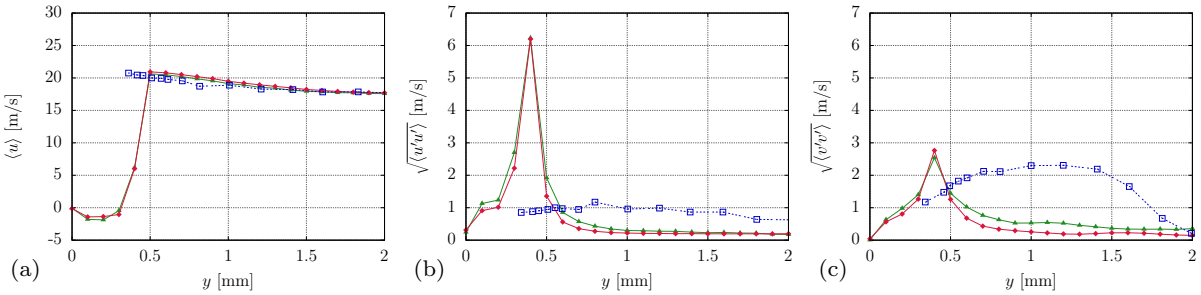

Figure 5.19: Mean and fluctuating velocity components at the nozzle inlet ($x = 0.5\ mm$) for $\sigma = 0.78$ with laminar inflow profile (-△-), fully developed inflow from precursor simulation (-◇-), and experiment (-□-); filled symbols / solid lines represent simulation results, empty symbols / dashed lines are experimental results by Sou *et al.* [174, 175].

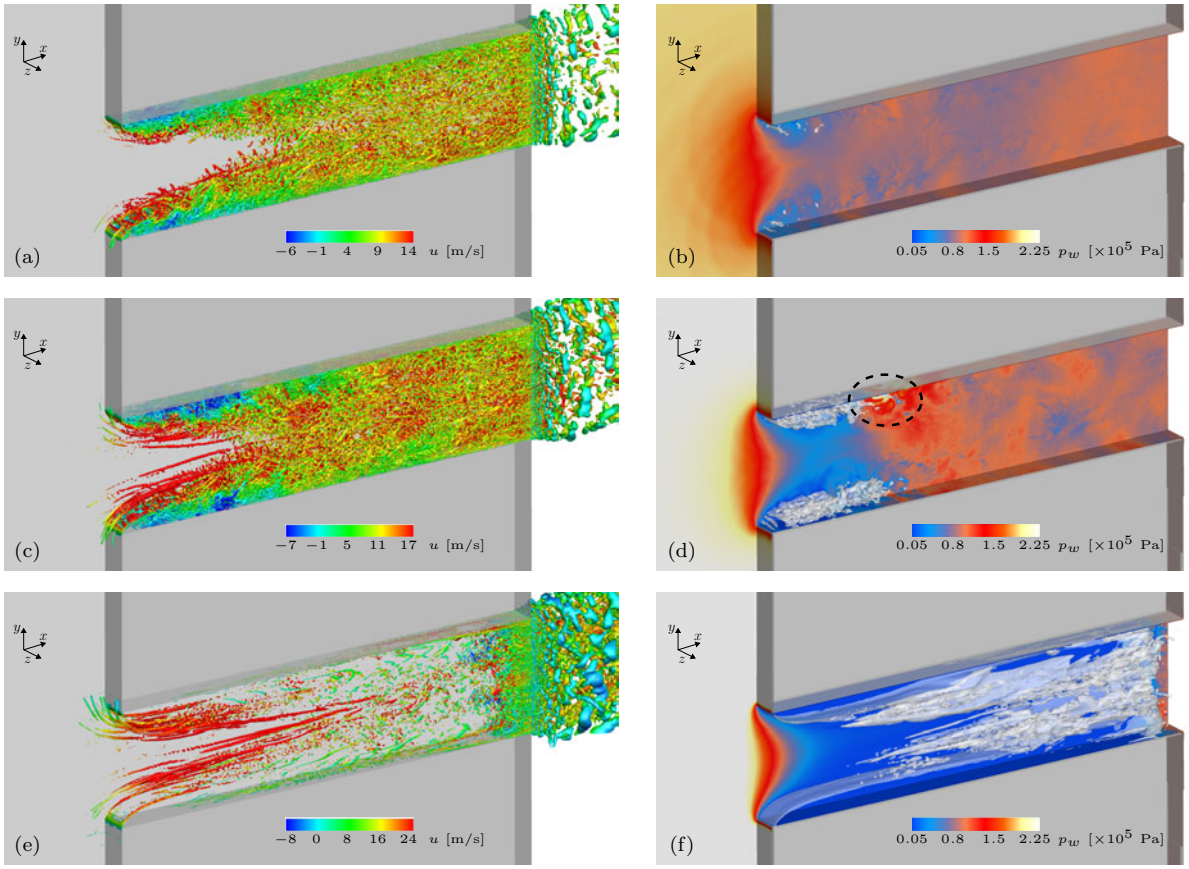

Figure 5.20: Snapshot of iso-surfaces of $\lambda_2 = -1 \times 10^8\ 1/s^2$ colored by streamwise velocity u (left column) together with iso-surfaces of vapor volume fraction $\alpha = 0.1$ and wall pressure (right column) for $\sigma = 1.27$, $\sigma = 0.78$, and $\sigma = 0.65$ (from top to bottom). Black dashed marker shows an example for the wall pressure near a collapse event.

For cavitation number $\sigma = 1.27$, see Fig. 5.20(a-b), a transitional and eventually fully turbulent duct flow is recovered. Corner vortices, which originate from the boundary layers upstream of the nozzle, are stretched in stream-wise direction and quickly break up into small scale turbulence. This phenomenon has been studied extensively by Egerer *et al.* [48].

The highly unsteady shedding and collapse of cavitation structures in case of a cavitation number $\sigma = 0.78$, Fig. 5.20(c-d), amplify turbulent fluctuations in the detached recirculation zone, which is identified by negative streamwise velocity. As a result, a fully turbulent flow is achieved earlier than in the non-cavitating case. The highly unsteady character of the flow at this operating point can also be noticed in the highly fluctuating wall pressure field, see Fig. 5.20(d), which shows the imprint of previously collapsed vapor clouds. Near the top wall of the nozzle such a collapse event is captured in the snapshot (see marked position).

Results for a cavitation number of $\sigma = 0.65$, Fig. 5.20(e-f), significantly differ from the higher cavitation numbers in terms of turbulent fluctuations and cavitation characteristics. For this operating point, stable corner vortices stretch up to approximately 60% of the nozzle length. These vortices start to cavitate at approximately 30% of the nozzle length, and add to the stable cavitation sheet at the wall, which forms at the inlet edge. This observation is consistent with the work of Egerer *et al.* [48], who found a similar, even more pronounced, behavior of cavitating corner vortices in their studies of cavitating micro-channels in agreement with reference experiments for a cavitation liquid throttle flow exiting into liquid. It is possible that these vortical structures become unstable in the experiment and break up due to the high level of turbulence, which would prevent the formation of stable vortex cavitation, or that geometrical uncertainties, which are not quantified in the description of the experimental setup, affect the nominal parameters at the low cavitation number case. Turbulent fluctuations are damped inside the vapor region and are strongly amplified at the nozzle outlet. This is in agreement with the findings of Dittakavi *et al.* [35].

5.2.3 Effect of Cavitating Nozzle Flow on Jet Break-Up

We now discuss the effect of the cavitating nozzle flow onto the liquid jet. Snapshots of our LES data are put side by side with experimental images in Fig. 5.21. The jet in the simulation is visualized by a 99%-volume fraction of air. Data are extracted for a range of 16×10^{-3} m $< x < 32 \times 10^{-3}$ m to match the image selection shown by Sou *et al.* [174, 175].

The experimental images show a very similar jet structure for cavitation numbers $\sigma = 1.27$ and $\sigma = 0.78$, see Fig. 5.21(a/d). For $\sigma = 0.65$, Fig. 5.21(g), in contrast, spray formation is observed. Small droplets and ligaments of liquid detach from the surface and cause an increased jet angle.

Our numerical results, see Fig. 5.21(b/e/h), show only little effect of the cavitation number on the average jet angle in the x-y plane. Rather than spray formation, we observe only a slightly more disturbed jet surface structure at the lowest cavitation number. However,

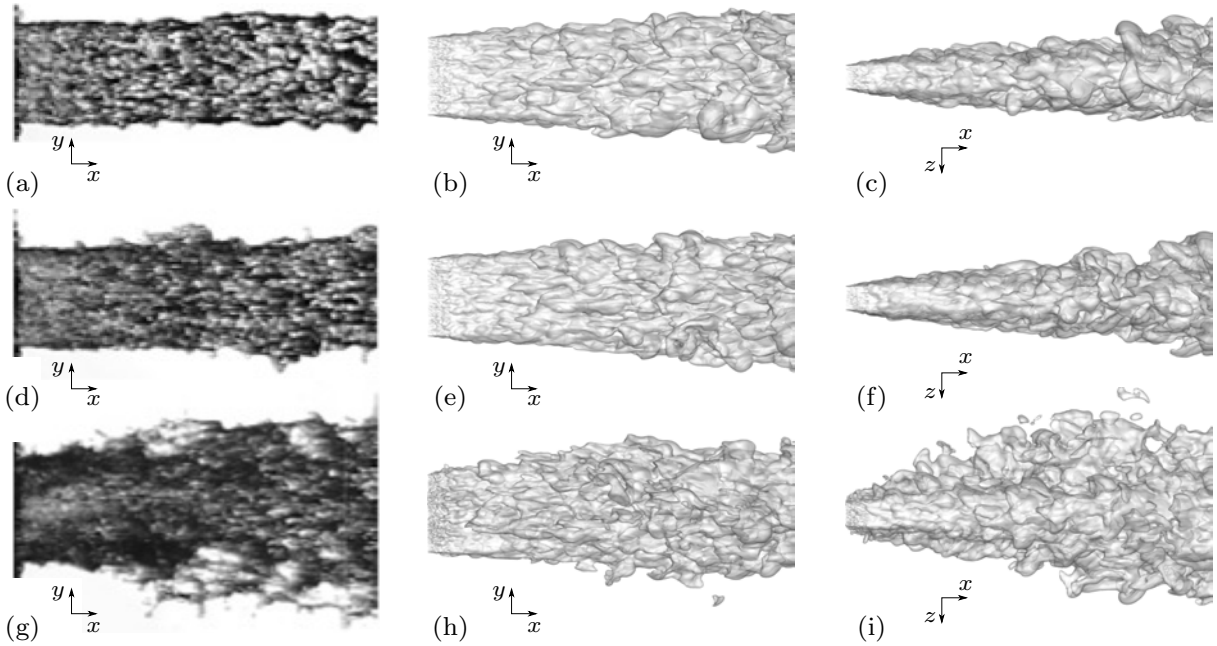

Figure 5.21: Experimental transmitted light images (left column) [reprinted from A. Sou, S. Hosokawa, and A. Tomiyama, Int. J. Heat Mass Transfer 50, 3575 (2007) [174]. Copyright 2007, Elsevier] and LES snapshots of x-y view (middle column) and x-z view (right column) showing iso-surfaces of gas volume fraction $\beta_G = 0.99$ in the range 16 mm $< x <$ 32 mm for $\sigma = 1.27$, $\sigma = 0.78$, and $\sigma = 0.65$ (from top to bottom).

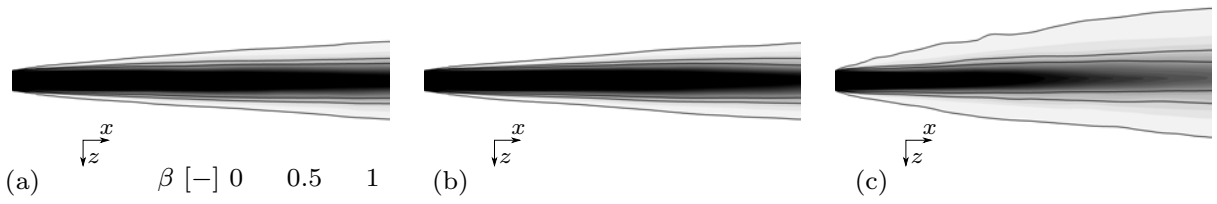

Figure 5.22: Time-averaged gas volume fraction β_G on the y-symmetry plane in the range 16 mm $< x <$ 32 mm for $\sigma = 1.27$, $\sigma = 0.78$, and $\sigma = 0.65$ (from left to right). Black lines show contour levels of $\beta_G = \{0.8, 0.9, 0.99\}$.

significant differences between the higher cavitation numbers $\sigma = 1.27$ and $\sigma = 0.78$, and the low cavitation number $\sigma = 0.65$ are observed in the x-z plane, see Fig. 5.21(c/f/i). We clearly notice a widening of the jet and a detachment of large and few small liquid structures from its surface, which closely resembles the observations in the experiments of Sou *et al.* [174, 175]. This effect of the cavitation number on the jet spreading angle is more clearly visible in the time-averaged data, see Fig. 5.22.

The primary break-up of a liquid jet, which is driven by inertia, can be divided into two stages. Initial perturbations of the jet surface are triggered near the nozzle exit. These perturbations are amplified in the liquid-gas shear layer under the influence of aerodynamic forces, resulting in secondary jet break-up in which the formation of droplets and ligaments dominate. For the initial stage, momentum generation towards the liquid-gas interface is of main importance. In addition to initial disturbance of the liquid-air interface due to Kelvin-Helmholtz type instabilities, we identify three main mechanisms from an analysis of our simulation data that lead to distortions of the jet surface and hence to a widening and break-up of the jet: turbulence production in terms of velocity fluctuations inside the nozzle near the outlet region, entrainment of non-condensable free gas, which enters the nozzle region from the outlet volume, and collapse events inside the emerging liquid jet. In the following, each of these mechanisms is briefly discussed.

Kelvin-Helmholtz Instabilities

Liquid jet and gas phase form a shear layer at the interface in the outflow region, which quickly becomes unstable to small disturbances and forms large-scale Kelvin-Helmholtz (KH) vortical structures, as has been discussed extensively in the literature [102, 111, 192]. These formations grow until the aerodynamic forces due to the velocity difference with respect to the quiescent surrounding gas break off large structures, which eventually lead to Rayleigh break-up and droplet formation[33]. In Fig. 5.23, KH vortical structures are visualized by contours of the z-vorticity magnitude ω_z in the xy-symmetry plane (top row), and of the y-vorticity magnitude ω_y in the xz-symmetry plane. The jet surface is highlighted by an iso-line of gas volume fraction $\beta_G = 0.99$.

For the two higher cavitation numners, $\sigma = 1.27$ and $\sigma = 0.78$, only low values of vorticity production are found at the liquid gas interface. For a low cavitation number, $\sigma = 0.65$, large KH vortices are clearly visible, which detach from the jet.

Effect of Turbulent Fluctuations

Sou *et al.* [174, 175] argue that strong turbulent fluctuations induced by collapses of vapor regimes just upstream of the nozzle exit induce additional momentum towards the liquid-gas interface and hence may cause the increase in spray angle and, ultimately, jet atomization observed in their experiments.

The collapse of single bubbles and bubble clouds interacts with the surrounding flow field on multiple scales. Dabiri *et al.* [26] observe that vorticity is generated at the surface of a single bubble in a shear flow during collapse, which could add to larger vortical structures

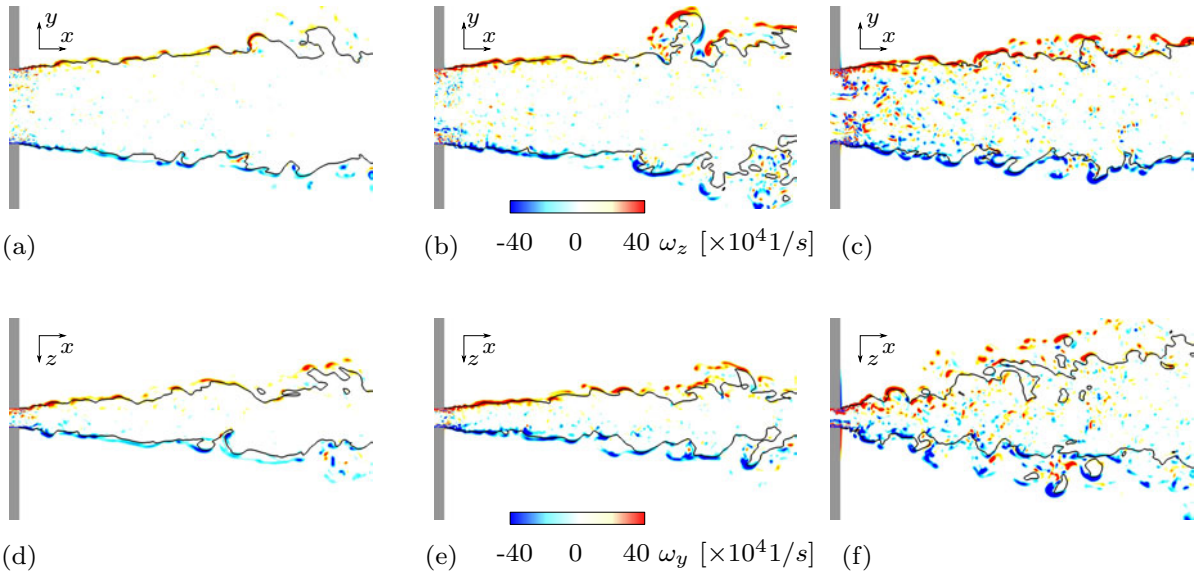

Figure 5.23: Contours of z-vorticity magnitude ω_z in the xy-symmetry plane (top row), and y-vorticity magnitude ω_y in the xz-symmetry plane (bottom row) together with iso-contour for gas volume fraction $\beta_G = 0.99$ (black line) for $\sigma = 1.27$, $\sigma = 0.78$, and $\sigma = 0.65$ (from left to right).

in the liquid. This effect, however, cannot be resolved in our LES. We suspect that the observed increase of the small scale fluctuations on the turbulence level are caused by micro jetting during the collapse process of aspherical vapor structures and vapor clouds, which creates a strong increase of local kinetic energy, see Adams and Schmidt [2]. Dittakavi *et al.* [35] moreover found that the collapse of vapor structures causes a substantial increase in the baroclinic torque. In addition, turbulent fluctuations are amplified when processed by shock waves, see, e.g. Larsson *et al.* [101] and Hickel *et al.* [82] In a cavitating cloud collapse, this effect can be intensified by chain reactions of collapsing cavity arrays, as found by Lauer *et al.* [103].

Figure 5.24 shows the wall-normal velocity fluctuations in y- and z-direction at the outlet extracted from our simulations. In the LES, only a small increase in wall-normal velocity fluctuations, Fig. 5.24(a), is detected in the proximity of the top wall near the nozzle exit when comparing $\sigma = 0.78$ with $\sigma = 0.65$. In contrast, in z-direction, see Fig. 5.24(b), a significant increase in the w' fluctuation magnitude is found for the supercavitating nozzle with $\sigma = 0.65$. The maximum amplitude of the w' fluctuations for $\sigma = 0.65$ is approx. 2.5 times higher than for $\sigma = 0.78$.

In our numerical simulation we detect collapse events with an algorithm developed by Mihatsch *et al.* [120, 121], which considers the re-condensation of vapor volume content inside a computational cell together with an analysis of the local velocity divergence. The normalized peak collapse pressure p_c is obtained by scaling the observed maximum p_m

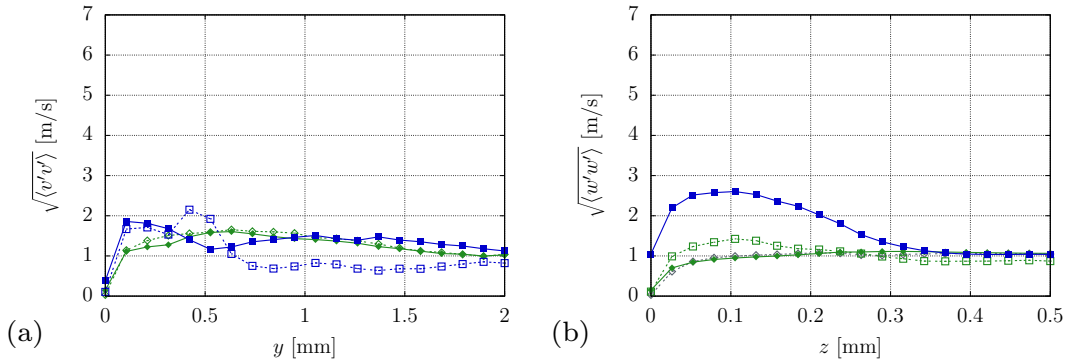

Figure 5.24: Components of wall-normal velocity fluctuations in y- and z-direction at the nozzle outlet at $x = 15.0$ mm (empty symbols / dashed lines) and $x = 16.0$ mm (filled symbols / solid lines) for $\sigma = 0.78$ (-◇-) and $\sigma = 0.65$ (-□-)

following Schmidt *et al.* [161] by

$$p_c = p_m \frac{V_\Omega^{1/3}}{l_{ref}}, \tag{5.7}$$

where we set the reference length scale $l_{ref} = 3.75 \times 10^{-6}$ m to compensate for the effect of grid resolution onto the collapse pressure inside the cell with volume V_Ω. Figure 5.25 shows the position of detected collapse events during a time interval of $\Delta t = 2$ ms. Each event is represented by a sphere, whose size and color scales with normalized collapse pressure p_c. In case of $\sigma = 1.27$, see Fig. 5.25(a-c), only few weak events are detected near the nozzle inlet. For $\sigma = 0.78$, Fig. 5.25(d-f), the location of collapse events is restricted approximately to the first 30% of the duct near the upper and lower walls. Only few collapses, which are mainly caused by rebounding vapor bubbles, are detected downstream of this region. In the supercavitating case, $\sigma = 0.65$, the majority of collapse events is detected near the nozzle outlet, see Fig. 5.25(g-i). In addition to events at the upper and lower duct wall at approximately 90% of the nozzle length, strong events are recorded in the LES at the side walls directly at the outlet edge. The events in this region are caused by the collapse of vapor structures near the side walls predicted in our LES, which are not present in the experiment. The position of the collapse events coincides with the location of amplification of turbulent fluctuations, which confirms the hypothesis of Sou *et al.* [174, 175].

Effect of Gas Entrainment

Gas entrainment into the nozzle is found to introduce large disturbances to the jet, which leads to an increase of the average jet angle. Low pressure vapor regions, which are present just upstream of the nozzle outlet and extend to the exit at the side-walls, cause a pressure gradient directed from the nozzle into the gas filled plenum. The initial phase of the collapse process of a cavitation region furthermore causes an acceleration of surrounding fluid towards the center of the structure. Near the nozzle outlet, such events cause gas to enter the duct region.

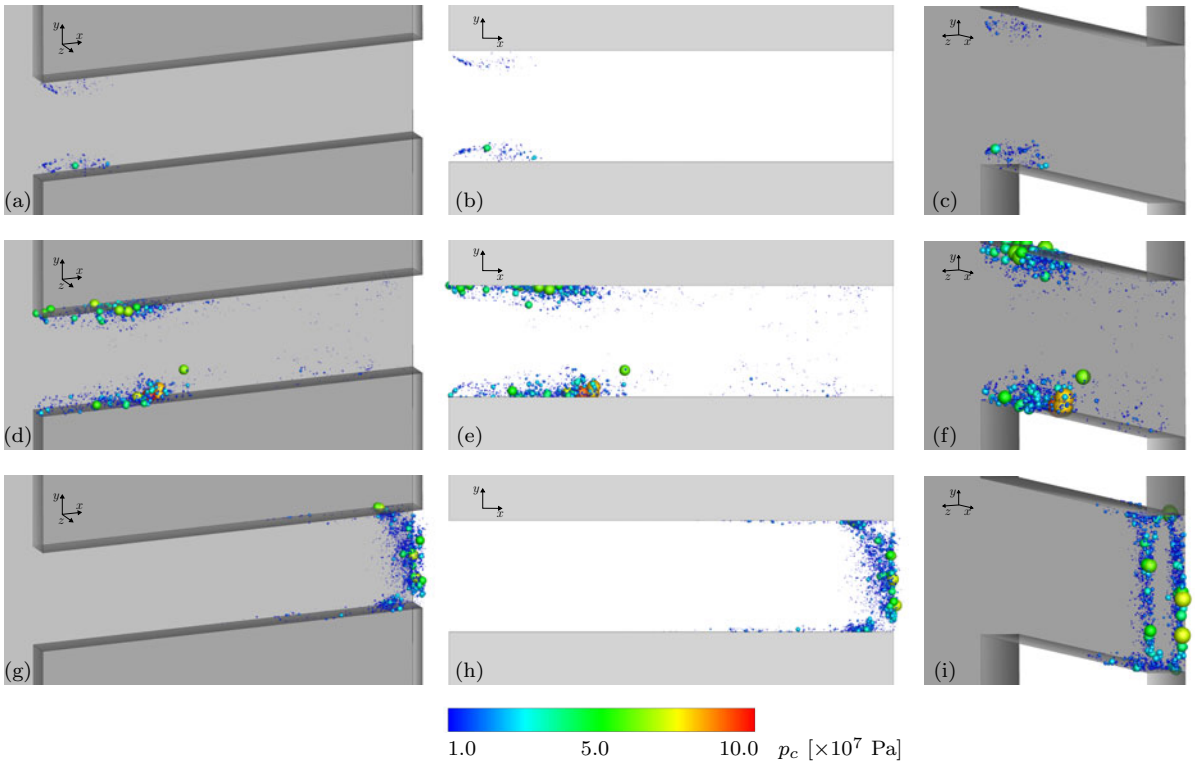

Figure 5.25: Spatial distribution of isolated collapses detected during an analysis interval of $\Delta t = 2$ ms for $\sigma = 1.27$, $\sigma = 0.78$, and $\sigma = 0.65$ (from top to bottom). Size and color of each sphere is based on the normalized collapse pressure p_c. Collapse events with a collapse pressure $p_c < 30 \times 10^5$ Pa are not shown.

This mechanism is depicted as a series of snapshots in Fig. 5.26. Gas that has passed the exit plane in upstream direction is visualized though green iso-surfaces of $\beta_G = 0.1$. At time $t = t_0$, Fig. 5.26(a), a large vapor structure reaches the nozzle outlet. As soon as the large structure collapses, gas is sucked into the nozzle, see Fig. 5.26(b). When the gas is pushed back by the liquid, Fig. 5.26(c), a significant acceleration of water in z-direction is observed, which results in a larger angle of the jet at the outlet. Few instants later in time, see Fig. 5.26(d/e), the same process is observed in the upper nozzle region.

Effect of Collapse Events inside the Jet

An potential additional mechanism promoting jet break-up is suspected in the collapse of vapor bubbles near a liquid-gas interface. This phenomenon was, e.g., discussed by Robinson *et al.* [152] and Obreschkow *et al.* [127], who describe the interaction of collapsing cavitation bubbles with a free planar and curved surfaces. The authors demonstrate that a bubble collapse near a liquid-gas interface creates a primary liquid jet pointing away from the interface, and a secondary jet towards the interface. The latter causes a liquid jet emerging from the surface. The intensity of this mechanism depends on the size of the cavitation bubble and its distance from the interface.

To demonstrate the ability of our model to represent this phenomenon, we have conducted a simple simulation to investigate this mechanism, as shown in Fig. 5.27. We initialize the domain with a liquid-gas interface at $p = 1$ atm and place a vapor bubble with $\alpha_v = 99\%$ inside the liquid. The bubble has a diameter of $D = 0.2$ mm and is resolved with approx. 16 cells across the bubble diameter on a homogenous grid. We vary the distance d between the bubble center and the interface, see Fig 5.27(a).

Snapshots show iso-surfaces of vapor volume fraction, gas volume fraction, and liquid mass fraction (right half of figures) together with contour-line $\beta_G = 0.99$ on the symmetry plane (left half of figures). The liquid-gas interface is colored by interface-normal velocity w. The bubble collapses under the high surrounding pressure, which is shown as a time series in Fig. 5.27(b-d). As soon as the bubble has collapsed, Fig. 5.27(c), which causes the liquid-gas interface to contract towards the collapse center, the formation of two jets is visible. The primary jet is directed away from the liquid-gas interface. The secondary jet, as found by experimental studies, points towards the interface and causes a small jet filled with water to be ejected into the gas domain, Fig. 5.27(c). The intensity of this jet, as well as inherent time scales, depend on the initial bubble diameter and its distance from the interface. The simplified study shows that effect of the secondary liquid jet penetrating the interface can be captured without surface tension in the early stages, before the formation of droplets and ligaments dominates the process, which cannot be captured by our current model.

A similar phenomenon, which we suspect to be based on the mechanism of a single bubble collapse near a liquid-gas interface as discussed above, is observed when cavitation regions pass the nozzle outlet and collapse inside the liquid jet near the liquid-gas interface. A confirmation of the occurrence of collapse events beyond the nozzle exit plane ($x > 16$ mm) in case of a supercavitating flow is found in Fig. 5.25(h). A time series of what we suspect to be the footprint of a vapor collapse near the jet surface is presented in Fig. 5.28.

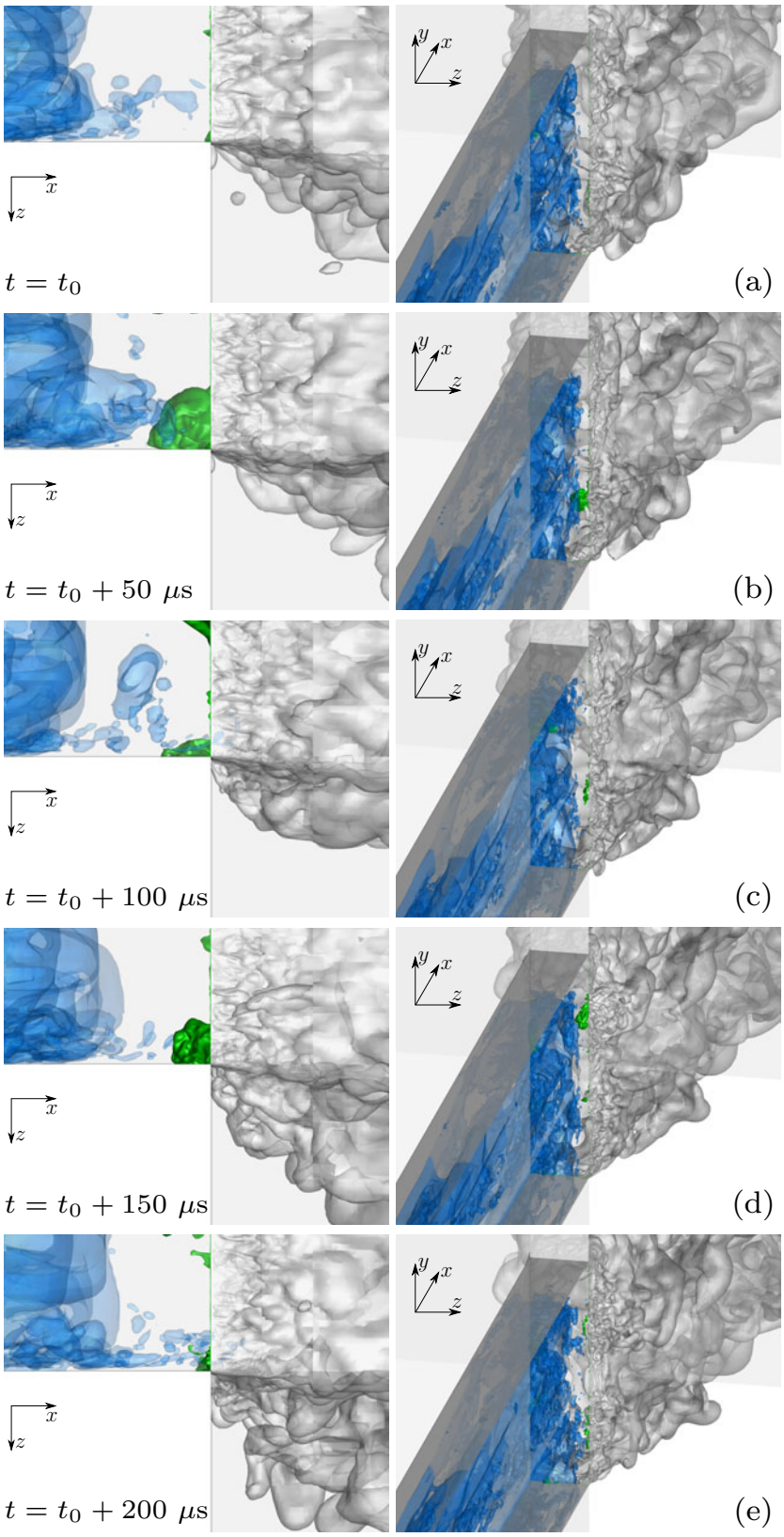

Figure 5.26: Visualization of gas entrainment process into the nozzle (left column: top view; right column: perspective view). Snapshots show iso-surfaces of $\alpha = 0.1$ (blue), together with gas volume fraction $\beta_G = 0.99$ (gray) and entrained gas volume fraction $\beta_G = 0.1$ (green).

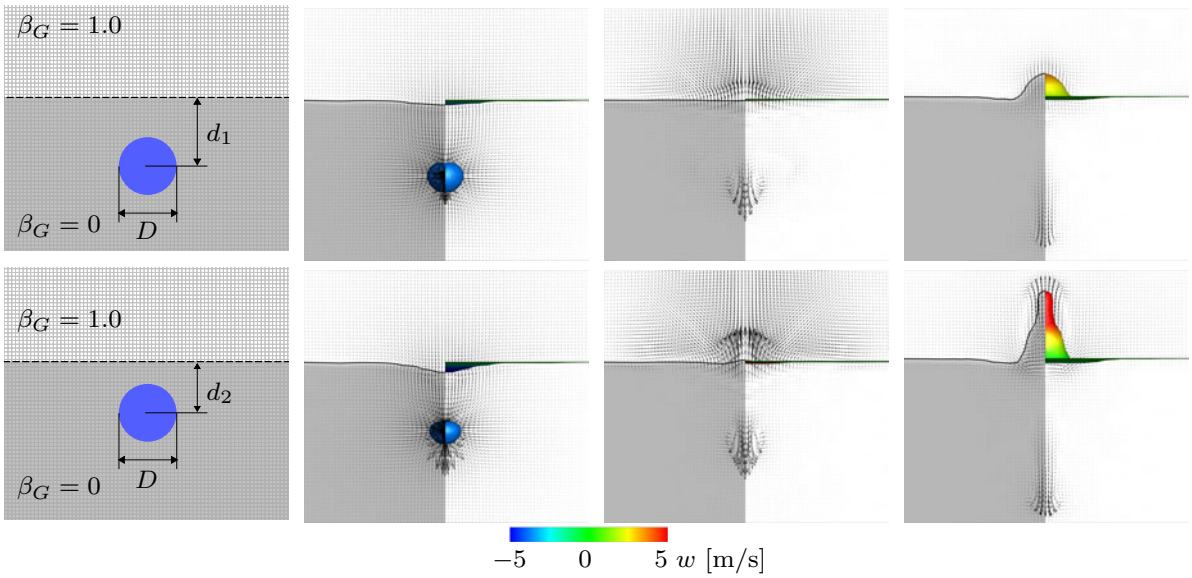

(a) $t = t_0$ (b) $t = t_0 + 7.0\ \mu$s (c) $t = t_0 + 9.0\ \mu$s (d) $t = t_0 + 27.0\ \mu$s

Figure 5.27: Collapse of single cavitation bubbles in the proximity of a liquid-gas interface at various instants in time. Bubble has an initial diameter $D = 0.2$ mm and is placed at a distance $d = \{0.17, 0.145\}$ mm from the the interface. Snapshots show iso-surfaces of vapor volume fraction $\alpha = 0.1$ (blue), gas volume fraction $\beta_G = 0.99$ colored by interface-normal velocity w (right half of figures), and liquid mass fraction on the symmetry plane (shaded grey) together with contour-line $\beta_G = 0.99$ (left half of figures).

We show iso-surfaces of vapor volume fraction $\alpha = 0.1$ (blue) in a top view without a visuatization of the jet (left column), together with top (middle column) and side view (right column) of vapor structures and an iso-surface of the gas volume fraction $\beta_G = 0.99$ colored by w-velocity.

We follow a cavitation structure marked in Fig. 5.28(a). The structure is convected downstream and has passed the nozzle exit plane in Fig. 5.28(b). A short time after the vapor cloud has collapsed under the high pressure that is imposed from the surrounding fluid, see Fig. 5.28(c). A collapse near the jet surface causes an acceleration of liquid towards the liquid-gas interface and a small, high velocity liquid spike emerging from the jet surface, which is marked in Figs. 5.28 (d) and (e).

In summary, the four described mechanisms significantly add to the generation of momentum directed towards the liquid-gas interface, which causes a widening and primary break-up of the liquid jet surface.

5.3 Summary

The collapse of isolated single bubbles is often used for a first validation of cavitation models. We have shown that the homogenous mixture single-fluid two-phase model is able to accurately predict the collapse of a vapor bubble in liquid water. The bubble collapse in the vicinity of a solid wall has been found to be in good agreement with reference data obtained with a sharp interface method.

Many experimental studies show that cavitation phenomena play a crucial role in jet break-up and vaporization. Still, the simulation of cavitating nozzle flows injected into a free gas phase remains a challenging task. As many complex models are limited to relatively simple configurations, one has to find a compromise between feasibility and applicability to realistic problems. Focus of the validation study is the initial stage of the jet break-up. The simulation of the secondary break-up, that is, ligament and droplet formation, has not been considered since the current model does not include surface tension effects.

The two-fluid two-phase model has been applied to a cavitating nozzle slot and jet flow injected into air. The setup of the present study has been subject to extensive experimental investigation. We have performed LES for three different cavitation numbers, each of which shows different characteristics of the nozzle flow and of the liquid jet. Cavitation structures within the duct resemble experimental results. Quantitative measurements of mean and fluctuating velocity components reveal a lower level of turbulence in the simulation, which we attributed to disturbances induced by the experimental apparatus. In contrast to the experiments, we have observed that cavitation promotes the break-up of the jet in lateral direction. In addition to classical Kelvin-Helmholtz type large scale instabilities of the jet surface, three main mechanisms suggested to be responsible for jet break-up in cavitating liquid flows have been reproduced and analyzed, namely turbulent fluctuations induced by the collapse of cavitation structures in the proximity of the exit plane of the nozzle, entrainment of gas into the nozzle, and collapse events inside the jet

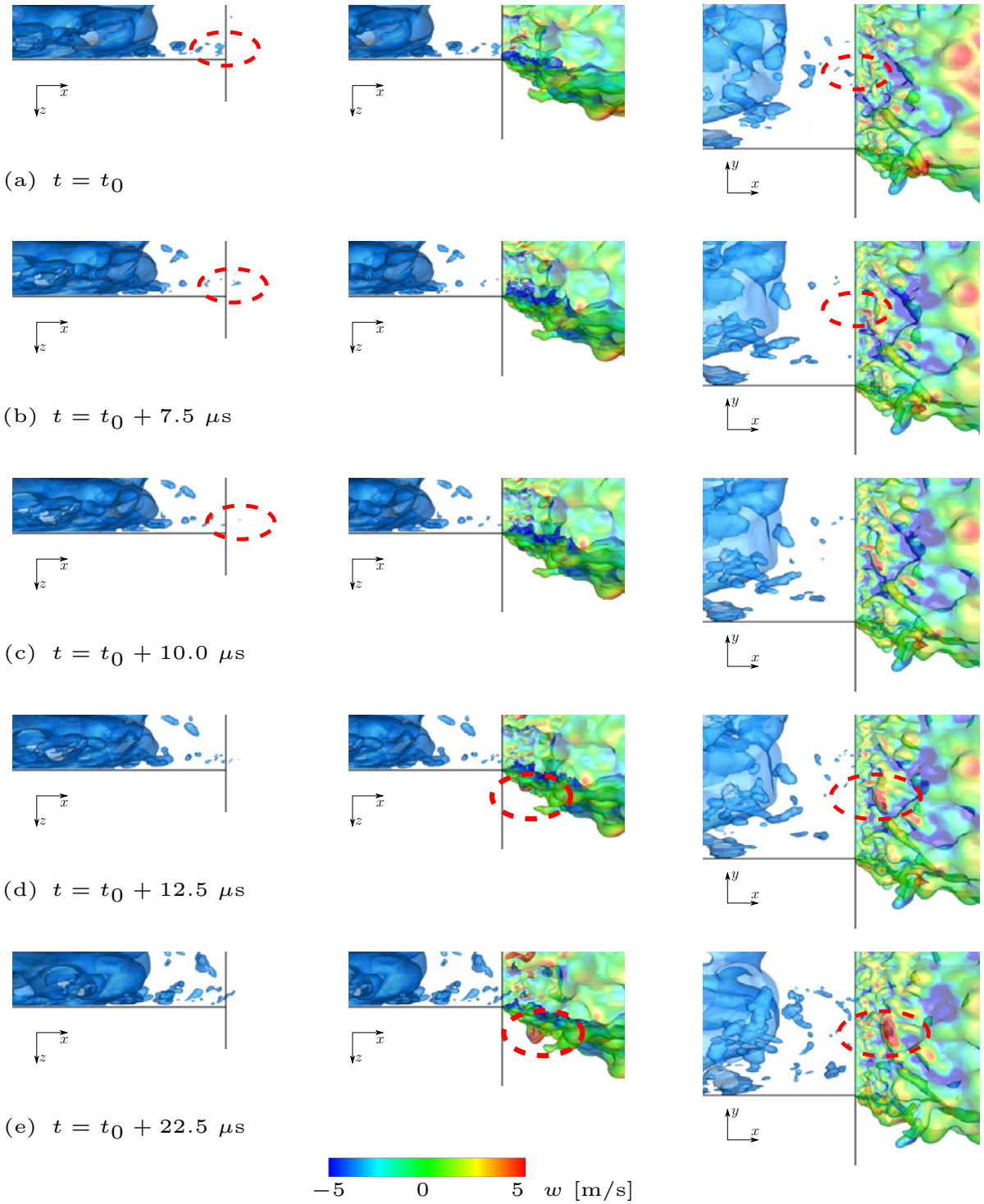

Figure 5.28: Collapse event inside the jet. Snapshots show iso-surfaces of $\alpha = 0.1$ (blue), and gas volume fraction $\beta_G = 0.99$ colored by w velocity. Snapshots are taken at the same instant in time. Collapse position and emerging liquid jet are highlighted by a red-dashed marker.

near the liquid-gas interface. All three mechanisms induce momentum directed away from the jet axis and lead to primary break-up of the jet. Collapse events near the exit and outside the nozzle region were found to be of particular importance. A fully compressible description of the flow is essential to capture such mechanisms.

6 Flow Inside a Nine-Hole Diesel Injector

In the following chapter, we investigate the turbulent multiphase flow inside a nine-hole common rail Diesel injector during a full injection cycle of ISO 4113 Diesel fuel into air. The simulation includes a prescribed needle movement obtained from a one-dimensional Multi-Domain Simulation. The injector geometry is represented by the cut-element based immersed boundary method. For this study, we employ the barotropic two-phase two-fluid model introduced in Sec. 2.2.3 for liquid and gaseous ISO 4113 Diesel Fluid, see Sec. 2.2.2, and non-condensable air.

This section has been published in Örley et al. [131]. Reprinted with permission by Sage Publishing.

6.1 Simulation Setup

6.1.1 Geometry and Simulation Strategy

We investigate the flow inside a nine-hole CR Diesel injector, which is shown in Fig. 6.1. The geometry was provided by Huber and Ulbrich [88]. The tapered nozzle holes, which are inclined by $\alpha_H = 15.57°$, have an inlet diameter of $D_{H,in} = 175 \times 10^{-6}$ m, an outlet diameter of $D_{H,out} = 135 \times 10^{-6}$ m, and a length of $L_H = 800 \times 10^{-6}$ m. The K-factor in

Table 6.1: Geometric parameters of the nine-hole CR Diesel injector.

Symbol	Parameter	Value
d_{N1}	Main needle diameter	2.8×10^{-3} m
d_{N2}	Needle diameter at needle volume	2.0×10^{-3} m
α_{N1}	Chamfer angle at needle volume	46.52°
α_{N2}	Needle seat angle	28.66°
α_{N3}	Needle tip angle	46.76°
d_{NL}	Inner diameter of nozzle line	3.4×10^{-3} m
h_S	Height of sac volume	0.77×10^{-3} m
α_H	Nozzle hole inclination angle	15.57°
$D_{H,in}$	Nozzle hole inlet diameter	175×10^{-6} m
$D_{H,out}$	Nozzle hole outlet diameter	135×10^{-6} m
k	K-Factor	4
L_H	Length of nozzle hole	800×10^{-6} m
$R_{H,in}$	Nozzle hole inlet radius	40×10^{-6} m
n	Number of nozzle holes	9

this case is $k = (D_{H,in} - D_{H,out})/10 = 4$. Deviations from the nominal dimensions of the individual nozzle holes, which may occur under realistic operation of the injection system, are neglected. The height of the sac-hole volume is $h_S = 770 \times 10^{-6}$ m. Details on the geometrical parameters of the nozzle holes, the needle, and the nozzle line are summarized in Tab. 6.1.

In our simulation, we model only the nozzle line and half of the ring chamber of the high-pressure system. Figure 6.2 shows the injector geometry embedded into the computational domain. To maintain a constant reservoir pressure and to avoid any influence of boundary conditions close to the region of interest, we connect the ring chamber to a large high-pressure volume and prescribe total pressure boundary conditions equal to the chosen rail pressure at the top of the domain, see Fig. 6.2(a). The outlet chamber is modelled in the same way. The high- and low-pressure chambers are only linked via the injector, Fig. 6.2(b). All side-walls of the pressure chambers are modelled as slip walls. We initialize the domain with liquid fuel, that is, $\xi_G = 0$, at rest at a rail pressure of $p_R = 1500$ bar above the needle seat, and gas, that is, $\xi_G = 1$, at chamber pressure $p_C = 10$ bar, otherwise. During the simulation, liquid fuel without a non-condensable gas is prescribed at the inlet boundary, that is, $\xi_{G,in} = 0$, in order to reproduce the boundary data of the one-dimensional reference simulation. We also investigated an operation at a rail pressure of $p_R = 2000$ bar, but found no significant difference in the flow features when compared to the lower rail pressure. We therefore focus our analysis on the latter case.

Initially, the needle is at its closed state and the high-pressure region is separated from the low-pressure outlet region. To maintain numerical stability, the minimum lift of the needle is approximately 4 μm. This means that the immersed boundaries for the injector casing and needle are within a single computational cell. During the simulation, the needle lift is prescribed. The needle lift l_N and needle lift velocity v_N, see Fig. 6.3, are obtained from a

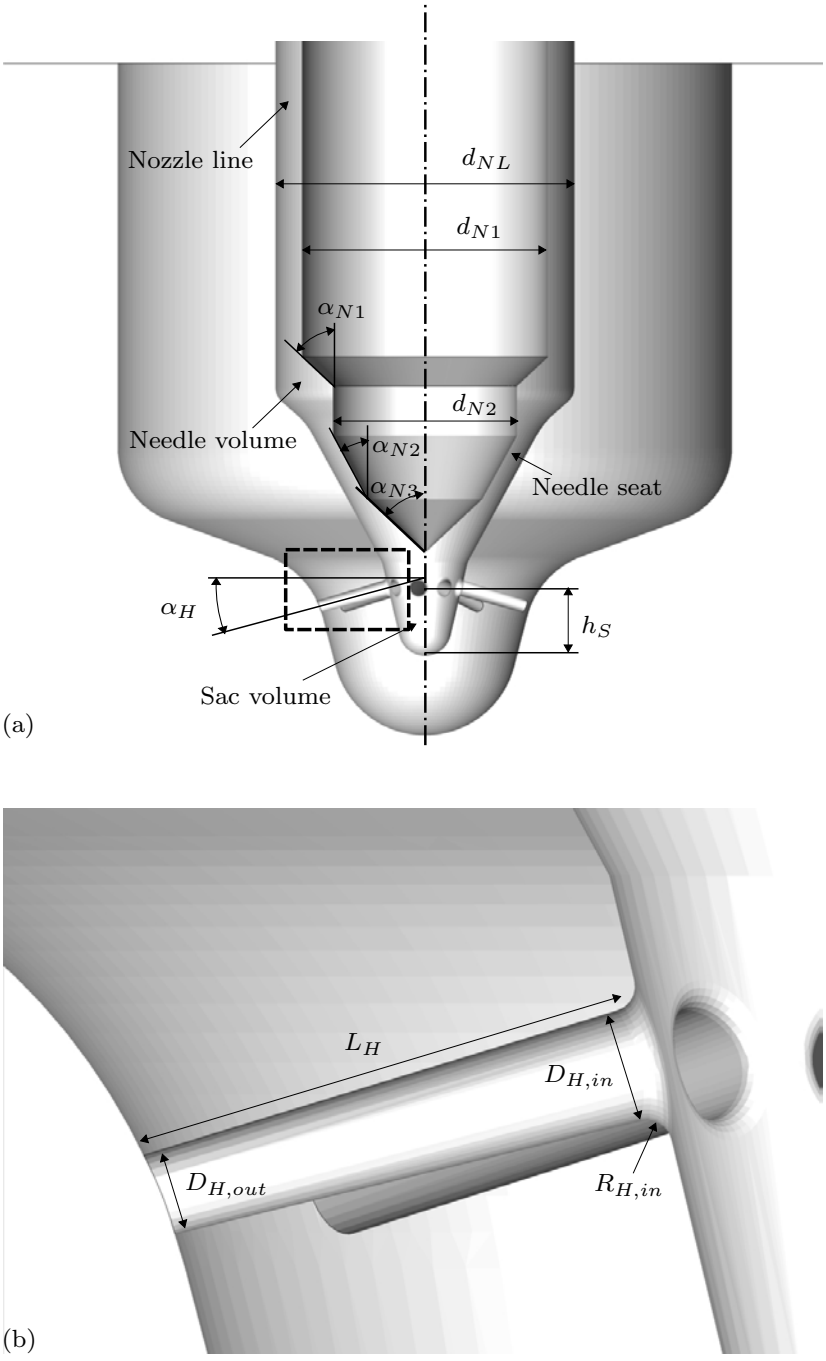

Figure 6.1: Geometry of the nine-hole CR Diesel Injector [88]: (a) full view of the needle seat and sac-hole region; (b) detailed view on the symmetry plane of a single injector hole (marked with dashed line).

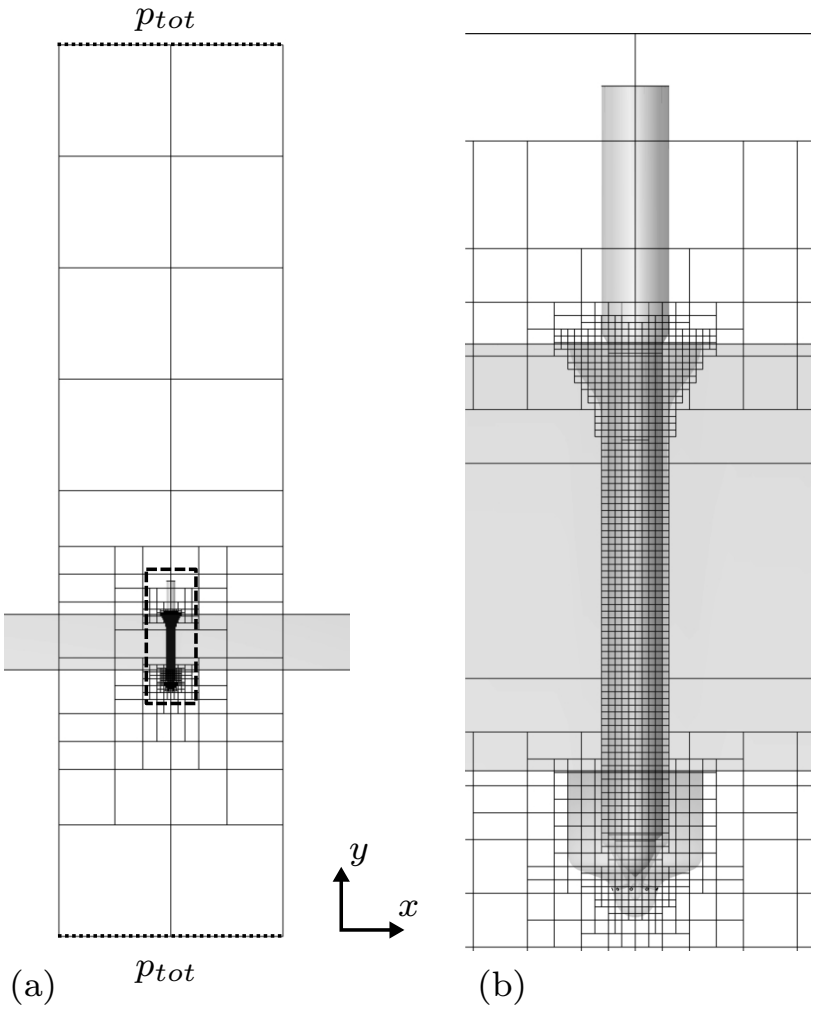

Figure 6.2: Computational domain and block structure of the nine-hole CR injector simulation: (a) full domain; (b) detailed view on the injector casing and needle (marked with dashed line).

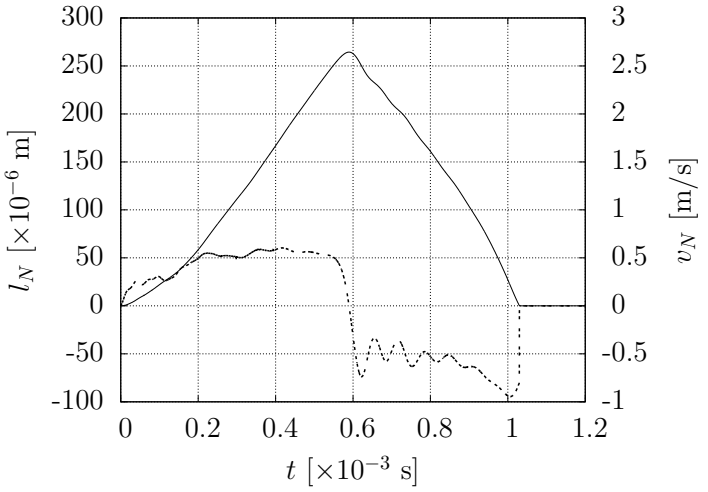

Figure 6.3: Needle lift (—) and needle velocity (·····) for rail pressure $p_R = 1500$ bar [88].

dynamic multi-domain simulation model by Huber and Ulbrich [88]. The injection cycle corresponds to a holding time of the solenoid valve driving current of $t_{hold} = 0.7$ ms. For injection pressures of $p_R = 1500$ bar, the maximum needle lift is $l_{N,max} = 264.4$ μm and the needle is in a ballistic operational mode.

6.1.2 Computational Setup

We discretize the domain with a Cartesian block-structured mesh, see Fig. 6.2. To reduce computational cost, we employ a local grid refinement near the needle seat, the sac-hole, the nozzle holes, and in the outflow region. We perform simulations on three different grid levels with successive refinement in the needle seat and nozzle hole regions. The coarse grid, subscript c, consists of approx. 35.2×10^6 cells with a smallest cell size of $\Delta x_c = 20 \times 10^{-6}$ m. The medium, subscript m, and fine grid, subscript f, consist of approx. 49.5×10^6 and 81.6×10^6 cells with a smallest cell size of $\Delta x_m = 10 \times 10^{-6}$ m and $\Delta x_f = 5 \times 10^{-6}$ m, respectively. On the finest grid level, the small cell size and the large speed of sound of the liquid phase limits the timestep size to 0.74×10^{-9} s. The grid parameters are summarized in Tab. 6.2. Details on the numerical grid of the three grid levels are shown in Fig. 6.4. To capture circumferential asymmetries in the flow field, we compute the full 360° geometry including all nine nozzle holes on the coarse and medium grid. Since a full system simulation is not feasible on the finest grid level, we reduce our computational domain to 180° at the symmetry plane, see Fig. 6.5(a). In the following, quantities denoted by $\langle \bullet \rangle$ are averaged over the nozzle holes. To compare our results across different grid resolutions, we average nozzle holes inside the 180°-domain marked in Fig. 6.5(a). Pressure probe positions are shown in Fig. 6.5(a/b). The probe positions are denoted by S1-S6. Sensors S1 and S2 are located at equal y-position and are distributed on a circular line with constant angular spacing. Sensor S3 is located in the sac-hole. Sensors S4-S6 correspond to measurement points located at the center of

Table 6.2: Grid parameters for three investigated grid levels.

Grid level		Coarse	Medium	Fine
Cell count	$[\times 10^6]$	35.2	49.5	81.6
Min. Cell size	$[\times 10^{-6}$ m]	20	10	5
Time step	$[\times 10^{-9}$ s]	3.6	1.75	0.74

the inlet, mid, and outlet cross-section of the nozzle holes.

6.2 Results and Discussion

In the following, we evaluate the results obtained from our LES. We first compare integral quantities measured on different grids to the results obtained from the multi-domain simulation model. Subsequently, we assess the three-dimensional flow field of the different phases of the injection cycle. A focus is put on the assessment of erosion prediction in terms of the location and dynamics of cavitation regions and their collapse behavior. Finally, we compare our results including a unsteady needle movement to data obtained from computations with a steady needle.

6.2.1 Mass Flow and Pressure Measurements during the Injection Cycle

First we compare the mass flow rate obtained on the three investigated grids. Figure 6.6 shows the temporal evolution of the averaged injection rate and standard deviation together with reference data [88]. Based on the temporal evolution of the injection rate, we define four phases of the injection cycle, which significantly differ in terms of injection rate, fluid flow turbulence, and cavitation characteristics. The different phases are the startup phase ($0 < t < 0.25$ ms), main injection ($0.25 < t < 0.95$ ms), needle closing ($0.95 < t < 1.03$ ms), and sealed needle seat ($1.03 < t < 1.15$ ms), as summarized in Tab. 6.3.

Our numerical results correspond well to the data obtained with the multi-domain simulation model. During the startup phase 1, our simulation first provides a lower mass flow than the 1D-simulation. This effect can be accredited to the fact that the multi-domain simulation model does not include cavitation effects in the needle seat. Our LES shows that cavitation leads to choked conditions at the needle seat. Once the needle lift is large enough, the mass flow rate rapidly rises to a value of approximately 6.5 g/s. During the main injection, phase 2, the mass flow rate is limited by choked conditions in the nozzle hole outlet area and remains almost constant. As soon as the closing needle has reached a lift of approximately 50 μm, phase 3, choked conditions in the needle seat again limit the mass flow rate. After the needle seat is closed, phase 4, the mass flow is blocked in the

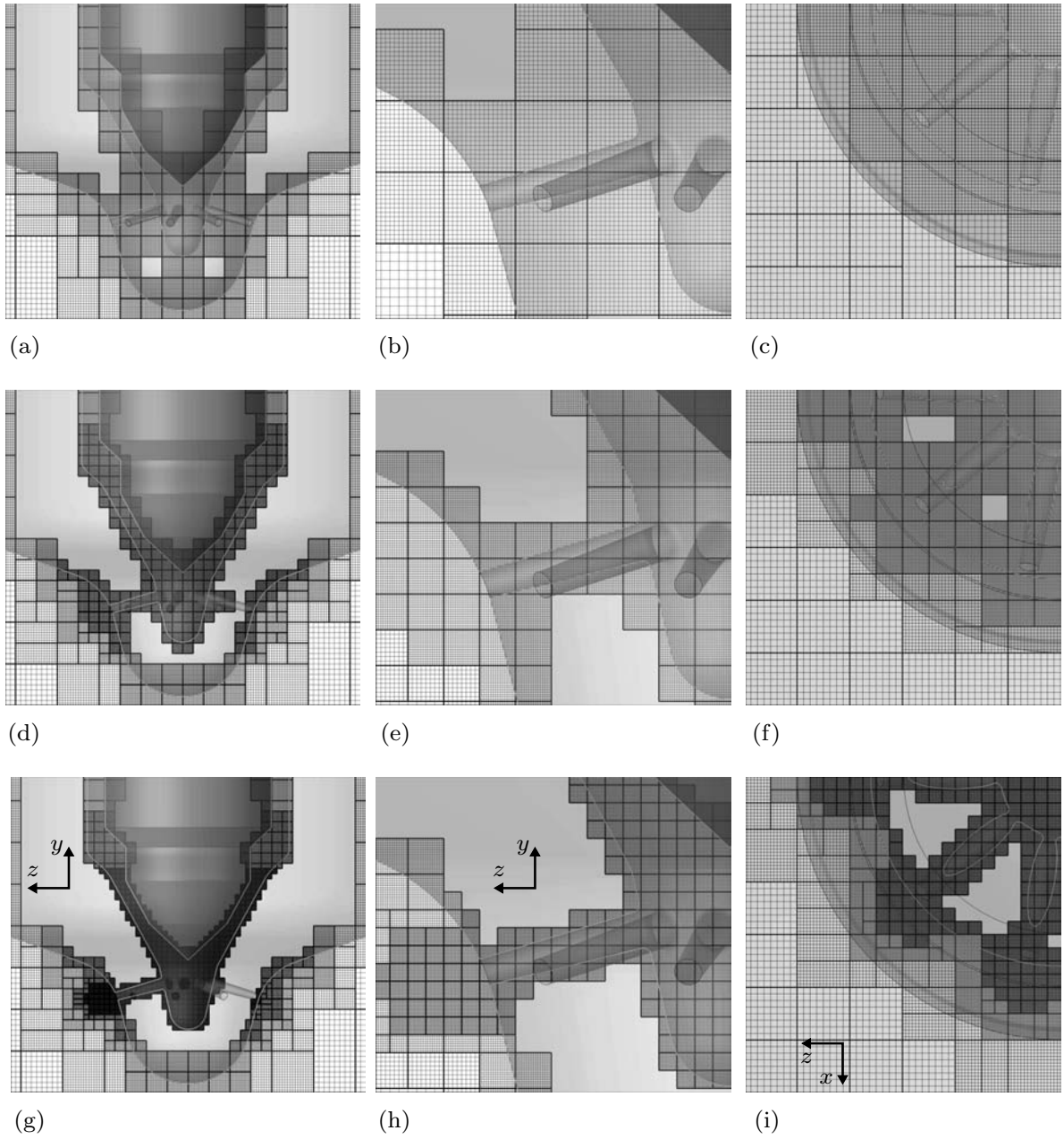

Figure 6.4: Computational grids and Cartesian block structure in the nozzle holes and needle seat for the coarse grid, medium grid, and fine grid (from top to bottom): z-y view in the x symmetry plane (left column); detailed view of the nozzle hole in the x symmetry plane (middle column); x-z view in a cut-plane through the nozzle holes (right column). Contours of the nozzle and needle geometry on the cut-planes are marked with a line.

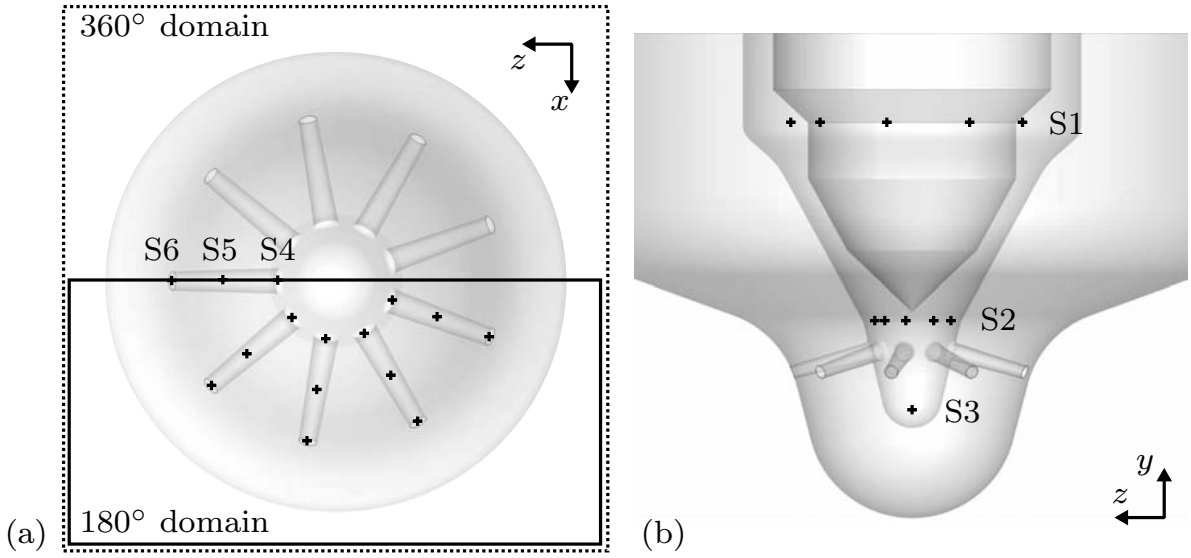

Figure 6.5: Top view (a) and side view (b) of the injector geometry. 360° sector computed on the coarse and medium grid (·····), and 180° sector computed on the fine grid (—). Probe positions are marked.

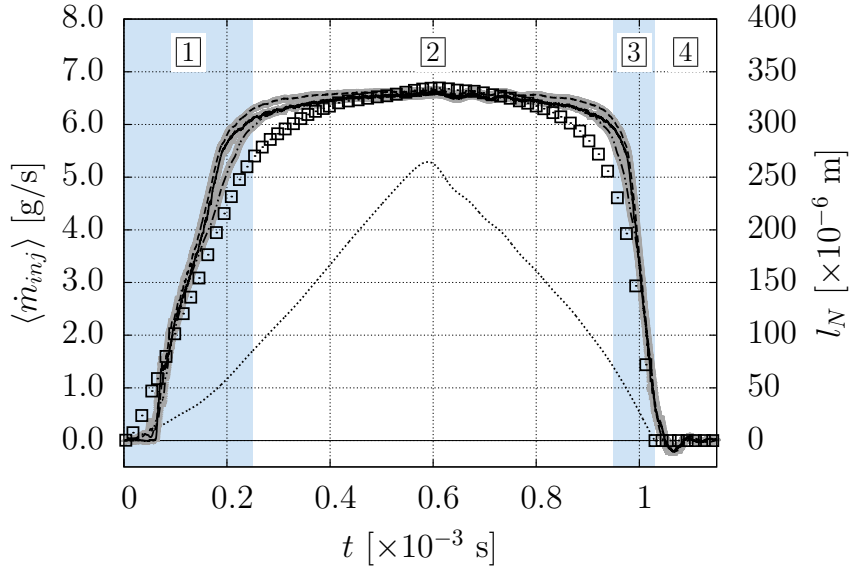

Figure 6.6: Temporal evolution of average injection rate $\langle \dot{m}_{inj} \rangle$ of a single hole for coarse (-·-·), medium (- - -), and fine (—) grid, and needle lift (·····) [88]. The grey bands show standard deviation between nozzle holes.

Table 6.3: Definition of four characteristic phases during the injection cycle.

Phase	Time interval [ms]	Phase description
1	$0 < t < 0.25$	Startup phase
2	$0.25 < t < 0.95$	Main injection
3	$0.95 < t < 1.03$	Needle closing
4	$1.03 < t < 1.15$	Sealed needle seat

Table 6.4: Total injected mass during one injection cycle.

	$\langle m_{inj} \rangle$ [$\times 10^{-3}$ g]	σ [$\times 10^{-3}$ g]
Coarse grid	5.4481	0.0284
Medium grid	5.6671	0.0215
Fine grid	5.5436	0.0265
Reference data [88]	5.2789	-

multi-domain simulation. In the LES, compressibility effects cause a back-flow through the nozzle holes before all disturbances of the closing process have decayed.

The discharge coefficient, which relates the maximum mass flow measured in the simulation to the maximum theoretical injection rate, is defined as

$$C_d = \frac{\dot{m}_{inj,max}}{\dot{m}_{inj,th}} = \frac{\dot{m}_{inj,max}}{A_{H,out}\sqrt{2\rho_R(p_R - p_C)}}. \tag{6.1}$$

In our simulations we compute a discharge coefficient of approximately $C_d = 0.89$ during the main injection phase, which is a typical value for non-cavitating nozzle flows with a K-factor of k=4, see, e.g., Schmidt [159].

The total injected mass, m_{inj}, during the cycle is obtained by time integration of the measured mass flow rate for each individual hole. Table 6.4 summarizes the total injected mass averaged over all holes together with the standard deviation and reference data [88]. For all grids, the injected mass lies within 5% error to the one-dimensional multi-domain simulation model. The low standard deviation verifies a negligible hole to hole variation.

A comparison of integral quantities, such as injection rate and total injected mass, suggests that a grid convergence is already reached for very coarse grids. Never the less, the characteristic flow structures are not well represented on the coarse and medium grid levels, which is discussed below.

Figure 6.7 shows the temporal evolution of the average pressure signal $\langle p \rangle$ at sensor positions S1-S6 as defined in Fig. 6.5. The pressure level upstream of the needle seat remains at rail pressure, which validates our method to prescribe a constant high pressure reservoir via a large connected volume. In the opening phase, the main pressure drop is observed over the needle seat (S1 to S2/S3). In the main injection phase, the pressure level

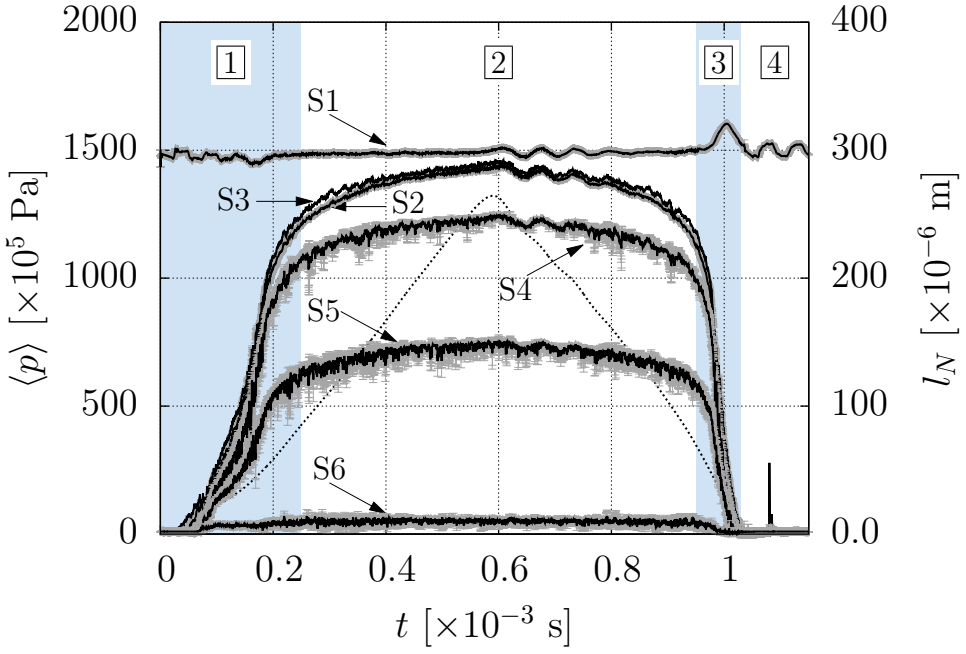

Figure 6.7: Temporal evolution of average pressure signal $\langle p \rangle$ at sensor positions S1-S6 (—) computed on the fine grid and needle lift (·····). The grey bands show standard deviation.

in the sac-hole volume S2/S3 is almost at rail pressure. In this phase, the main pressure drop occurs over the nozzle holes, that is, S4 to S6. The high standard deviation in this phase is caused by the highly dynamic flow structures inside the nozzle holes. Closing the needle raises the pressure level upstream of the needle seat and lowers the pressure in the sac volume. This leads to the formation and subsequent collapse of a large vapor bubble At $t = 1.1$ ms, a high pressure peak in the sensor S3 signal indicates the collapse of this structure in the sac volume. We will further analyse this process in Sec. 6.2.4 below.

6.2.2 Assessment of the Three-Dimensional Flow-Field

We now turn towards the analysis of the three-dimensional internal flow. In the following, we will discuss only results obtained on the finest grid level. A comparison to the medium and coarse grid levels is provided in the next section

Figures 6.8-6.11 show snapshots of velocity contours on the symmetry plane, iso-surfaces of coherent vortical structures visualized by the λ_2 criterion, and iso-contours of the vapor volume fraction α.

During the startup phase, see Fig. 6.8, which shows a snapshot taken at $t = 130 \times 10^{-6}$ s at a needle lift $l_N = 30.5 \times 10^{-6}$ m, the flow field is dominated by small scale turbulent fluctuations inside the sac-hole and the nozzle holes. The turbulence is driven by a high frequency shedding process, which occurs at the outlet of the needle seat. A large separation is visible on the upper side of the nozzle holes near the inlet edge. A vapor

sheet indicates the choked conditions in the needle seat, which limits the mass flow during this phase.

Figure 6.9 shows snapshots of the main injection phase at $t = 580 \times 10^{-6}$ s at a needle lift $l_N = 264.4 \times 10^{-6}$ m. The flow inside the sac-hole is still fully turbulent. Now, the nozzle hole outlet area limits the mass flow rate. The velocity level inside the needle seat thus is lower than in the startup phase. Inside the nozzle holes large, stable vortices in axial direction now dominate the flow. In each hole, several of these structures are present at the same time. The origin of these vortices lies upstream of the needle seat in the needle chamber. At this location large vortex rings are shed by the backward facing needle. These vortex rings are disturbed when being convected into the needle seat, break up, and form long, streamwise vortical structures, which are being further accelerated in the converging needle seat area. Inside the nozzle holes, the vortices are further accelerated and stretched. As a result, the pressure drops near to saturation pressure on the nozzle outlet plane. Due to the pressure drop inside the vortex core, the liquid evaporates and vapor is generated. During the main injection phase, this is the only location where cavitation is detected.

When the needle comes near to closing the injector, see Fig. 6.10, which shows the flow field at $t = 996 \times 10^{-6}$ s at a lift $l_N = 30.0 \times 10^{-6}$ m, the flow inside the nozzle holes again undergoes transition to a fully turbulent state. Cavitation occurs near the inlet of the nozzle holes due to the strong acceleration of fluid from the needle seat into the nozzle holes and the lower pressure level inside the sac-hole compared to the main injection phase.

Finally, at $t = 1082 \times 10^{-6}$ s, see Fig. 6.11, the flow is characterized by decaying turbulent fluctuations after the needle is fully sealed. Inside the sac-hole, we observe the formation and collapse of cavitation structures, which are generated in the sac-hole by inertia effects shortly after closing of the needle. In the nozzle holes, a backflow of liquid and gas from the combustion chamber is observed after the re-condensation of large vapor volumes in the sac-hole region.

6.2.3 Effect of grid resolution on flow features

In the following, we discuss the effect of grid resolution on characteristic flow features during the main injection phase. Figure 6.12 shows coherent turbulent structures visualized by the λ_2 criterion and the absolute velocity on the symmetry plane obtained on the three investigated grids at $t = 600 \times 10^{-6}$ s and at a needle lift of $l_N = 262.8 \times 10^{-6}$ m.

On the finest grid, Fig. 6.12(e), as discussed above, vortical structures are created upstream of the needle seat and are advected into the nozzle holes, where they are accelerated and stretched. This process can also be observed on the medium grid, Fig. 6.12(c). Compared to the finest grid, the number of vortices created is smaller, and vortices inside the nozzle holes are not as well resolved, but nevertheless the overall evolution is found to be similar. A significant difference is found when comparing the small-scale turbulence in the sac-hole found on the fine grid, which is not resolved on the medium grid. On the coarse grid, Fig. 6.12(a), elongated vortical structures are not present. Fluctuations

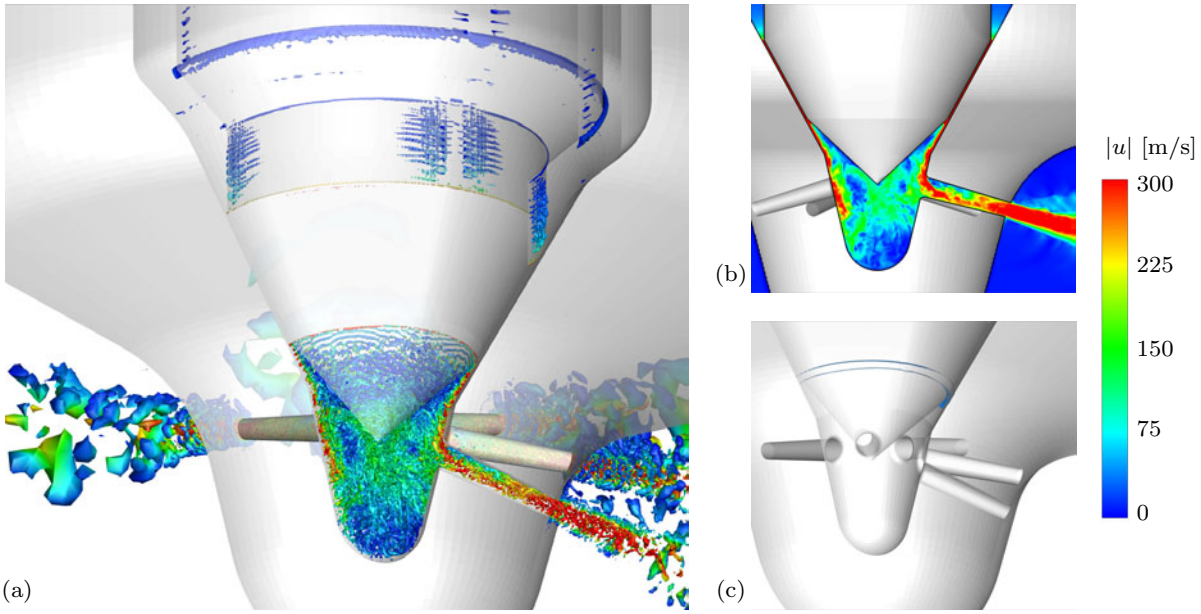

Figure 6.8: Snapshots of iso-contours of $\lambda_2 = -2 \times 10^{-10}$ s^{-}2 colored by absolute velocity (a), velocity contours on the symmetry plane (b), and iso-contours of $\alpha = 0.05$ (c) at $t = 130 \times 10^{-6}$ s and needle lift $l_N = 30.5 \times 10^{-6}$ m.

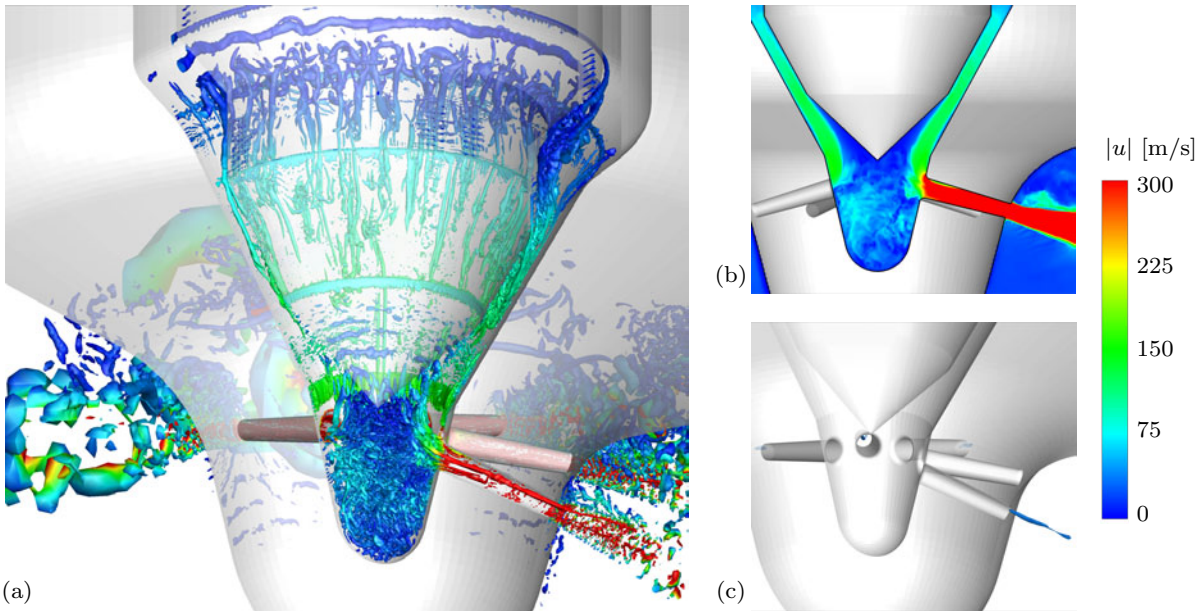

Figure 6.9: Snapshots of iso-contours of $\lambda_2 = -2 \times 10^{-10}$ s^{-}2 colored by absolute velocity (a), velocity contours on the symmetry plane (b), and iso-contours of $\alpha = 0.05$ (c) at $t = 580 \times 10^{-6}$ s and needle lift $l_N = 264.4 \times 10^{-6}$ m.

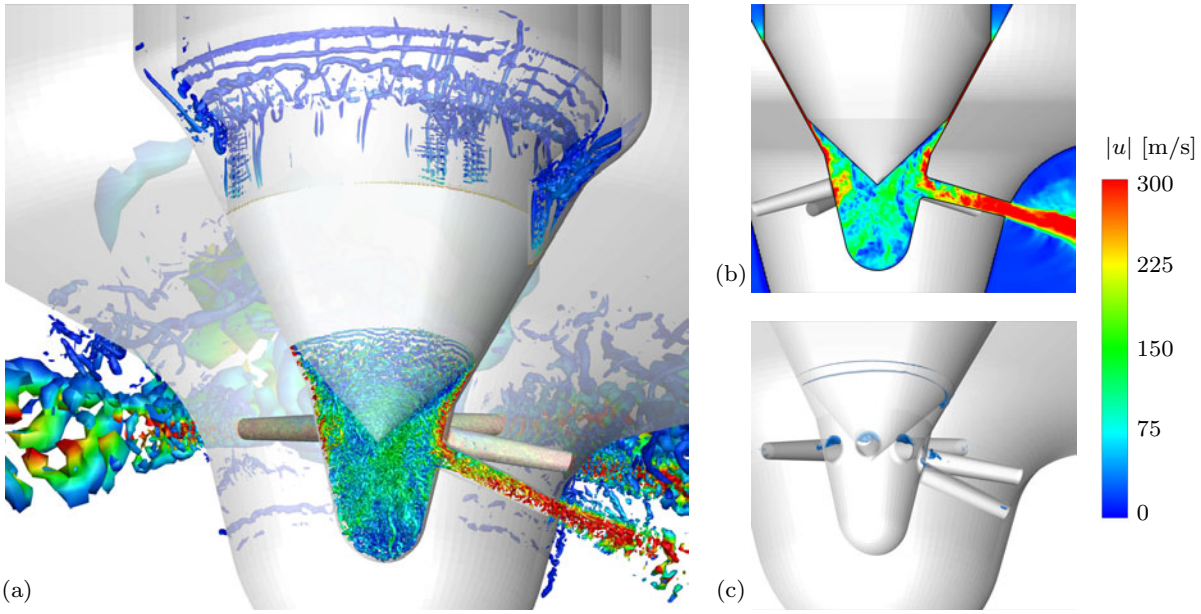

Figure 6.10: Snapshots of iso-contours of $\lambda_2 = -2 \times 10^{-10}$ s^{-}2 colored by absolute velocity (a), velocity contours on the symmetry plane (b), and iso-contours of $\alpha = 0.05$ (c) at $t = 996 \times 10^{-6}$ s and needle lift $l_N = 30.0 \times 10^{-6}$ m.

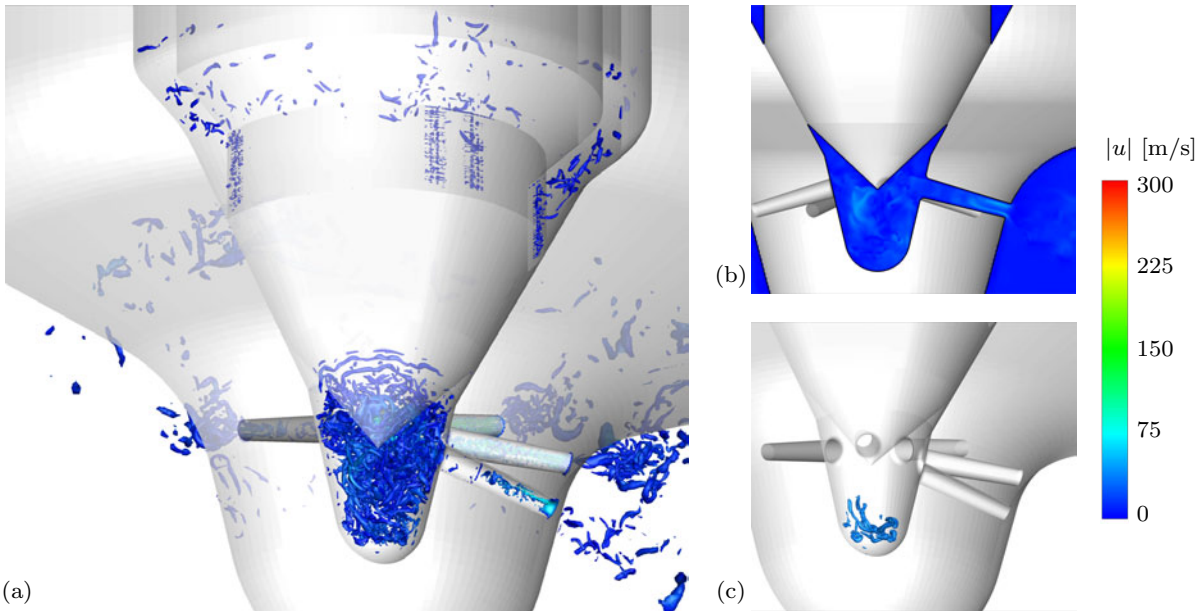

Figure 6.11: Snapshots of iso-contours of $\lambda_2 = -2 \times 10^{-10}$ s^{-}2 colored by absolute velocity (a), velocity contours on the symmetry plane (b), and iso-contours of $\alpha = 0.05$ (c) at $t = 1160 \times 10^{-6}$ s and needle lift $l_N = 0 \times 10^{-6}$ m.

in the sac-hole are even more reduced. The velocity magnitude on the symmetry plane shows a similar evolution for all grid levels, Fig. 6.12(b/d/f), implying a grid-converged total mass flow. A significant difference again is the visible turbulence in the sac-hole found on the fine grid, Fig. 6.12(f), as well as a flow detachment at the nozzle inlet, which increase with grid resolution.

In summary, results for the medium and fine grid compare well in terms of turbulent structures and integral flow quantities, such as mass flow and pressure measurements, indicating that the LES on the finest grid provides a reliable database for the analysis of the flow field during the injection process.

6.2.4 Cavitation Characteristics and Erosion Assessment

A main focus of this study is to identify erosion sensitive areas during operation of the injector. With our numerical simulation results for the full injection cycle we are able to resolve and assess the onset of cavitation both spatially as well as temporally. This provides important information on the location where and the instant in time when damage due to violent collapse events may be expected.

Figure 6.13 shows the temporal evolution of the total vapor volume α_{tot} within the computational domain. During the opening phase, a peak indicates cavitation in the needle seat. In the main injection phase, cavitation only occurs inside the vortex cores outside the nozzle holes. The total vapor volume produced during this phase is very low. The sharp rise during the closing phase is caused by the development of cavitation inside the needle seat, and is further increased by the development of cavitation structures in the nozzle holes and, after the needle seat is sealed, inside the sac volume. Note that the total vapor fraction is in very good agreement between the medium and fine grid. This suggests that at least the onset and magnitude of vapor formation can be predicted on a coarser grid, even if cavitation structures are not well resolved.

After the needle has closed the seat, the liquid inside the nozzle holes, which still has a high inertia, suddenly is strongly decelerated. This can only be achieved by a significant pressure drop inside the needle seat outlet and sac-hole region. In these regions large vapor clouds are generated. The cavitation structures at the time instant at which the total vapor fraction reaches its maximum are shown in Fig. 6.14(a). The nozzle holes are still partly filled with vapor. Shortly thereafter, Fig. 6.14(b), the vapor inside the nozzle holes and near the needle seat has re-condensated. The large vapor structure inside the sac-hole starts to collapse slightly later under the increasing pressure. This is shown in a time series in Figs. 6.14(b-j). First, the cloud starts to shrink towards the lowest point of the sac-hole. The final re-condensation stage, Fig. 6.14(e), results in a strong collapse event, during which the liquid is strongly accelerated towards the lower sac-hole wall. The wall pressure, which reaches values of several hundred bars, shows the footprint of the strong shock wave that is emitted during this event. Significant pressure peaks are detected on the sac-hole walls, nozzle inlets and the needle tip. The subsequent expansion again causes the liquid at the bottom of the sac-hole to evaporate, see Fig. 6.14(i/j), and

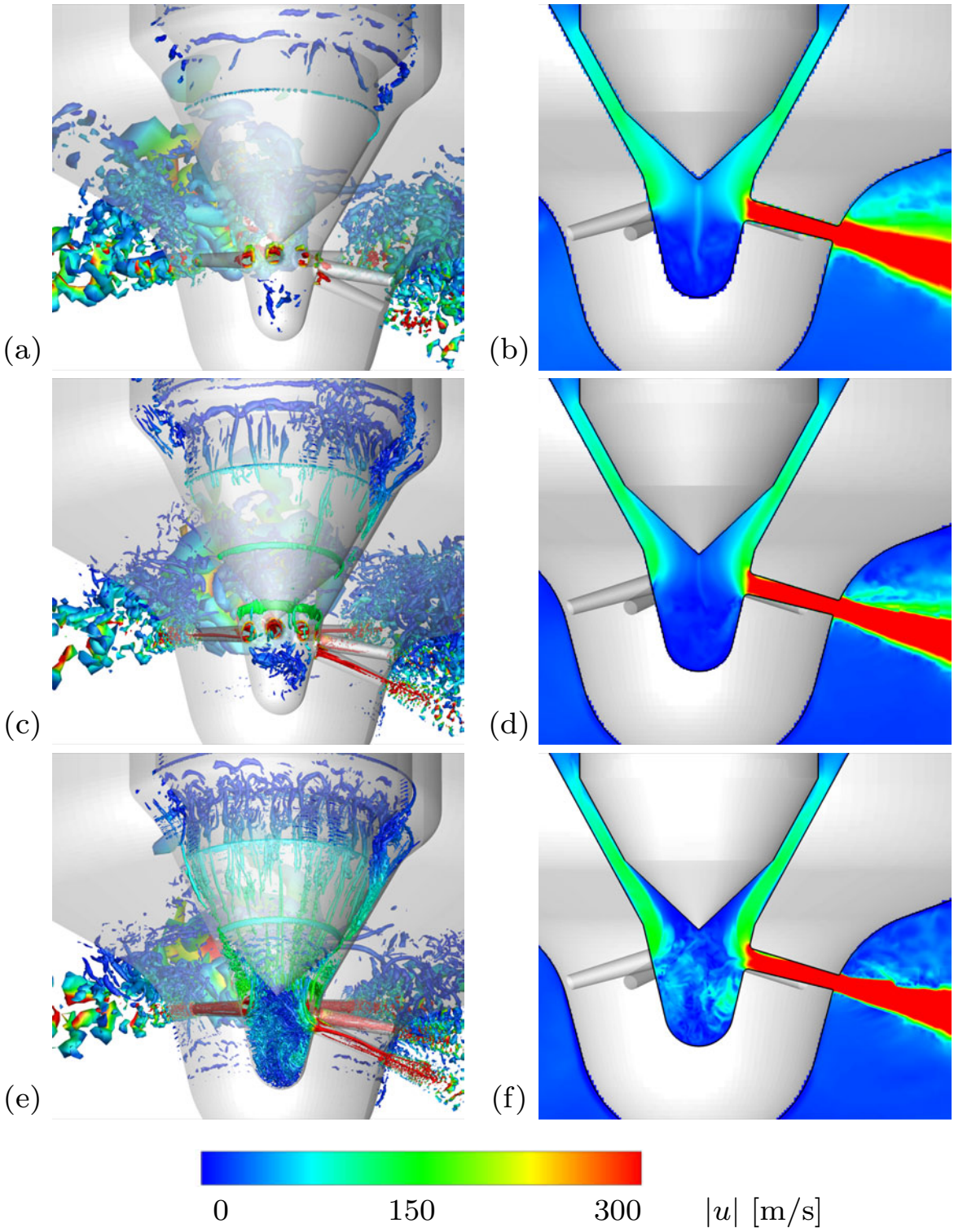

Figure 6.12: Snapshots of iso-contours of $\lambda_2 = -2 \times 10^{-10}$ s^{-2} colored by absolute velocity (left column) and velocity contours on the symmetry plane (right column) at $t = 600 \times 10^{-6}$ s as computed on the coarse (a/b), medium (c/d), and fine grid (e/f).

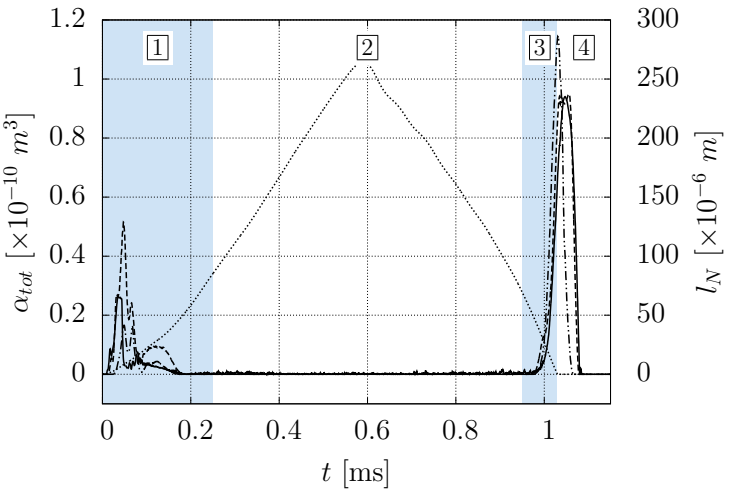

Figure 6.13: Temporal evolution of total vapor volume α_{tot} for coarse (-···-), medium (---), and fine (—) grid, and needle lift (·····).

leads to several weak rebounds, that is, the formation and collapse of vapor clouds with decreasing size.

In our numerical simulation we are able detect collapse events with an algorithm of Mihatsch *et al.* [119, 120], which tracks the re-condensation of vapor volume content inside a computational cell together with an analysis of the local velocity divergence. The normalized peak collapse pressure p_c is obtained by scaling the observed maximum p_m

$$p_c = p_m \frac{V_\Omega^{1/3}}{l_{ref}}, \tag{6.2}$$

where we set the reference length scale $l_{ref} = 3.75 \times 10^{-6}$ m to compensate for the effect of grid resolution onto the collapse pressure inside the cell with volume V_Ω [2]. We adopt the value of l_{ref} as proposed by Egerer *et al.* [48] in the study of a similar test case. We note that this value can be case dependent, and that the effect of its choice has been investigated for a different setup by Mihatsch *et al.* [119]. With this collapse detector we are able to quantify the time, location, and strength of isolated collapse events, which enables us to characterize the injection phases in terms of their erosion potential.

In Fig. 6.15, we show the collapse events during the four injection phases. Each individual event is visualized by a single sphere. Size and color of each sphere scale with the normalized collapse pressure p_c. In the initial phase 1, Fig. 6.15(a), a small number of collapses is found at the nozzle hole inlet and near the needle seat. During the main injection phase 2, see Fig. 6.15(b), collapse events are only found in the nozzle hole outlet region and outside the nozzle hole in the jet. During closing phase 3, Fig. 6.15(c), a large number of strong events is found over the full length of the nozzle holes, as well as near the needle seat and tip. After closing, phase 4, the collapse of vapor structures near the needle seat causes collapse events with very high peak pressure, compare Fig. 6.15(d). Subsequently, the collapse of the sac-hole cavity and rebound effects causes a large number of strong

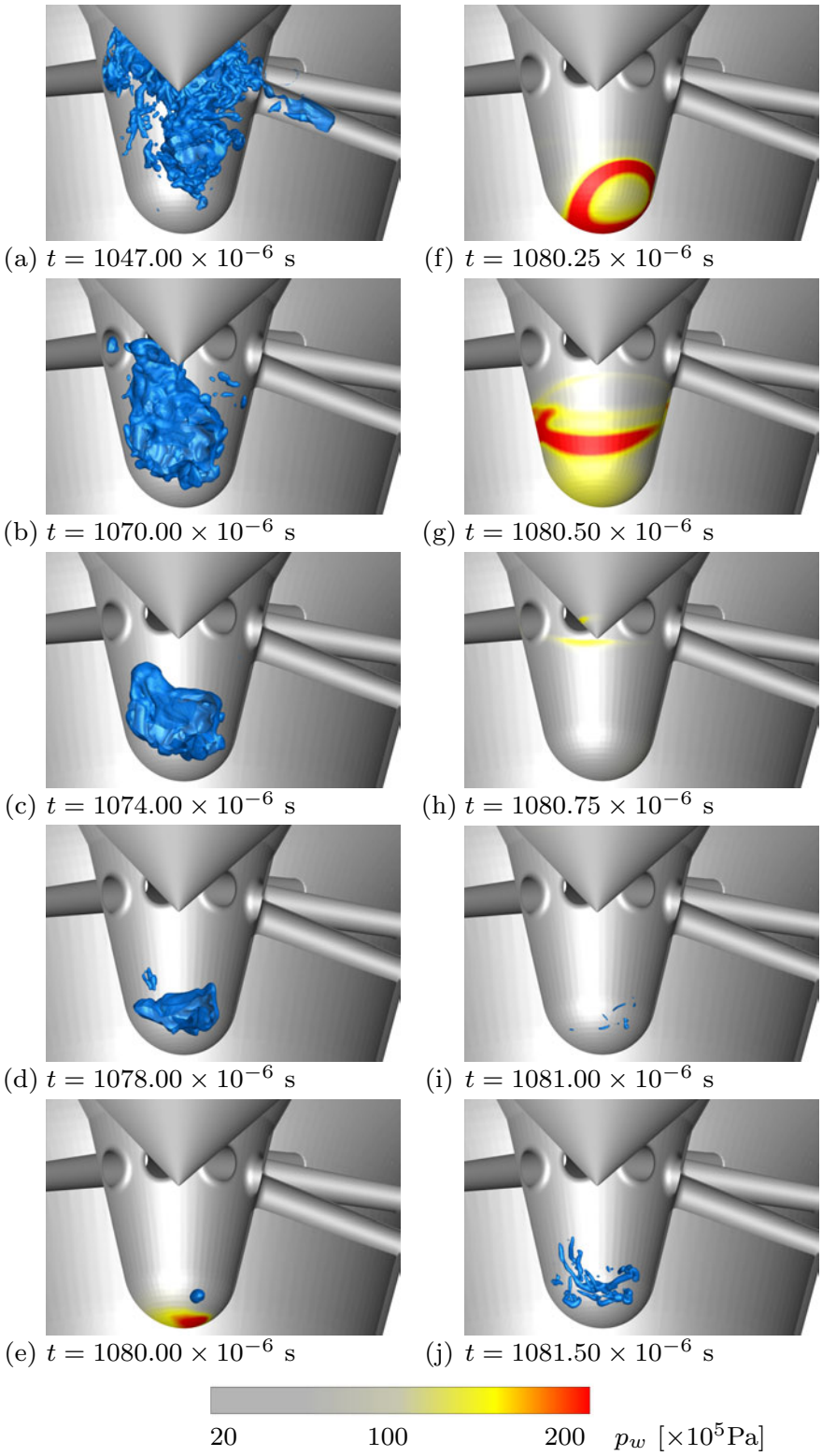

Figure 6.14: Collapse of sac-hole vapor structure: snapshots of iso-contours of $\alpha = 0.05$ and wall pressure.

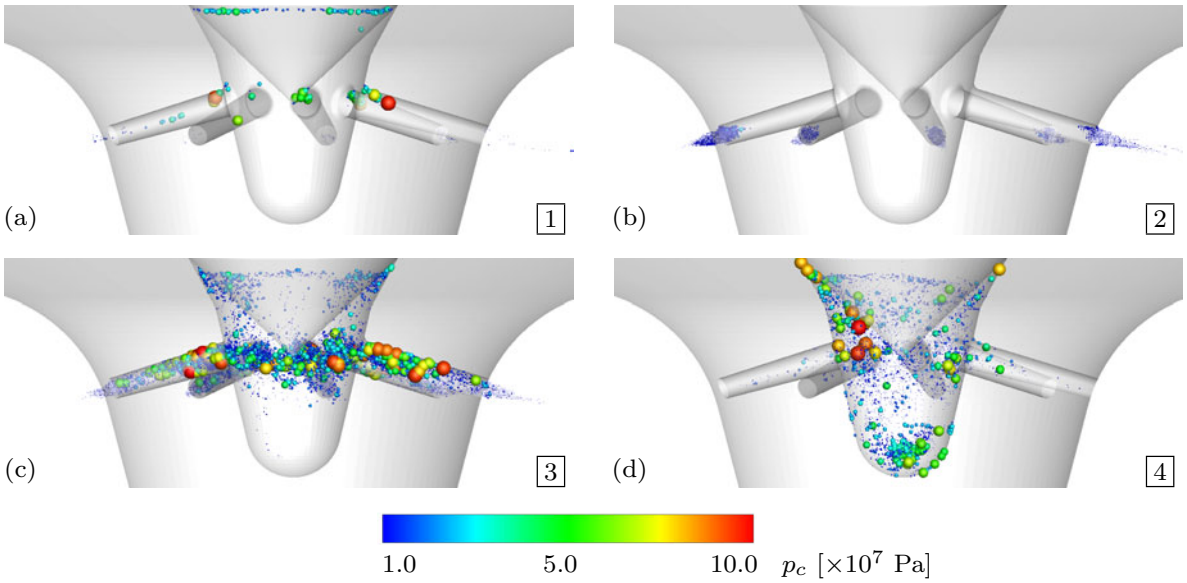

Figure 6.15: Spatial distribution of isolated collapse events detected during the characteristic injection phases. Size and color of each sphere is based on the normalized collapse pressure p_c.

events near the lowest point of the sac-hole.

6.2.5 Comparison to Steady Needle Simulations

Finally, we compare our LES of unsteady needle motion with simulation results performed for a steady needle at different positions. The grid and initial conditions are the same as for the unsteady simulation. After initialization, we let the flow develop over at least half an injection cycle before data is extracted for comparison.

Figure 6.16 shows the LES results for the steady and unsteady simulation at full needle lift. The same characteristic flow features are found in both simulations. As in the unsteady simulation, the formation of long, streamwise vortical structures originating from the needle volume is found. In the steady case, these structures are more stable than in the unsteady case, in which the majority of these vortices break up when passing through the needle seat. As a result, a larger number of vortical structures is found in the nozzle holes of the steady simulation. As in the unsteady simulation, vortex cavitation outside of the nozzle holes is also present in the steady case. In summary, the steady simulation at full needle lift captures the overall flow features of the unsteady simulation reasonably well.

At a low needle lift, in contrast, significant differences between steady and unsteady simulations are observed. In Fig. 6.17, we present the flow field and cavitation structures at a needle lift of $l_{N,s2} = 30 \times 10^{-6}$ m during the opening phase, Fig. 6.17(c/d), and at the same needle lift during the closing phase, Fig. 6.17(e/f).

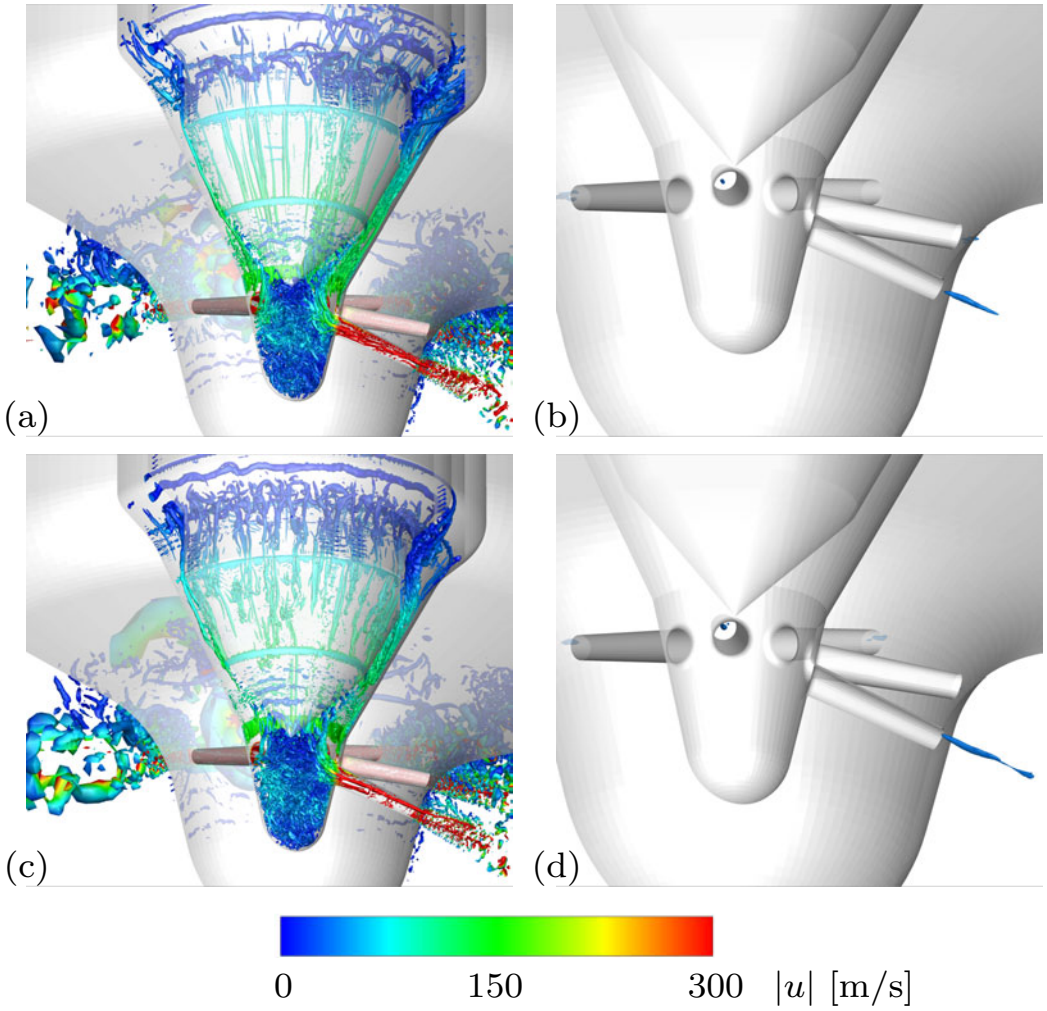

Figure 6.16: Steady (top row) vs. unsteady needle lift (bottom row): snapshots of iso-contours of $\lambda_2 = -2 \times 10^{-10}$ s$^{-}2$ colored by absolute velocity (left column), and iso-contours of $\alpha = 0.05$ (right column) for needle at maximum lift $l_{N,s1} = 264.4 \times 10^{-6}$ m at $t_{N,s1} = 580 \times 10^{-6}$ s.

Compared to the steady simulation, Fig. 6.17(a/b), the unsteady simulation during the opening phase does not yet develop vortical structures in the needle chamber. Otherwise, the flow field compares well with respect to small scale turbulent fluctuations in the sac-hole and the nozzle holes. A large separation is visible near the hole inlet. In terms of cavitation prediction, on the other hand, the two results differ significantly. In both cases, the needle seat is filled with a stable vapor sheet. In the steady simulation, formation of periodically shedding cavitation sheets is also found at the inlet edge of all nozzle holes, which is not found during the opening phase of the unsteady simulation.

When comparing the steady simulation to the results of the closing phase at equal needle lift position, we find that the unsteady simulation predicts higher flow velocities in the nozzle holes. This is due to the fact that the mass flow in the nozzle holes experiences a short time lag with respect to the actual needle seat area. Both simulations are in good agreement in terms of cavitation regions. However, larger cavitation structures are found in the liquid jets inside the combustion chamber are found in the unsteady simulation.

6.3 Summary

To assess the performance of Diesel injectors in the context of life-cycle and fuel mixing characteristics, it is important to understand the flow inside these devices, which is dominated by turbulence and cavitation phenomena. Experimental studies are complicated by the small geometries and timescales, as well as by the high operating pressures.

We have performed well-resolved LES of the flow inside a nine-hole common rail Diesel injector during a full injection cycle using a fully compressible two-fluid / two-phase homogenous mixture model for cavitating Diesel and non-condensable gas flows. The injector operates at a pressure of 1500 bar. The simulations provide detailed insight into the complex flow structure inside a high-pressure Diesel injection device.

We have defined four different phases of the injection cycle, during which the flow characteristics differ significantly. During the opening phase, small scale turbulent fluctuations are found inside the sac-hole and nozzle holes. Cavitation in this phase only occurs at the needle seat and limits the mass flow rate. During the main injection phase, large vortical structures are created in the needle chamber just upstream of the needle seat, and dominate the flow inside the nozzle holes. Due to the tapered shape of the nozzle holes, these vortices are further stretched and cause vortex cavitation at the nozzle outlet plane. When the injector needle is close to sealing the needle seat, formation of large cavitation structures is also found at the nozzle hole inlet. After closing of the injector, strong collapse events of vapor structures in the needle seat and the sac-hole cause the formation of violent shock waves. A fully compressible description of the flow is essential to capture such phenomena.

In addition to the simulations including a moving needle, we have performed computations at different steady needle lifts. In all cases, steady simulations capture the main flow features reasonably well. Steady needle simulations provide a worst case scenario in terms of localization and quantification of vapor formation. This information may suffice

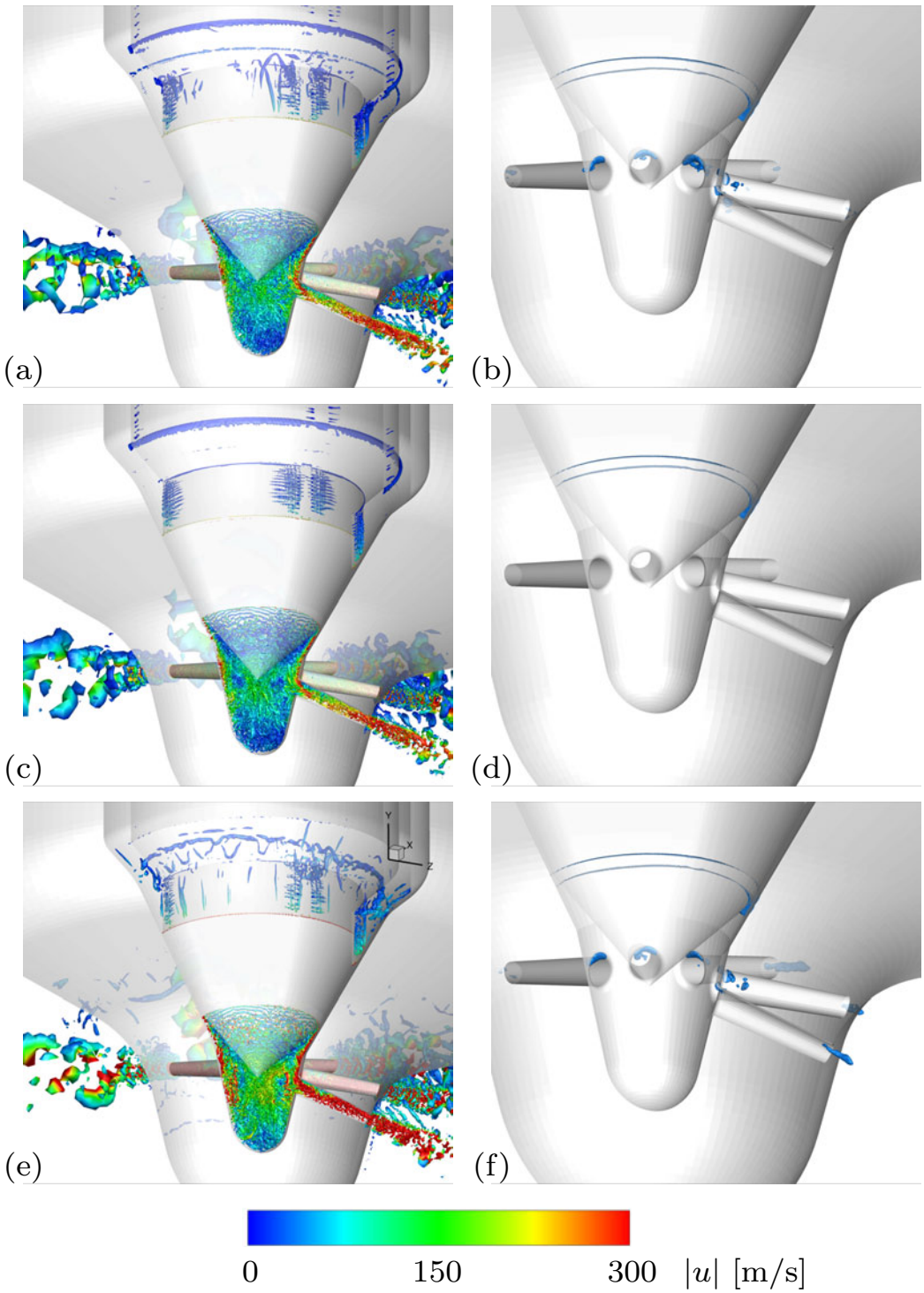

Figure 6.17: Steady (top row) vs. unsteady needle lift (middle and bottom row): snapshots of iso-contours of $\lambda_2 = -2 \times 10^{-10}$ s$^{-}2$ colored by absolute velocity (left column), and iso-contours of $\alpha = 0.05$ (right column) for needle at lift $l_{N,s2} = 30 \times 10^{-6}$ m at $t_{N,s2.1} = 128 \times 10^{-6}$ s (opening) and $t_{N,s2.2} = 997 \times 10^{-6}$ s (closing).

if one is only interested in the liquid jet break-up inside the combustion chamber during the main injection phase. The vapor creation during the closing phase, however, is caused by the liquid inertia distribution in the nozzle holes and thus requires information of the developed flow field just before closing of the needle seat. Hence, a reliable prediction of erosion-sensitive areas due to collapse events during and after closing of the needle can only be predicted accurately by including the unsteady needle motion.

7 Summary and Conclusion

Modern direct fuel injection systems for automotive applications aim at increasing injection pressures to reduce emissions and to meet legislative standards. Recently, injection pressures of more than 2500 bar have been employed in Diesel injectors to support jet break-up and atomization in order to improve combustion efficiency. As a result, the flow inside these devices becomes prone to strong turbulence and cavitation effects, which may affect the injector performance and durability, and must thus be understood and controlled during the design process to ensure a reliable operation. Experimental characterization of flow features reaches its limit due to high operating pressures and small spatial and temporal scales. Numerical simulations, on the other hand, can provide detailed insight into flow dynamics by highly resolved computations in both space and time.

The scope of this work has been to develop the relevant tools to conduct Large-Eddy simulations of high-pressure direct Diesel injection systems under realistic thermodynamic conditions, including movement of the injector needle, cavitation effects and interaction of gas and liquid phase. This problem has been chosen as an example for a complex, industrial application. The building blocks that have been investigated in this context are:

1. Development and improvement of a numerical method to represent moving bodies of arbitrary shape on Cartesian grids for LES

2. Development of a thermodynamic framework to perform simulations of cavitating liquids and gases

3. Validation of the new numerical and thermodynamic methods

4. Analysis of a reference simulation of a full injection cycle

In each chapter of this thesis, a detailed summary of the corresponding topic has been discussed. In the following, the main findings are briefly summarized.

First, the conservative immersed interface method has been improved for representing complex immersed solid boundaries on Cartesian grids. This has been found to be a necessary step to allow for numerical simulations of weakly compressible flows when dealing with moving geometries. It has been demonstrated, that an approximation of moving interfaces by a level-set field, as has been performed in previous works, results in unphysical oscillations in the vicinity of sharp corners in weakly compressible fluids. These numerical artefacts can be omitted when switching to an exact reconstruction of the geometrical parameters of cut-cells directly from a surface triangulation of the embedded body. The new method is based on cut-elements. It provides sub-cell resolution of the geometry and handles flows through narrow closing or opening gaps in a straightforward manner. The improved version of the immersed boundary method has been validated against canonical flow problems, such as oscillating cylinder flows and moving cylinders interacting with each other. The results were in very good agreement with reference data from the literature. A comparison of integral and instantaneous flow quantities of a two-dimensional rotating mixer with simulations results obtained from a body-fitted simulation demonstrated the performance of the new method also in weakly compressible environments.

An extension of the thermodynamic equilibrium cavitation model to perform monolithic, fully compressible two-fluid two-phase simulations of cavitating liquid jets injected into non-condensable gas has been discussed. The model uses an additional transport equation for the gas mass fraction and states a simple, but robust and effective method for LES. Different liquid and gas models can be integrated into the modular framework. In this thesis, different approaches for water and ISO4113 Diesel fuel have been presented. Validation studies of collapse events of isolated single bubbles showed good agreement with analytical and numerical reference data. The break-up of a cavitating liquid jet in air has been investigated. The setup resembles a large-scale injector nozzle operated at lower injection pressures. The cavitation and Reynolds numbers of the nozzle flow were $\sigma = \{1.27, 0.78, 0, 65\}$ and $Re = \{50000, 64000, 70000\}$, respectively. A qualitative comparison of cavitation structures showed good agreement with experimental data, while a comparison of mean and fluctuating velocity components revealed a lower level of turbulence in the simulation. Uncertainties in the inflow conditions were identified as a probable cause for this effect. The break-up of cavitating jets in the gas volume is strongly enhanced for low cavitation numbers. Classical Kelvin-Helmholtz type instabilities of the jet surface were considered to have only a minor impact on jet break-up when compared to effects induced by cavitation. For a supercavitating nozzle flow, collapse events of vapor structures near the nozzle exit, gas entrainment into the nozzle, and collapse events near the liquid-air interface inside the jet were found to be the main source for adding momentum of the liquid directed away from the jet axis and hence promote primary break-up.

Finally, high-resolution LES of the flow inside a nine-hole common rail Diesel injector including prescribed needle movement at a rail pressure of 1500 bar, using the developed numerical tools and thermodynamic models, have been performed. During opening and closing of the injector needle, small scale turbulent fluctuations dominate the flow field. In the main injection phase, large vortical structures are observed inside the nozzle holes and cause vortex cavitation inside the jet in the combustion chamber. Cavitation inside the injector occurs mainly during and shortly after the closing phase, which thus are identified as the phases of highest risk for surface erosion.

In conclusion, it has been shown that cut-element based immersed boundary methods are suited for the numerical simulation of complex, moving geometries. New thermodynamic models provided physical insight into jet break-up of cavitating liquid jets. The current state provides a starting point suitable for further geometry studies and optimization of injection systems or related industrial problems.

Bibliography

[1] Adams, N. A., Hickel, S., and Franz, S. Implicit subgrid-scale modeling by adaptive deconvolution. *Journal of Computational Physics 200*, 2 (2004), 412–431.

[2] Adams, N. A., and Schmidt, S. J. Shocks in cavitating flows. In *Bubble Dynamics and Shock Waves*, C. F. Delale, Ed. Springer Science & Business Media, 2013, pp. 235–256.

[3] Andriotis, A., Gavaises, M., and Arcoumanis, C. Vortex flow and cavitation in diesel injector nozzles. *Journal of Fluid Mechanics 610*, 1 (2008), 195–215.

[4] Arienti, M., and Sussman, M. An embedded level set method for sharp-interface multiphase simulations of Diesel injectors. *International Journal of Multiphase Flow 59*, C (2014), 1–14.

[5] Asi, O. Failure of a diesel engine injector nozzle by cavitation damage. *Engineering Failure Analysis 13*, 7 (2006), 1126–1133.

[6] Banister, D., Anderton, K., Bonilla, D., Givoni, M., and Schwanen, T. Transportation and the Environment. *Annual Review of Environment and Resources 36*, 1 (2011), 247–270.

[7] Bardina, J., Ferziger, J. H., and Reynolds, W. Improved subgrid-scale models for large-eddy simulation. In *American Institute of Aeronautics and Astronautics, Fluid and Plasma Dynamics Conference, 13th, Snowmass, Colo., July 14-16, 1980, 10 p.* (1980).

[8] Battistoni, M., Som, S., and Longman, D. E. Comparison of Mixture and Multifluid Models for In-Nozzle Cavitation Prediction. *J. Eng. Gas Turbines Power 136*, 6 (2014), 061506.

[9] Battistoni, M., Xue, Q., Som, S., and Pomraning, E. Effect of Off-Axis Needle Motion on Internal Nozzle and Near Exit Flow in a Multi-Hole Diesel Injector. *SAE Int. J. Fuels Lubr. 7*, 1 (2014), 167–182.

[10] Bayyuk, S. A., Powell, K. G., and Van Leer, B. A simulation technique for 2-D unsteady inviscid flows around arbitrarily moving and deforming bodies of arbitrary geometry. *AIAA Paper 93-3391-CP* (1993).

[11] Beattie, D., and Whalley, P. B. A simple two-phase frictional pressure drop calculation method. *International Journal of Multiphase Flow 8*, 1 (1982), 83–87.

[12] Befrui, B., Corbinelli, G., Robart, D., Reckers, W., and Weller, H. LES simulation of the internal flow and near-field spray structure of an outward-opening GDI injector and comparison with imaging data. *SAE SP 2187* (2008), 77.

[13] Bensow, R. E., and Bark, G. Implicit LES Predictions of the Cavitating Flow on a Propeller. *Journal of Fluids Engineering 132*, 4 (2010), 041302.

[14] Bergwerk, W. Flow Pattern in Diesel Nozzle Spray Holes. *Proceedings of the Institution of Mechanical Engineers 173*, 1 (1959), 655–660.

[15] Blokkeel, G., Barbeau, B., and Borghi, R. A 3D Eulerian model to improve the primary breakup of atomizing jet. *SAE Paper No. 2003-01-0005.* (2003).

[16] Brennen, C. E. *Cavitation and bubble dynamics.* Cambridge University Press, 1995.

[17] Brusiani, F., Falfari, S., and Pelloni, P. Influence of the Diesel Injector Hole Geometry on the Flow Conditions Emerging from the Nozzle. *Energy Procedia 45* (2014), 749–758.

[18] Chahine, G. L., Kapahi, A., Choi, J.-K., and Hsiao, C.-T. Modeling of surface cleaning by cavitation bubble dynamics and collapse. *Ultrasonics Sonochemistry 29* (2016), 528–549.

[19] Chapman, D. K. Computatisnal aerodynamics development and outlook. *AIAA Journal 17*, 12 (1979), 1293–1313.

[20] Chapman, L. Transport and climate change: a review. *Journal of Transport Geography 15*, 5 (2007), 354–367.

[21] Chmela, F., and Orthaber, G. Rate of Heat Release Prediction for Direct Injection Diesel Engines Based on Purely Mixing Controlled Combustion. *SAE Technical Paper* (1999).

[22] Choi, J.-I., Oberoi, R. C., Edwards, J. R., and Rosati, J. A. An immersed boundary method for complex incompressible flows. *Journal of Computational Physics 224*, 2 (2007), 757–784.

[23] Clarke, D. K., Hassan, H. A., and Salas, M. D. Euler calculations for multielement airfoils using Cartesian grids. *AIAA Journal 24*, 3 (1986), 353–358.

[24] Colella, P., Graves, D. T., Keen, B. J., and Modiano, D. A Cartesian grid embedded boundary method for hyperbolic conservation laws. *Journal of Computational Physics 211*, 1 (2006), 347–366.

[25] Cristallo, A., and Verzicco, R. Combined Immersed Boundary/Large-Eddy-Simulations of Incompressible Three Dimensional Complex Flows. *Flow, Turbulence and Combustion 77*, 1-4 (2006), 3–26.

[26] Dabiri, S., Sirignano, W. A., and Joseph, D. D. Interaction between a cavitation bubble and shear flow. *Journal of Fluid Mechanics 651* (2010), 93.

[27] d'Agostino, L., and Brennen, C. E. Linearized dynamics of spherical bubble clouds. *Journal of Fluid Mechanics 199* (1989), 155–176.

[28] Dahlquist, G., and Björck, Å. *Numerical Methods*. Dover Publications, 2003.

[29] De Tullio, M., Cristallo, A., Balaras, E., Pascazio, G., De Palma, P., Iaccarino, G., Napolitano, M., and Verzicco, R. Recent advances in the immersed boundary method. In *European Conference on Computational Fluid Dynamics ECCOMAS CFD 2006* (2006).

[30] De Tullio, M., Cristallo, A., Balaras, E., and Verzicco, R. Direct numerical simulation of the pulsatile flow through an aortic bileaflet mechanical heart valve. *Journal of Fluid Mechanics 622* (2009), 259–290.

[31] Delale, C., Schnerr, G. H., and Sauer, J. Quasi-one-dimensional steady-state cavitating nozzle flows. *Journal of Fluid Mechanics 427* (2001), 167–204.

[32] Desantes, J. M., Salvador, F. J., Carreres, M., and Martínez-López, J. Large-eddy simulation analysis of the influence of the needle lift on the cavitation in diesel injector nozzles. *Proceedings of the Institution of Mechanical Engineers, Part D: Journal of Automobile Engineering 229*, 4 (2015), 407–423.

[33] Desjardins, O., and Pitsch, H. Detailed numerical investigation of turbulent atomization of liquid jets. *Atomization and Sprays 20*, 4 (2010), 311–336.

[34] Diegelmann, F., Tritschler, V. K., Hickel, S., and Adams, N. A. Ignition and mixing in shock-bubble interaction with chemical reactions. In *Association of Applied Mathematics and Mechanics, March 23 - 27, 2015, Lecce, Italy.* (2015).

[35] Dittakavi, N., and Chunekar, A. Large eddy simulation of turbulent-cavitation interactions in a Venturi nozzle. *Journal of Fluids Engineering 132* (2010), 121301.

[36] Donea, J., Huerta, A., Ponthot, J., and Rodríguez Ferran, A. *Arbitrary Lagrangian–Eulerian methods.* Encyclopedia of Computational Mechanics. John Wiley & Sons, Ltd, 2004.

[37] Dongiovanni, C., and Coppo, M. *Accurate modelling of an injector for common rail systems.* INTECH Open Access Publisher, 2010.

[38] Dowell, M., and Jarratt, P. A modified regula falsi method for computing the root of an equation. *BIT Numerical Mathematics* (1971).

[39] Ducros, F., Ferrand, V., Nicoud, F., Weber, C., Darracq, D., Gacherieu, C., and Poinsot, T. Large-eddy simulation of the shock/turbulence interaction. *Journal of Computational Physics 152*, 2 (1999), 517–549.

[40] Duke, D. J., Schmidt, D. P., Neroorkar, K., Kastengren, A. L., and Powell, C. F. High-resolution large eddy simulations of cavitating gasoline-ethanol blends. *International Journal of Engine Research 14*, 6 (2013), 578–589.

[41] Dukowicz, J. K. A particle-fluid numerical model for liquid sprays. *Journal of Computational Physics 35*, 2 (1980), 229–253.

[42] Dular, M., Bachert, B., Stoffel, B., and Širok, B. Relationship between cavitation structures and cavitation damage. *Wear 257*, 11 (2004), 1176–1184.

[43] Duret, B., Reveillon, J., Ménard, T., and Demoulin, F. X. Improving primary atomization modeling through DNS of two-phase flows. *International Journal of Multiphase Flow 55*, 0 (2013), 130–137.

[44] Dütsch, H., Durst, F., Becker, S., and Lienhart, H. Low-Reynolds-number flow around an oscillating circular cylinder at low Keulegan–Carpenter numbers. *Journal of Fluid Mechanics 360* (1998), 249–271.

[45] Eberhardt, S. *Large-eddy simulations of supersonic mixing with application to scramjets*. PhD thesis, Institute of Aerodynamics, Technische Universität München, 2015.

[46] Eberhardt, S., and Hickel, S. LES Investigation of a Central Strut Injector with Perpendicular Injection for Scramjet Applications. In *5th EUCASS 2013 July 1-5, Munich, Germany* (2013).

[47] Eberhardt, S., and Hickel, S. Comparative Numerical Investigation of a Sonic Jet in a Supersonic Turbulent Crossflow. Springer, 2015, pp. 351–366.

[48] Egerer, C. P., Hickel, S., Schmidt, S. J., and Adams, N. A. Large-eddy simulation of turbulent cavitating flow in a micro channel. *Physics of Fluids 26*, 8 (2014), 085102.

[49] Egerer, C. P., Hickel, S., Schmidt, S. J., and Adams, N. A. LES of Temporally Evolving Turbulent Cavitating Shear Layers. In *High Performance Computing in Science and Engineering '14*. Springer, 2015, pp. 367–378.

[50] European Parliament and Council. Regulation (ec) no 443/2009.

[51] European Parliament and Council. Regulation (ec) no 459/2012.

[52] Fadlun, E. A., Verzicco, R., Orlandi, P., and Mohd-Yusof, J. Combined Immersed-Boundary Finite-Difference Methods for Three-Dimensional Complex Flow Simulations. *Journal of Computational Physics 161*, 1 (2000), 35–60.

[53] Falcovitz, J., Alfandary, G., and Hanoch, G. A two-dimensional conservation laws scheme for compressible flows with moving boundaries. *Journal of Computational Physics 138*, 1 (1997), 83–102.

[54] Franc, J.-P., and Michel, J.-M. *Fundamentals of cavitation*, vol. 76. Springer Science & Business Media, 2006.

[55] Franc, J.-P., Riondet, M., Karimi, A., and Chahine, G. L. Material and velocity effects on cavitation erosion pitting. *Wear 274-275* (2012), 248–259.

[56] Fujikawa, S., and Akamatsu, T. Effects of the non-equilibrium condensation of vapour on the pressure wave produced by the collapse of a bubble in a liquid. *Journal of Fluid Mechanics 97*, 03 (1980), 481–512.

[57] Gaffney JR, R., and Hassan, H. A. Euler calculations for wings using Cartesian grids. In *25th AIAA Aerospace Sciences Meeting* (Reston, Virigina, 1987), American Institute of Aeronautics and Astronautics.

[58] Garnier, E., Adams, N. A., and Sagaut, P. *Large eddy simulation for compressible flows*. Springer Science & Business Media, 2009.

[59] Gavaises, M. Flow in valve covered orifice nozzles with cylindrical and tapered holes and link to cavitation erosion and engine exhaust emissions. *International Journal of Engine Research 9*, 6 (2008), 435–447.

[60] Germano, M., Piomelli, U., Moin, P., and Cabot, W. H. A dynamic subgrid-scale eddy viscosity model. *Physics of Fluids A: Fluid Dynamics 3*, 7 (1991), 1760.

[61] Ghosal, S. An analysis of numerical errors in large-eddy simulations of turbulence. *Journal of Computational Physics 125*, 1 (1996), 187–206.

[62] Giannadakis, E., Gavaises, M., and Arcoumanis, C. Modelling of cavitation in diesel injector nozzles. *Journal of Fluid Mechanics 616*, 1 (2008), 153–193.

[63] Giannadakis, E., Gavaises, M., Roth, H., and Arcoumanis, C. Cavitation modelling in single-hole Diesel injector based on Eulerian-Lagrangian approach. In *Proc. THIESEL Intl Conf. Thermo- Fluid Dyn. Processes Diesel Engines, Valencia, Spain* (2004), La Editorial de la UPV, pp. 47–60.

[64] Giannadakis, E., Papoulias, D., Gavaises, M., Arcoumanis, C., Soteriou, C., and Tang, W. Evaluation of the predictive capability of diesel nozzle cavitation models. *SAE paper*, 2007-01 (2007), 0245.

[65] Gottlieb, S., and Shu, C.-W. Total variation diminishing Runge-Kutta schemes. *Mathematics of Computation of the American Mathematical Society 67(221)*, 221 (1998), 73–85.

[66] Goud, M., Greif, D., Suffa, M., Winklhofer, E., and Gill, D. Virtual Erosion Prediction, Design Optimisation and Combustion System Integration of High Pressure Fuel Injector Systems. . In *IMechE Conf Fuel Injection Systems for IC Engines, London.* (2012).

[67] Greif, D., Sampl, P., and Edelbauer, W. Cavitating Injector Flow Simulations Considering Longitudinal and Lateral Needle Displacement . *International Journal of Automotive Engineering 5* (2014), 85–90.

[68] Griffith, B. E., and Peskin, C. S. On the order of accuracy of the immersed boundary method: Higher order convergence rates for sufficiently smooth problems. *Journal of Computational Physics 208*, 1 (2005), 75–105.

[69] Grilli, M. *Analysis of the unsteady behavior in shockwave turbulent boundary layer interaction*. PhD thesis, Institute of Aerodynamics, Technische Universität München, 2014.

[70] Grilli, M., Hickel, S., Hu, X. Y., and Adams, N. A. Conservative Immersed Interface Method for compressible viscous flows with heat transfer. In *Academy Colloquium on Immersed boundary methods: current status and future research directions, Amsterdam, The Netherlands* (2009).

[71] Grilli, M., Schmid, P. J., Hickel, S., and Adams, N. A. Analysis of unsteady behaviour in shockwave turbulent boundary layer interaction. *Journal of Fluid Mechanics 700* (2012), 16–28.

[72] Guilmineau, E., and Queutey, P. A numerical simulation of vortex shedding from an oscillating circular cylinder. *Journal of Fluids and Structures 16*, 6 (2002), 773–794.

[73] Günther, C., Hartmann, D., Schneiders, L., Meinke, M., and Schröder, W. A Cartesian cut-cell method for sharp moving boundaries. *AIAA Paper 3387* (2011).

[74] Günther, C., Meinke, M., and Schröder, W. A flexible level-set approach for tracking multiple interacting interfaces in embedded boundary methods. *Computers and Fluids* (2014), 1–47.

[75] Harten, A., Lax, P. D., and Van Leer, B. On Upstream Differencing and Godunov-type Schemes for Hyperbolic Conservation Laws, 1982.

[76] He, Z., Zhong, W., Wang, Q., Jiang, Z., and Fu, Y. An investigation of transient nature of the cavitating flow in injector nozzles. *Applied Thermal Engineering 54*, 1 (2013), 56–64.

[77] Heywood, J. B. Internal combustion engine fundamentals.

[78] Hickel, S., and Adams, N. A. A proposed simplification of the adaptive local deconvolution method. *ESAIM: Proceedings 16* (2007), 66–76.

[79] Hickel, S., and Adams, N. A. On implicit subgrid-scale modeling in wall-bounded flows. *Physics of Fluids 19* (2007), 105106.

[80] Hickel, S., Adams, N. A., and Domaradzki, J. A. An adaptive local deconvolution method for implicit LES. *Journal of Computational Physics 213*, 1 (2006), 413–436.

[81] Hickel, S., Adams, N. A., and Mansour, N. N. Implicit subgrid-scale modeling for large-eddy simulation of passive-scalar mixing. *Physics of Fluids 19* (2007), 095102.

[82] Hickel, S., Egerer, C. P., and Larsson, J. Subgrid-scale modeling for implicit large eddy simulation of compressible flows and shock-turbulence interaction. *Physics of Fluids 26*, 10 (2014), 106101.

[83] Hickel, S., and Larsson, J. An adaptive local deconvolution model for compressible turbulence. In *Center for Turbulence Research Proceedings of the Summer Program 2008* (2008), p. 85.

[84] Hickel, S., Mihatsch, M. S., and Schmidt, S. J. Implicit Large Eddy Simulation of Cavitation in Micro Channel Flows. In *Proceedings of the WIMRC 3rd International Cavitation Forum* (University of Warwick, UK, 2011), S. C. Li, Ed., e-print arXiv:1401.6548, ISBN 978-0-9570404-1-0.

[85] Hirt, C. W., and Nichols, B. D. Volume of fluid (VOF) method for the dynamics of free boundaries. *Journal of Computational Physics 39*, 1 (1981), 201–225.

[86] Hu, X. Y., Khoo, B. C., Adams, N. A., and Huang, F. L. A conservative interface method for compressible flows. *Journal of Computational Physics 219*, 2 (2006), 553–578.

[87] Hubbard, B., and Chen, H.-C. A Chimera scheme for incompressible viscous flows with application to submarine hydrodynamics. *AIAA Paper 94-2210* (1994).

[88] Huber, B., and Ulbrich, H. *Simulation and Validation of a Common Rail Diesel Injector*. Proceedings of the Ninth International Conference on Engineering Computational Technology, Civil-Comp Press, Stirlingshire, Scotland, 2014.

[89] Hurlbut, S. E., Spaulding, M. L., and White, F. M. Numerical Solution for Laminar Two Dimensional Flow About a Cylinder Oscillating in a Uniform Stream. *Journal of Fluids Engineering 104*, 2 (1982), 214–220.

[90] Ishimoto, J., Sato, F., and Sato, G. Computational Prediction of the Effect of Microcavitation on an Atomization Mechanism in a Gasoline Injector Nozzle. *J. Eng. Gas Turbines Power 132*, 8 (2010), 082801.

[91] Jeong, J., and Hussain, F. On the identification of a vortex. *Journal of Fluid Mechanics 285*, 69 (1995), 69–94.

[92] Jia, M., Xie, M., Liu, H., Lam, W.-H., and Wang, T. Numerical simulation of cavitation in the conical-spray nozzle for diesel premixed charge compression ignition engines. *Fuel 90*, 8 (2011), 2652–2661.

[93] Kang, S., Iaccarino, G., and Moin, P. Accurate Immersed-Boundary Reconstructions for Viscous Flow Simulations. *AIAA Journal 47*, 7 (2009), 1750–1760.

[94] Kao, K.-H., and Liou, M.-S. Advance in overset grid schemes - From Chimera to DRAGON grids. *AIAA Journal 33*, 10 (1995), 1809–1815.

[95] Kim, D., and Choi, J.-I. Immersed boundary method for flow around an arbitrarily moving body. *Journal of Computational Physics 212*, 2 (2006), 662–680.

[96] Kim, J., Kim, D., and Choi, H. An Immersed-Boundary Finite-Volume Method for Simulations of Flow in Complex Geometries. *Journal of Computational Physics 171*, 1 (2001), 132–150.

[97] Kirkpatrick, M. P., Armfield, S. W., and Kent, J. H. A representation of curved boundaries for the solution of the Navier-Stokes equations on a staggered three-dimensional Cartesian grid. *Journal of Computational Physics 184* (2003), 1–36.

[98] Koukouvinis, P., Gavaises, M., Li, J., and Wang, L. Large Eddy Simulation of Diesel injector including cavitation effects and correlation to erosion damage. *Fuel 175*, C (July 2016), 26–39.

[99] Kravchenko, A., and Moin, P. On the effect of numerical errors in large eddy simulations of turbulent flows. *Journal of Computational Physics 131*, 2 (1997), 310–322.

[100] Kunz, R. F., Boger, D. A., Stinebring, D. R., Chyczewski, T. S., Lindau, J. W., Gibeling, H. J., Venkateswaran, S., and Govindan, T. A preconditioned Navier–Stokes method for two-phase flows with application to cavitation prediction. *Computers and Fluids 29*, 8 (2000), 849–875.

[101] Larsson, J., Bermejo-Moreno, I., and Lele, S. K. Reynolds- and Mach-number effects in canonical shock–turbulence interaction. *Journal of Fluid Mechanics 717* (2013), 293–321.

[102] Lasheras, J., and Hopfinger, E. Liquid jet instability and atomization in a coaxial gas stream. *Annual Review of Fluid Mechanics 32* (2000), 275–308.

[103] Lauer, E., Hu, X. Y., Hickel, S., and Adams, N. A. Numerical investigation of collapsing cavity arrays. *Physics of Fluids 24* (2012), 052104.

[104] Lauer, E., Hu, X. Y., Hickel, S., and Adams, N. A. Numerical modelling and investigation of symmetric and asymmetric cavitation bubble dynamics. *Computers and Fluids 69* (2012), 1–19.

[105] Lemmon, E., McLinden, M., and Friend, D. Thermophysical Properties of Fluid Systems. In *NIST Chemistry WebBook, NIST Standard Reference Database Number 69*, P. Linstrom and W. Mallard, Eds. National Institute of Standards and Technology, Gaithersburg MD, 20899, http://webbook.nist.gov, retrieved March 20, 2015, 2005.

[106] Leonard, A. Energy cascade in large-eddy simulations of turbulent fluid flows. In *Turbulent Diffusion in Environmental Pollution* (1974), pp. 237–248.

[107] Liao, C.-C., Chang, Y.-W., Lin, C.-A., and McDonough, J. M. Simulating flows with moving rigid boundary using immersed-boundary method. *Computers and Fluids 39*, 1 (2010), 152–167.

[108] Lin, S. P., and Reitz, R. D. Drop and spray formation from a liquid jet. *Annual Review of Fluid Mechanics 30*, 1 (1998), 85–105.

[109] Macian, V., Payri, R., Margot, X., and Salvador, F. J. A CFD analysis of the influence of diesel nozzle geometry on the inception of cavitation. *Atomization and Sprays 13*, 5&6 (2003).

[110] Margot, X., Hoyas, S., Fajardo, P., and Patouna, S. Cfd study of needle motion influence on the spray conditions of single-hole injectors. *Atomization and Sprays 21*, 1 (2011), 31–40.

[111] Marmottant, P., and Villermaux, E. On spray formation. *Journal of Fluid Mechanics 498* (1999), 73–111.

[112] Marsden, G., and Rye, T. The governance of transport and climate change. *Journal of Transport Geography 18*, 6 (2010), 669–678.

[113] Ménard, T., Tanguy, S., and Berlemont, A. Coupling level set/VOF/ghost fluid methods: Validation and application to 3D simulation of the primary break-up of a liquid jet. *International Journal of Multiphase Flow 33*, 5 (2007), 510–524.

[114] Meyer, M. *Simulation of Complex Turbulent Flows on Cartesian Adaptive Grids*. PhD thesis, Institute of Aerodynamics, Technische Universität München, 2013.

[115] Meyer, M., Devesa, A., Hickel, S., Hu, X. Y., and Adams, N. A. A conservative immersed interface method for Large-Eddy Simulation of incompressible flows. *Journal of Computational Physics 229*, 18 (2010), 6300–6317.

[116] Meyer, M., Hickel, S., and Adams, N. A. Assessment of Implicit Large-Eddy Simulation with a Conservative Immersed Interface Method for turbulent cylinder flow. *International Journal of Heat and Fluid Flow 31*, 3 (2010), 368–377.

[117] Meyer, M., Hickel, S., Breitsamter, C., and Adams, N. A. Wall-Modelled Implicit Large-Eddy Simulation of the RA16SC1 Highlift Configuration. In *Fluid Dynamics and Co-located Conferences*. American Institute of Aeronautics and Astronautics, 2014.

[118] Mihatsch, M. S. *Numerical Prediction of Erosion and Degassing Effects in Cavitating Flows*. PhD thesis, Institute of Aerodynamics, Technische Universität München, 2016.

[119] Mihatsch, M. S., Schmidt, S. J., and Adams, N. A. Cavitation erosion prediction based on analysis of flow dynamics and impact load spectra. *Physics of Fluids 27*, 10 (2015), 103302.

[120] Mihatsch, M. S., Schmidt, S. J., Thalhamer, M., and Adams, N. A. Numerical Prediction of Erosive Collapse Events in Unsteady Compressible Cavitating Flows. In *Computational Methods in Applied Sciences*, L. Eça, E. Oñate, J. García-Espinosa, T. Kvamsdal, and P. Bergan, Eds. Springer Netherlands, 2013, pp. 187–198.

[121] Mihatsch, M. S., Schmidt, S. J., Thalhamer, M., Adams, N. A., Skoda, R., and Iben, U. Collapse Detection in Compressible 3-D Cavitating Flows and Assessment of Erosion Criteria. In *Proceedings of the WIMRC 3rd International Cavitation Forum* (University of Warwick, UK, 2011), S. C. Li, Ed., e-publication can be accessed at https://files.warwick.ac.uk/shengcaili/files/Proceedings+2011/.

[122] Mitroglou, N., and Gavaises, M. Mapping of cavitating flow regimes in injectors for medium-/heavy-duty diesel engines. *International Journal of Engine Research 14*, 6 (2013), 590–605.

[123] Mittal, R., Dong, H., Bozkurttas, M., Najjar, F. M., Vargas, A., and von Loebbecke, A. A versatile sharp interface immersed boundary method for incompressible flows with complex boundaries. *Journal of Computational Physics 227*, 10 (2008), 4825–4852.

[124] Mittal, R., and Iaccarino, G. Immersed boundary methods. *Annual Review of Fluid Mechanics 37*, 1 (2005), 239–261.

[125] Mohd-Yusof, J. Combined immersed-boundary/B-spline methods for simulations of ow in complex geometries. *Center for Turbulence Research Annual Research Briefs* (1997), 317–327.

[126] Momma, T., and Lichtarowicz, A. A study of pressures and erosion produced by collapsing cavitation. *Wear 186* (1995), 425–436.

[127] Obreschkow, D., Kobel, P., Dorsaz, N., de Bosset, A., Nicollier, C., and Farhat, M. Cavitation Bubble Dynamics inside Liquid Drops in Microgravity. *Physical Review Letters 97*, 9 (2006), 204501.

[128] Ohl, C.-D., Arora, M., Dijkink, R., Janve, V., and Lohse, D. Surface cleaning from laser-induced cavitation bubbles. *Applied Physics Letters 89*, 7 (2006), 074102–074102–3.

[129] Örley, F., Grilli, M., Hickel, S., Schmidt, S. J., and Adams, N. A. Application of Immersed Boundary Methods for the Investigation of Cavitating Liquid Flows Interacting with Moving Geometries. In *Joint EUROMECH / ERCOFTAC Colloquium 549 'Immersed Boundary Methods: Current Status and Future Research Directions', June 17-19 2013, Leiden, The Netherlands* (2013).

[130] Örley, F., Hickel, S., Schmidt, S. J., and Adams, N. A. LES of cavitating flow inside a Diesel injector including dynamic needle movement. *Journal of Physics: Conference Series 656*, 1 (2015), 012097.

[131] Örley, F., Hickel, S., Schmidt, S. J., and Adams, N. A. Large-Eddy Simulation of turbulent, cavitating fuel flow inside a 9-hole Diesel injector including needle movement. *International Journal of Engine Research* (2016).

[132] Örley, F., Pasquariello, V., Hickel, S., and Adams, N. A. Cut-element based immersed boundary method for moving geometries in compressible liquid flows with cavitation. *Journal of Computational Physics 283*, C (2015), 1–22.

[133] Örley, F., Trummler, T., Hickel, S., Mihatsch, M. S., Schmidt, S. J., and Adams, N. A. Large-eddy simulation of cavitating nozzle and jet flows. *Journal of Physics: Conference Series 656*, 1 (2015), 012096.

[134] Örley, F., Trummler, T., Hickel, S., Mihatsch, M. S., Schmidt, S. J., and Adams, N. A. Large-eddy simulation of cavitating nozzle flow and primary jet break-up. *Physics of Fluids 27*, 8 (2015), 086101.

[135] Örley, F., Trummler, T., Hickel, S., Mihatsch, M. S., Schmidt, S. J., and Adams, N. A. LES of Cavitating Nozzle and Jet Flows. In *Direct and Large-Eddy Simulation X, ERCOFTAC Workshop DLES 10, May 27-29, 2015* (Limassol, Cyprus, 2015).

[136] Pasquariello, V., Grilli, M., Hickel, S., and Adams, N. A. Large-eddy simulation of passive shock-wave/boundary-layer interaction control. *International Journal of Heat and Fluid Flow 49*, C (2014), 116–127.

[137] Pasquariello, V., Hammerl, G., Örley, F., Hickel, S., Danowski, C., Popp, A., Wall, W. A., and Adams, N. A. A cut-cell Finite Volume – Finite Element coupling approach for fluid-structure interaction in compressible flow . *Journal of Computational Physics 307*, C (2016), 670–695.

[138] Pasquariello, V., Hickel, S., and Adams, N. A. *Extension of the Conservative Immersed Interface Method towards high-order interpolation*. Sonderforschungsbereich/Transregio 40 - Annual Report 2013. Sonderforschungsbereich/Transregio 40 - Annual Report 2013, 2013.

[139] Payri, R., Bermudez, V., Payri, R., and Salvador, F. J. The influence of cavitation on the internal flow and the spray characteristics in diesel injection nozzles. *Fuel 83*, 4-5 (2004), 419–431.

[140] Payri, R., Salvador, F. J., Gimeno, J., and de la Morena, J. Effects of nozzle geometry on direct injection diesel engine combustion process. *Applied Thermal Engineering 29*, 10 (2009), 2051–2060.

[141] Pember, R. B., Bell, J. B., Colella, P., Curtchfield, W. Y., and Welcome, M. L. An Adaptive Cartesian Grid Method for Unsteady Compressible Flow in Irregular Regions. *Journal of Computational Physics 120*, 2 (1994), 278–304.

[142] Peskin, C. S. Flow patterns around heart valves: a numerical method. *Journal of Computational Physics 10*, 2 (1972), 252–271.

[143] Peskin, C. S. The immersed boundary method. *Acta Numerica 11* (2002), 479–517.

[144] Philipp, A., and Lauterborn, W. Cavitation erosion by single laser-produced bubbles. *Journal of Fluid Mechanics 361* (1998), 75–116.

[145] Plesset, M. S., and Chapman, R. B. Collapse of an initially spherical vapour cavity in the neighbourhood of a solid boundary. *Journal of Fluid Mechanics 47*, 02 (1971), 283–290.

[146] Plesset, M. S., and Prosperetti, A. Bubble dynamics and cavitation. *Annual Review of Fluid Mechanics 9*, 1 (1977), 145–185.

[147] Powell, C. F., Kastengren, A. L., Liu, Z., and Fezzaa, K. The Effects of Diesel Injector Needle Motion on Spray Structure. *J. Eng. Gas Turbines Power 133*, 1 (2011), 012802.

[148] Rayleigh, L. VIII. On the pressure developed in a liquid during the collapse of a spherical cavity. *The London, Edinburgh, and Dublin Philosophical Magazine and Journal of Science 34*, 200 (1917), 94–98.

[149] Reid, B. A., Gavaises, M., Mitroglou, N., Hargrave, G. K., Garner, C. P., Long, E. J., and McDavid, R. M. On the formation of string cavitation inside fuel injectors. *Experiments in Fluids 55*, 1 (2014), 1662.

[150] Reif, K. *Dieselmotor-Management Im Überblick*. Einschließlich Abgastechnik. Springer, 2010.

[151] Reitz, R. D. Mechanism of atomization of a liquid jet. *Physics of Fluids 25*, 10 (1982), 1730.

[152] Robinson, P. B., Blake, J. R., Kodama, T., Shima, A., and Tomita, Y. Interaction of cavitation bubbles with a free surface. *Journal of Applied Physics 89*, 12 (2001), 8225.

[153] Roma, A. M., Peskin, C. S., and Berger, M. An adaptive version of the immersed boundary method. *Journal of Computational Physics 153*, 2 (1999), 509–534.

[154] Russell, D., and Jane Wang, Z. A cartesian grid method for modeling multiple moving objects in 2D incompressible viscous flow. *Journal of Computational Physics 191*, 1 (2003), 177–205.

[155] Salvador, F. J., Hoyas, S., Novella, R., and Martínez-López, J. Numerical simulation and extended validation of two-phase compressible flow in diesel injector nozzles. *Proceedings of the Institution of Mechanical Engineers, Part D: Journal of Automobile Engineering 225*, 4 (2011), 545–563.

[156] Saurel, R., Cocchi, P., and Butler, P. B. Numerical Study of Cavitation in the Wake of a Hypervelocity Underwater Projectile. *Journal of Propulsion and Power 15*, 4 (1999), 513–522.

[157] Saurel, R., Petitpas, F., and Abgrall, R. Modelling phase transition in metastable liquids: application to cavitating and flashing flows. *Journal of Fluid Mechanics 607* (2008), 313–350.

[158] Saurel, R., Petitpas, F., and Berry, R. A. Simple and efficient relaxation methods for interfaces separating compressible fluids, cavitating flows and shocks in multiphase mixtures. *Journal of Computational Physics 228*, 5 (2009), 1678–1712.

[159] Schmidt, D. P. *Cavitation in diesel fuel injector nozzles*. PhD thesis, University of Wisconsin - Madison, 1997.

[160] Schmidt, D. P., Rutland, C. J., Corradini, M. L., Roosen, P., and Genge, O. Cavitation in Two-Dimensional Asymmetric Nozzles. *SAE Technical Paper 1999-01-0518* (1999).

[161] Schmidt, S. J., Mihatsch, M. S., Thalhamer, M., and Adams, N. A. Assessment of the Prediction Capability of a Thermodynamic Cavitation Model for the Collapse Characteristics of a Vapor-Bubble Cloud. In *Proceedings of the WIMRC 3rd International Cavitation Forum* (University of Warwick, UK, 2011), S. C. Li, Ed., ISBN 978-0-9570404-1-0.

[162] Schmidt, S. J., Mihatsch, M. S., Thalhamer, M., and Adams, N. A. Assessment of erosion sensitive areas via compressible simulation of unsteady cavitating flows. In *Advanced Experimental and Numerical Techniques for Cavitation Erosion Prediction*, K.-H. Kim, G. L. Chahine, J.-P. Franc, and A. Karimi, Eds. Springer Netherlands, 2014, pp. 329–344.

[163] Schmidt, S. J., Sezal, I. H., and Schnerr, G. H. Compressible simulation of high-speed hydrodynamics with phase change. In *ECCOMAS CFD 2006, TU Delft, The Netherlands* (2006), P. Wesseling, E. Onate, and J. Périaux, Eds.

[164] Schneiders, L., Hartmann, D., Meinke, M., and Schröder, W. An accurate moving boundary formulation in cut-cell methods. *Journal of Computational Physics 235* (2013), 786–809.

[165] Schnerr, G. H., Sezal, I. H., and Schmidt, S. J. Numerical investigation of three-dimensional cloud cavitation with special emphasis on collapse induced shock dynamics. *Physics of Fluids 20*, 4 (2008), 040703.

[166] Schumann, F., Sarikoc, F., Buri, S., Kubach, H., and Spicher, U. Potential of spray-guided gasoline direct injection for reduction of fuel consumption and simultaneous compliance with stricter emissions regulations. *International Journal of Engine Research 14*, 1 (2013), 80–91.

[167] Senocak, I., and Shyy, W. A Pressure-Based Method for Turbulent Cavitating Flow Computations. *Journal of Computational Physics 176*, 2 (2002), 21–21.

[168] Seo, J. H., and Mittal, R. A sharp-interface immersed boundary method with improved mass conservation and reduced spurious pressure oscillations. *Journal of Computational Physics 230*, 19 (2011), 7347–7363.

[169] Sezal, I. H. *Compressible Dynamics of Cavitating 3-D Multi-Phase Flows*. PhD thesis, Technische Universität München, Verlag Dr. Hut, 2009.

[170] Shibata, S., Nishio, S., Sou, A., Akayama, D., and Mashida, M. Evaluation of cavitation in injector nozzle and correlation with liquid atomization. *Journal of Visualization 18*, 3 (2015), 481–492.

[171] Smagorinsky, J. General circulation experiments with the primitive equations: I. the basic experiment*. *Monthly weather review 91*, 3 (1963), 99–164.

[172] Som, S., and Aggarwal, S. K. Effects of primary breakup modeling on spray and combustion characteristics of compression ignition engines. *Combustion and Flame 157*, 6 (2010), 1179–1193.

[173] Som, S., Ramirez, A., Aggarwal, S. K., El-Hannouny, E. M., and Longman, D. E. Investigation of nozzle flow and cavitation characteristics in a diesel injector. *J. Eng. Gas Turbines Power 132*, ANL/ES/JA-62050 (2010), 042802.

[174] Sou, A., Hosokawa, S., and Tomiyama, A. Effects of cavitation in a nozzle on liquid jet atomization. *International Journal of Heat and Mass Transfer 50*, 17-18 (2007), 3575–3582.

[175] Sou, A., Tomiyama, A., Hosokawa, S., Nigorikawa, S., and Maeda, T. Cavitation in a two-dimensional nozzle and liquid jet atomization:(LDV measurement of liquid velocity in a nozzle). *JSME International Journal. Series B, Fluids and Thermal Engineering 49*, 4 (2006), 1253–1259.

[176] Strotos, G., Koukouvinis, P., Theodorakakos, A., Gavaises, M., and Bergeles, G. Transient heating effects in high pressure Diesel injector nozzles. *International Journal of Heat and Fluid Flow 51* (2014), 257–267.

[177] Su, S.-W., Lai, M.-C., and Lin, C.-A. An immersed boundary technique for simulating complex flows with rigid boundary. *Computers and Fluids 36*, 2 (2007), 313–324.

[178] Tamaki, N., Shimizu, M., and Hiroyasu, H. Enhancement of the atomization of a liquid jet by cavitation in a nozzle hole. *Atomization and Sprays 11*, 2 (2001), 125–137.

[179] Tomita, Y., and Shima, A. Mechanisms of impulsive pressure generation and damage pit formation by bubble collapse. *Journal of Fluid Mechanics 169* (1986), 535–564.

[180] Tritschler, V. K., Avdonin, A., Hickel, S., Hu, X. Y., and Adams, N. A. Quantification of initial-data uncertainty on a shock-accelerated gas cylinder. *Physics of Fluids 26*, 2 (2014), 026101.

[181] Tritschler, V. K., Hickel, S., Hu, X. Y., and Adams, N. A. On the Kolmogorov inertial subrange developing from Richtmyer-Meshkov instability. *Physics of Fluids 25*, 7 (2013), 071701.

[182] Tritschler, V. K., Hu, X. Y., Hickel, S., and Adams, N. A. Numerical simulation of a Richtmyer–Meshkov instability with an adaptive central-upwind sixth-order WENO scheme. *Physica Scripta T155* (2013), 014016.

[183] Tritschler, V. K., Olson, B. J., Lele, S. K., Hickel, S., Hu, X. Y., and Adams, N. A. On the Richtmyer–Meshkov instability evolving from a deterministic multimode planar interface. *Journal of Fluid Mechanics 755* (2014), 429–462.

[184] Tritschler, V. K., Zubel, M., Hickel, S., and Adams, N. A. Evolution of length scales and statistics of Richtmyer-Meshkov instability from direct numerical simulations. *Physical Review E 90*, 6 (2014), 063001.

[185] Trummler, T. *Gasmodellierung in kavitierenden Strömungen.* Masterarbeit, Lehrstuhl für Aerodynamik und Strömungsmechanik, Technische Universität München. 2014.

[186] Udaykumar, H. S., Mittal, R., Rampunggoon, P., and Khanna, A. A Sharp Interface Cartesian Grid Method for Simulating Flows with Complex Moving Boundaries. *Journal of Computational Physics 174*, 1 (2001), 345–380.

[187] Udaykumar, H. S., Mittal, R., and Shyy, W. Computation of solid–liquid phase fronts in the sharp interface limit on fixed grids. *Journal of Computational Physics 153*, 2 (1999), 535–574.

[188] Udaykumar, H. S., Shyy, W., and Rao, M. M. Elafint: a mixed Eulerian–Lagrangian method for fluid flows with complex and moving boundaries. *International journal for numerical methods in fluids 22*, 8 (1996), 691–712.

[189] Ueberall, A., Otte, R., Eilts, P., and Krahl, J. A literature research about particle emissions from engines with direct gasoline injection and the potential to reduce these emissions. *Fuel 147*, C (2015), 203–207.

[190] Van Albada, G., Van Leer, B., and Roberts Jr, W. A comparative study of computational methods in cosmic gas dynamics. *Astronomy and Astrophysics 108* (1982), 76–84.

[191] Verzicco, R., Mohd-Yusof, J., Orlandi, P., and Haworth, D. LES in complex geometries using boundary body forces. *Center for Turbulence Research Proceedings of the Summer Program 1998* (1998), 171–186.

[192] Villermaux, E. Fragmentation. *Annual Review of Fluid Mechanics 39*, 1 (2007), 419–446.

[193] Wang, Y., Qiu, L., Reitz, R. D., and Diwakar, R. Simulating cavitating liquid jets using a compressible and equilibrium two-phase flow solver. *International Journal of Multiphase Flow 63*, C (2014), 52–67.

[194] Xu, S., and Wang, Z. J. An immersed interface method for simulating the interaction of a fluid with moving boundaries. *Journal of Computational Physics 216*, 2 (2006), 454–493.

[195] Yang, J., and Balaras, E. An embedded-boundary formulation for large-eddy simulation of turbulent flows interacting with moving boundaries. *Journal of Computational Physics 215*, 1 (2006), 12–40.

[196] Ye, T., Mittal, R., Udaykumar, H. S., and Shyy, W. An accurate Cartesian grid method for viscous incompressible flows with complex immersed boundaries. *Journal of Computational Physics 156*, 2 (1999), 209–240.

[197] Young, F. *Cavitation.* Imperial College Press, 1999.

[198] Yuan, W., Sauer, J., and Schnerr, G. H. Modeling and computation of unsteady cavitation flows in injection nozzles. *Mécanique & Industries 2*, 5 (2001), 383–394.

[199] Zhao, H., Quan, S., Dai, M., Pomraning, E., Senecal, P. K., Xue, Q., Battistoni, M., and Som, S. Validation of a Three-Dimensional Internal Nozzle Flow Model Including Automatic Mesh Generation and Cavitation Effects. *J. Eng. Gas Turbines Power 136*, 9 (2014), 092603.

[200] Zwerger, C. *Numerical investigation of the flow field around a delta wing*. PhD thesis, Institute of Aerodynamics, Technische Universität München, 2015.